6-4-2020

Synthesis and evaluation of catalytic application of porous resin

Mahboubeh Nabavinia
Rowan University

SYNTHESIS AND EVALUATION OF CATALYTIC APPLICATION OF POROUS RESIN

By
Mahboubeh Nabavinia

A Dissertation

Submitted to the
Department of Chemical Engineering
Henry M. Rowan College of Engineering
In partial fulfillment of the requirements
For the degree of
Doctor of Philosophy
at
Rowan University
January 22, 2020

Thesis Chair: Iman Noshadi, Ph.D.

Dedications

For Mom, Dad, and My sisters

Acknowledgments

I would like to express my gratitude to Dr. Iman Noshadi, my graduate advisor and thesis chair. In addition, I would like to thank Dr. Mariano Savelski, Dr. Robert Hesketh, Dr. Manuj Pandey, Dr. Subash Jonnalagadda, and Dr. Mague Amos, for all the help and support they provided though my time at Rowan University.

I would also like to thank my friends and family from back home. My parents, sisters, and extended family have truly shaped my life to which I am forever indebted.

Abstract

Mahboubeh Nabavinia
SYNTHESIS AND EVALUATION OF CATALYTIC APPLICATION OF POROUS RESIN
2018-2019
Iman Noshadi, Ph.D.
Doctor of Philosophy

The abilities to tailor catalytic functional groups and chemical characteristics onto a robust polymer structure make mesoporous phenolic resins great candidates for catalytic support applications. The use of a template synthesis method for configuring a catalytic structure is neither commercially nor environmentally friendly. In this Ph.D. thesis, new one-pot template-free methods for synthesizing mesoporous metal-doped phenol-formaldehyde resins were developed. The methods facilitate scaling for industrial catalytic applications in pharmaceutical, environmental, and medical applications. Heterogeneous palladium centered catalytic mesoporous structures were synthesized by a single-stage template-free method. BET adsorption measurements, SEM, EDX, XPS, and TEM were used to study the surface area, uniformity of Pd distribution, and an interconnected porous network structure. Subsequently, the activity of the catalyst was evaluated in bed batch and continuous reactors for Suzuki-Miyaura cross-coupling reactions. The catalyst was confirmed for biocompatibility and used for extracellular synthesis of anti-cancer PP121 drug in mono-cell layer and 3D-printed model structures with encapsulated cells. The metabolic activity and flow cytometry results confirmed the efficiency of this catalyst for in-situ drug synthesis. Additionally, this catalyst was doped using cobalt and nickel and evaluated for CO_2 capture and electrochemical conversion to fuels and chemicals.

Table of Contents

Table of Contents (Continued)

Table of Contents (Continued)

List of Figures

List of Figures (Continued)

Figure Page

List of Figures (Continued)

Figure Page

List of Tables

Table Page

Chapter 1

Literature Review

Text and figures are reproduced and adapted with permission from Stanzione JF, Suib S, Liu F, and Noshadi I, "One-Pot Aqueous and Template-Free Synthesis of Mesoporous Polymeric Resins." Catalysts. 2019 September; 9(9):782.

1.1 Introduction

The family of ordered mesoporous resins (OMR) is a versatile class of materials, as they can be useful in a plethora of applications in separation [1], catalysis [2-5], adsorption [1, 6, 7], bioreactors [8], and sensors [9]. Materials with pore diameters 2-50 nm have mesostructured. The ordered mesoporosity creating large surface areas and uniform pore sizes, spark significant contributions with these applications [1]. The combination of high porosity and surface area alongwith tailorable chemistries allows profuse interaction with atoms, ions, and even large molecules and molecular assemblies at the surface and throughout the interpenetrating porous network. These advantages encourage the application of OMRs in adsorption and catalysis with possibilities for industrial scale-up [9-12].

1.2 Motivation and Background

The intrinsic character of organic molecules creates mesoporous organic materials that are dissimilar from their inorganic counterparts. In general, mesostructured materials can be synthesized through several routes, including controlled foaming, ion track etching, molecular imprinting phase, separation, and a templating approach by employing colloidal particles or porous inorganic materials [3, 10, 11]. Soft or hard templating methods are

conventionally used to prepare mesoporous resins. The most common hard template contains ordered mesoporous silica, siliceous colloids, and colloidal silica crystals. The template is removed in the last step of the synthesis process by calcification at high temperature or acid washing. Although the soft- templating method eliminates the need for synthesizing siliceous or related hard templates but using surfactants and block copolymers (e.g., Pluronic F127, P123) decreases the number of synthesis steps and cost of the process. The soft-templating process is based on using phenolic resins as thermosetting polymer and triblock copolymers as thermally degradable surfactants to form ordered polymer-polymer composite mesostructured after the carbonization process is distorted to obtain ordered mesoporous carbons [5, 12]. As shown in Figure 1, the cooperative assembly of the block copolymer in aqueous-ethanolic media forms nicely arranged micelles. This organized structure of the organic template is critical for the formation of ordered mesostructure. The organic-organic self-assembly method was used by Tanaka et al. successfully. Resorcinol and formaldehyde were used as carbon sources and Pluronic F127 (EO106-PO70-EO106) as diblock [13]. The same carbon sources were used by Dai et al. to prepare ordered mesoporous carbon films with open-pore structures that were synthesized by using poly(styrene)-b-poly (4-vinyl pyridine) (PS-b-P4VP) as a template. Significance in both industrial applications and synthesis of ordered mesoporous resins by novel routes were developed by Bai et al. Phenol-formaldehyde resins (OMR-n where n stands for synthesis temperatures of 200 and 260 ºC) were synthesized at high-temperature (200 and 260 ºC) to produce ordered mesoporous resins. They used copolymer surfactants "such as F127" to control morphology monoliths, which have been used as templates under

alkaline conditions. These ordered mesoporous resins have a high crosslinking degree, giving excellent thermal and mechanical stabilities [4].

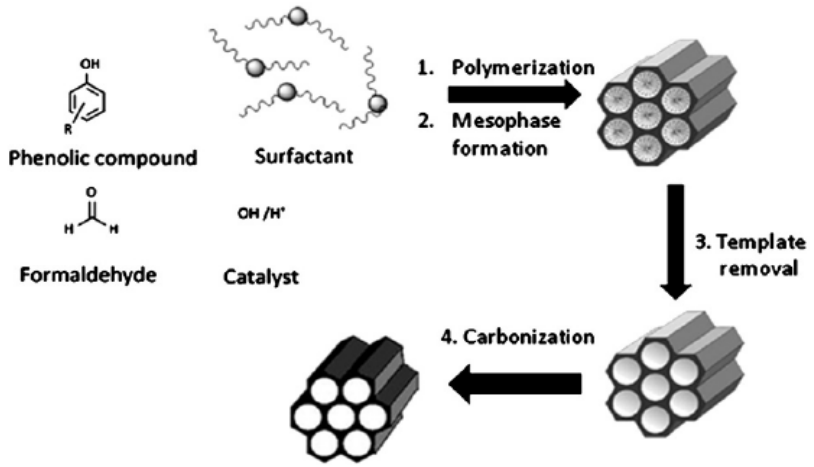

Figure 1. Schematic representation of the direct synthesis of ordered mesoporous phenolic resins and carbons using a surfactant as soft template.

1.3 Synthesis and Application of OMR Catalyst

The impressive chemical polymer characteristics of mesoporous phenolic resins make them a great candidate for using as the catalyst support. In fact, functional groups or metal elements, compounds, or nanoparticles can be introduced into these polymer networks [14-15]. Overview of the functionalization and incorporation of metals and hetero elements in mesoporous phenolic resins and carbons showed in Figure 2. Two main methods are used to anchor this hetero-atom or metal to resins and carbons network: 1. Involving a metal or other specific precursor in the self-assembly, 2. Polymerization which can be used as a carbon source containing the metal or compound (in-situ methods) or can be used as a post-synthesis treatment such as impregnation, adsorption, grafting, or ion exchange methods.

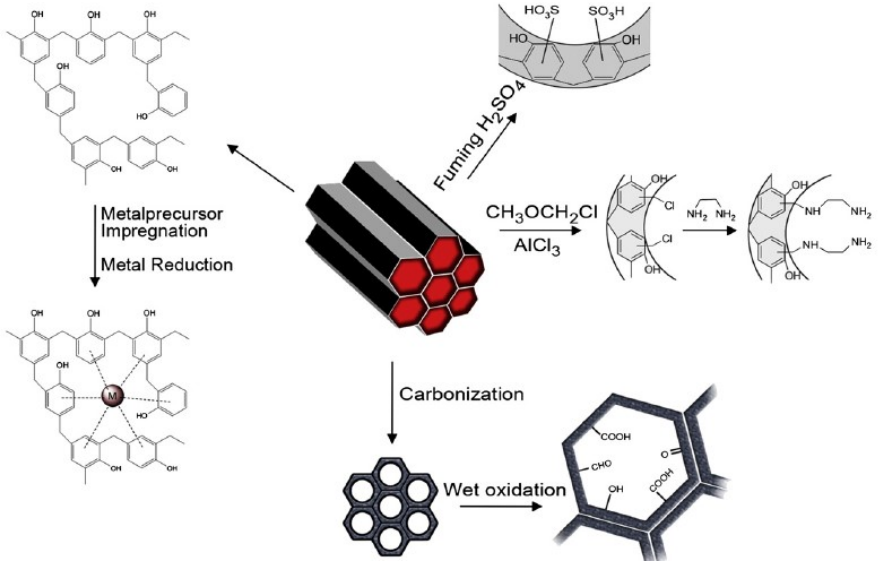

Figure 2. Schematic overview of the functionalization of ordered mesoporous phenolic resins.

Table 1 illustrated a summary of metal-doped phenolic resins as catalyst support. For this purpose, various transition metals such as Ir, Fe, Ru, Pd, Pt, Ti, etc. are, efficaciously dispersed in this structure. These materials were used for heterogeneous transition metal catalysts conventionally synthesized through two steps: first, impregnation of metal precursor on the surface of a porous solid support, second hydrogen reduction (e.g., borohydride reduction method) or chemical reduction (e.g., coordination alteration-induced redox by using ionic liquids) [16, 17]. The weak interactions between metal particles and the support are because of common reduction methods. Therefore, it was the main reason for partial oxidation, aggregation/sintering, and metal leaching during catalyst preparation [17]. To overcome this issue, Su et al. reported a thermal method to prepare different transition metals, such as Ru catalysts with uniform Ru nanoparticles dispersion in the OMR [17]. The metal reduction occurred during removing soft template at the

calcination stage simultaneously, reduced catalyst activity. On the other hand, the weakness of using the soft-template method for using phenol-formaldehyde resins as support is metal reduction. In fact, during the calcination stage in the soft-template method, CO, H_2, or other reducing species are produced due to the breakdown of block copolymer and pyrolysis of phenolic resin. These gases reduced the metal salt and formed metal nanoparticles [18]. Also, formaldehyde is known as a reducing agent, which is one of the most common carbon precursors of the phenolic resin. Palladium is one of the transient metal that is being used for the palladium-catalyzed cross-coupling reactions, reported for the first time in 1978. Research in this area has developed exponentially, and these transformations have become extremely versatile and powerful tools in the synthesis of drugs, natural products, and fine chemicals [19]. Thus, producing new heterogeneous Pd structures has attracted enormous interest. Reducing the cost of producing this catalyst and is very significant. Therefore, many researchers have tried to use new catalyst supporters. As mentioned above, OMR is a great candidate for this purpose. The first attempt for using ordered mesoporous material was reported in 2009. In this method, carbon-silica hydride materials were used as support for palladium chloride salt. This novel heterogeneous catalyst was evaluated for coupling reactions by using various aryl chlorides in aqueous media [20]. An evaporation method synthesized the hybrid support in the presence of ethanol as solvent. The first co-assembly of soluble phenolic prepolymer and TEOS around surfactant (F127) occurred. After co-assembly and curing, the resin was carbonized resulting in a mesoporous carbon-silica framework. This support was then impregnated in an aqueous solution of $PdCl_2$. Therefore, in this method, palladium was distributed in this support at the final stage of synthesis of the heterogeneous hybrid palladium catalyst. The

palladium was reduced by hydrogen. By using TEM analysis, no visible aggregation was detected. On the other hand, the metal nanoparticles were highly dispersed in the support matrix. The hybrid character of this material (silica and carbon components) can be attributed to the formation of a uniformly dispersed continuous network. This tendency of aggregation of palladium ions is significantly reduced due to selectively adsorption on the silica moieties of the framework. The lack of attraction for carbon sections plays an essential role in this homogeneity. The catalyst showed excellent performance, easy recoverability, and negligible leaching, as mentioned earlier, but this multi-stage process is time-consuming and expensive [21]. Fujian et al. developed a method to synthesize solvent-free OMR in a solid phase [22]. Fujian showed that palladium acetate could be distributed uniformly in the structure of ordered mesoporous resin to produce the active and reusable catalyst for the cross-coupling reaction family [23]. They addressed homogenous palladium distribution and stability. However, the main challenge for scale-up is the calcination procedure to remove the template [17].

Table 1

Overview of using phenol-formaldehyde resin application as the catalyst by incorporation of various elements and functional groups

Compounds	Precursor	Incorporat-ion	Support	C-precursor	Template	Reaction type	References
CaO	$Ca(NO_3)^{2\cdot}{}_4H_2O$	in-situ	OMC	PF	F127	Physi- and chemisorption CO_2	23

Table 1 (continued)

Compounds	Precursor	Incorporat-ion	Support	C-precursor	Template	Reaction type	References
F	p-fluorophenol	in-situ	OMC	PF	F127	Cyclic voltammetry	24
Ir	H_2IrCl_6	in-situ	OMC	RF	F127	Decomposition	25
Fe	$Fe(NO_3)^{3\cdot}{}_9H_2O$	post-synthesis	OMC	RF	F127	Catalytic wet peroxide oxidation	26
MoC	$(NH_4)_6Mo_7O^2{}^4{}_{.4}H_2O$	in-situ	OMC	RF	F127	Decomposition	28
Fe	$Fe(NO_3)^{3\cdot}{}_9H_2O$	in-situ	OMC	RF	F127	_____	27
Ni	$Ni(NO_3)^2$	in-situ	OMSC	RF	F127	_____	30
Ni	$Ni(H_2O)_6(NO_3)_2$	in-situ	OMC	RF	F127	_____	31
Pd	H_2PdCl_4	in-situ	OMSC	PF	F127	Heck coupling	32
Pd	Pd acetate	in-situ	OMSC	PF	F127	Cross-coupling	22
Pd	PdCl2	post-synthesis	OMC	PF	F127	Uman coupling	33

Table 1 (continued)

	Precursor Compounds	Incorport-ion	Support	C-precursor	Template	Reaction type	References
Pt	H_2PtCl_6	post-synthesis	OMP	PF	P123	Hydrodechlorination	34
Ru	$RuCl_3 \cdot 3H_2O$	in-situ	OMC	PF	F127	Hydrogenation	37
Ru	$RuCl_3$	in-situ	OMC	RF	F127	Hydrogenation	38
Ti	$Ti(OBu)_4$	in-situ	OMP	PF	F127	_____	41
$N(CH_3)_2$	DMA	post-synthesis	OMP	PF	F127	Beckmann	46
NH_2	ED	post-synthesis	OMP	PF	F127/P123	Condensation	47
SO_3H	50% SO_3/H_2SO_4 vapor	post-synthesis	OMP	PF	P123	Esterification	48
SO_3H		post-synthesis	OMP	PF	P123		49
NH2+Pd	1)ED, 2)H_2PdCl_4	post-synthesis	OMP	PF	F127/P123	Heck coupling, Hydrogenation	50, 22

Abbreviation; OMP: Ordered Mesoporous Polymer, OMC: Ordered Mesoporous Carbon, PF: Phenol-Formaldehyde

1.4 Carbon Dioxide Electrochemical Conversion

The CO_2 concentration in the atmosphere has significantly increased from 300 ppm in the preindustrial decade to 400 ppm in 2010[51]. The effect of carbon dioxide on global warming made it as the main greenhouse gas[52] [53]. Consequently, environmental concerns have been convinced the governments to take steps to change the CO_2 emission policy. One of the most remarkable strategies is capturing and converting technologies that are being developed to reduce it from main sources. Many methods have been suggested for converting CO_2 such as chemical, photocatalytic[54-55], and electrocatalytic reduction[56- 58]. Heterogeneous catalysts play the main role as a solid adsorbent and conversion. These include materials such as silica[59- 61], metal-organic frames (MOFs)[53], and carbon-based materials[52- 54]. One of the most commonly used adsorbents is carbon-based material. These are include activated carbon [15], ordered mesoporous polymer/carbon(OMP/OMC) [61-67], activated carbon fibers[68- 69], carbon graphene[64][52], and graphene oxide[70-72], which have been extensively used for this purpose. Regular pore structure, high surface area, and inexpensive precursor have potential advantageous OMP/OMC for CO_2 capture[61, 66-67]. The schematic for synthesis and functionalization of such OMR structures has been provided in Figures 1 and 2 [31]. Essentially, the main downfall is in producing cost-effective, feasibly of scalable, and eco-friendly catalysts that can afford a high ability to capture and convert CO_2 for the long-term[51, 63-64]. To increase the adsorption capacity and activity of this adsorbent, further functionalizing has been recommended [51,57,65]. Nitrogen functionalities generally provide basic sites for enhanced interactions with acidic CO_2. Typically, nitrogen doping is the most attractive. Utilization amid group can enhance

nitrogen bonding, which are the most common methods suggested to capture CO_2[59, 63, 66]. Fujian et al. showed nitrogen not only increased CO_2 capture but can feasibly anchor metal elements to polymer network for expediting CO_2 conversion. They synthesized ordered mesoporous phenol-formaldehyde polymer (N-OMP) by using hexamethylenetetramine (HMTA) as a source of nitrogen. N-OMP exhibited high stability, selectivity, and CO_2 capturing [57].

Polyethylenimine (PEI) is a multipurpose polymer with amine-containing repeat units, spaced out by the aliphatic ethylene CH_2CH_2 ligand[67]. As a result of high basicity, high amine content, good thermal stability, and low volatility. It is widely used to produce highly effective and stable functionalized adsorbents[68-69]. Silica[70, 71][1], nanocarbon tube, ordered mesoporous carbon, polymer [68, 72][2], and alumina [73] were modified by PEI. Due to the increasing nitrogen content of polymers, PEI functionalized Polymethyl methacrylate (PMMA), and polystyrene (PS)[72] showed high CO_2 adsorption capacity. However, despite these modified adsorbents having high CO_2 capturing properties, they have not yet been commercialized. The main hindrance is the multi-stages synthesizing method. It not only increases the cost of adsorbent, but it is not scalable as well[68- 74]. To overcome this barrier, Wang and colleagues developed organic amine-mediated synthesis of polymer with various types of amine for CO_2 capturing and energy storage[35].

Solid metal-doped polymers are an affective and environment-friendly catalyst for carbon dioxide conversion. Many researchers are agreeable to developing them because of high surface area, thermal stability, and activity [52]. As mentioned earlier, MOFs have also been reported as great adsorbents with good catalyst activity due to active metal sides

[53]. Cobalt, zinc, nickel, etc have been used extensively for this purpose. These metals not only enhance CO_2 capturing but also increase photo or chemical-electro conversion ability of MOFs. The solvothermal method is one of the conventional methods for metal-impregnated which these compounds to modify organic frame for improving the CO_2 capture and conversion rate[52-53].

This chapter focused on the potential of nitrogen-doped mesoporous polymer (MRF), with or without metal, for CO_2 capturing and electrochemical conversion. To facilitate the study of MRF, we focused on cobalt- doped MR. The effect of cobalt concentration and PEI concentration were considered on MRF properties such as surface area, pore size, pore structures and morphology, thermal stability, and elemental analysis. We used resorcinol and formaldehyde as precursor. In contrast to the multi-stage synthesis method, one-pot solvothermal synthesize method not only decreased the cost of production but it eliminated scalp- up barriers. In addition, a low temperature of synthesis without calcination stage makes it more ecofriendly. Its superior surface area and uniform mesoporous structure can be observed (from scanning electron microscopy (SEM)). The elemental analysis map confirmed homogenous metal distribution. This approach provides excellent feasibility for producing multi-metal catalysts, as well.

1.5 In-Situ Drug Synthesis

Surgery is the primary method of cancer treatment. Few patients elect to bypass this option, as it has considered necessary to stop cancer progression. Radiation therapy is the next step, which uses x-rays and other radioactive materials to damage DNA and cell membranes of cancer cells. Chemotherapy is the third step, which is the use of chemical agents to destroy dividing cells or stop their division [75]. The most popularly used

chemotherapeutic agent is cisplatin, which is a systemic antineoplastic treatment. This platinum-based antitumor drug has several disadvantages, including side effects, cisplatin-resistant tumors, limited solubility in aqueous media, and so on [76]. Another therapeutic approach that can be used throughout the treatment process is hormone therapy; however, this is only effective against types of cancer [77-80]. Therefore, there is an urgent need to (a) improve current chemotherapy efficacy, (b) develop new therapeutic drugs, and (c) identify a novel cancer drug target [81-82]. Transition metal-mediated activation of caged fluorophores has found a variety of applications in chemical biology [83-85]. Trapped palladium nanoparticles within inert polymeric microspheres were used as heterogeneous palladium catalysts in mammalian cells for the first time by Bradley et al. They created a ligand-free heterogeneous palladium catalyst [86]. This built upon work, which demonstrated the routine and practical delivery of polymeric microspheres into cells. They were loaded with a variety of cargos, ranging from sensors to proteins and nucleic acids [87]. Thus, engineered polystyrene microspheres (0.3–0.5 μm in diameter) were employed as "Trojan-horses" to deliver palladium nanoparticles into a living system, where the entrapped palladium was used to catalyze the C–C bond formation *via* Suzuki-Miyaura cross-coupling reactions [86-88]. In this scope, the deprotection chemistry was expanded with "on-site" production of an anticancer drug. Deprotection achieved synthesis of allylcarbamate-protected Amsacrine by Pd (0)-microspheres, in which the cells were dying as a result of the drug decaging [87-89]. The utility of Pd (0)- resin was envisioned for the intratumoral implantation of Pd (0) functionalized devices for exclusive activation of prodrugs within the cancerous tissue, consequently reducing the side effects of chemotherapy.

Weiss et al. applied this concept and showed the extracellular activation of a pro-drug in the presence of a Pd (0)-resin [85,88]. In these reports, Yusop [82] and Cho [83] developed the highly active heterogeneous catalytic system by converting the caged 5-fluorouracyl (5FU) and Gemcitabine analogues to their active forms in colorectal HCT116 and pancreatic BxPC-3 cancer cell lines. 5-Propargyl fluorouracyl (Pro-FU) released the 5-FU within 24 h, producing an effect comparable to the 5-FU antiproliferative activity. Similarly, the cytotoxicity of Gemcitabine was decreased (> 23-fold) by *N*-propargyloxy carbamate functionalization of the 4-amino group [88]. In-vivo Pd (0) biocompatibility was investigated by introducing a single Pd (0)-resin in the yolk-sac of zebrafish, which indicated the healthy development of an egg into larvae stage without cytotoxicity and phenotypic alteration [89]. These studies elegantly demonstrated the ability of Pd(0)-based heterogeneous catalysts to stay harmlessly around cells for days and to catalyze the synthesis of molecules from nontoxic intermediates or prodrugs, thus limiting the side effects associated with the cytotoxic compound.

1.6 Dissertation Summary

Mesoporous phenol-formaldehyde resins are a great candidate for an extensive application such as adsorbent, super capacitance, and catalyst. This research was focused on two main goals; first developing eco-friendly and scalable methods for producing resorcinol-formaldehyde as a catalyst to overcome the main drawback for industrial application of OMR, second evaluating the catalytic applications such as drug synthesis on a chip, carbon dioxide capturing/ conversion, and in-situ drug synthesis for cancer treatment. For reaching these goals, following steps were carried out.

1. First, a new template-free method was developed by using one-step copolymerization of resorcinol and formaldehyde with Polyethyleneimine (PEI). Due to the high surface area of the catalyst and flexibility of the synthesis method, Pd-MPR was chosen as support for producing heterogeneous palladium catalysts for pharmaceutical and biomedical applications. We focused on the synthesis and characterization of palladium-doped-mesoporous phenol-formaldehyde resin (Pd-MPR). The results were reported in Chapter four. Template-free MR catalyst was developed by the solvothermal method to reduce the cost of the product and increase the efficiency of the catalyst. This new method overcomes scale-up obstacles of calcination and multiple steps associated with standard methods for producing heterogeneous palladium catalysts. Surface area analysis based on the BET method, SEM, EDAX, XRD, and XPS were used to characterize the catalyst. Also, catalyst efficiency was evaluated in batch and continuous (microreactor model) for various Suzuki-Miyaura cross-coupling reaction.

2. A series of mesoporous metal-doped polymers (MRFs) with tunable metal functionality and hierarchical porosity were successfully synthesized. As showed in Chapter five, cobalt and nickel heterogeneous catalysts were synthesized by one-step copolymerization of resorcinol and formaldehyde with Polyethyleneimine (PEI) under solvothermal conditions. The effect of PEI and metal doping concentrations were observed on physical properties and adsorption. The results confirmed the role of PEI in increasing the mesoporosity of the polymer networks and surface area. Besides, it enhanced CO_2 capture capacity. The resulting Cobalt doped material shows proper thermal stability and promising CO_2 capture performance. With its ease of synthesis, this catalyst is a promising candidate for promising for CO_2 capture and subsequent electrochemical conversion.

3. The biomedical application of the palladium catalyst was chosen goal in Chapter six. The catalyst biocompatibility was evaluated by using Presto-Blue, Live/Dead Assay. Also, cell morphology was considered by actin and DAPI essay during culture time (7 days) in the presence of the catalyst. Finally, the efficiency of in-situ drug synthesis was considered. For this stage, the cell viability of the prostate cell line (PC3 cells) was evaluated by Presto-Blue, Live and dead, flow cytometry assay in 2D and 3D in-vitro models.

Chapter 2

Characterization Methods

2.1 Introduction

Throughout the work of this thesis, a new solvothermal method is developed to produce mesoporous phenol-formaldehyde resin. Various methods were employed to characterize and evaluate the application of these materials described below. The goals of this chapter are to provide a basic overview of the essential characterization methods and explain the theory behind each technique. The techniques were used include scanning electron microscopy (SEM), elemental analysis (EDAX), Brunaur-Emmett-Teller (BET), thermogravimetric analysis (TGA), electrochemical conversion test (chronopotentiometry, linear sweep voltammetry), gas chromatography (GC), and biological test (biocompatibility, drug screening).

2.2 Thermal Gravimetric Analysis

Thermal stability of material is measured by thermal gravimetric analysis (TGA). The sample is held under oxidative (air or oxygen) or inert (nitrogen) environments. Three types of thermal gravimetric analysis are common;

1) Isothermal or Static Thermogravimetry: The sample weight is recorded as function of time at constant temperature.

2) Quasistatic Thermogravimetry: The sample is heated to a constant weight at each of increasing temperatures.

3) Dynamic Thermogravimetry: The sample is heated in an environment whose temperature is changed in a linear manner.

Mass changes are monitored and recorded versus temperature or time. Various thermal procedures can occur vaporization, oxidation, decomposition, etc. [90]. In this

study, TGA was measured under nitrogen atmosphere by a TA instrument. Two types of pans were used; ceramic and platinum. The pans were heated at the same rate, and the mass change was plotted against temperature. The plot shows the decomposition profile of the sample (a decrease in mass).

Applications of TGA include analysis of thermogravimetric kinetics, thermal stability, and oxidation or combustion behavior. If the TGA is run in pure nitrogen conditions, it can also show the behavior of the sample under anaerobic oxidation. Many different methods can be used to determine the activation energy by analyzing the TGA data.

The Arrhenius equation describes how the temperature of a material affects the kinetic rate constant, k. the equation is shown below.

$$k = Ae^{\frac{-E_a}{RT}} \quad \text{(Eq 1)}$$

Here A is the pre-exponential factor, E_a is the activation energy, T is the absolute temperature, and R is the gas constant. This equation can be used in the overall kinetics equation (Eq 2-3), which describes the conversion of a material as a function of the kinetic rate constant and the chosen reaction model.

$$\frac{d\propto}{dt} = k(t) * f(\propto) \quad \text{(Eq 2)}$$

Where

$$\propto = \frac{m_i - m_a}{m_i - m_f} \quad \text{(Eq 3)}$$

In this last equation, the initial mass, final mass, and actual mass is represented by m_i, m_f and m_a respectively. In the case of non-isothermal conditions, this equation can be modified by incorporating the equation 4 -5 for the heating rate.

$$B = \frac{dT}{dt} \quad \text{(Eq 4)}$$

$$\frac{d\propto}{dT} = \frac{k(t)}{\beta} * f(\propto) \quad \text{(Eq 5)}$$

By replacing k(t) for the Arrhenius equation, a final equation is obtained;

$$\frac{d\propto}{dT} = \frac{A}{\beta} * e^{\frac{-E_a}{RT}} * f(\propto) \quad \text{(Eq 6)}$$

Flynn-Wall-Ozawa (FWO) method, the Kissinger method, and the Kissinger-Akahira-Sunose (KAS) methods are suggested to determine activation energies and pre-exponential factors of degradation kinetics [91].

FWO method: the natural logarithm of the heating rates plots against $1000/T_{\alpha i}$. Here the activation energy can be calculated from the slope of the line (Eq- 7). To obtain the method, Doyle's approximation is used for temperature integration:

$$g(\propto) = \frac{A}{\beta} 0.00484 e^{-1.052\frac{E_a}{RT}} \quad \text{(Eq 7)}$$

Therefore, by taking the natural log of Eq 7, the heating rate at the FWO model is obtained:

$$\mathrm{Ln}(\beta) = \ln\left(\frac{AE_a}{\mathrm{R}g(\propto)}\right) - 5.331 - 1.052\frac{E_a}{RT} \quad \text{(Eq 8)}$$

Here g(α) is a constant at a given value of conversion.

Kissinger method similarly allows one to determine the activation energy from the slope but incorporates the temperature peak obtained in the differential thermal gravimetric curve, T_m. The equation 9 is shown below.

$$\mathrm{Ln}\left(\frac{\beta}{T_m^2}\right) = \ln\left(\frac{AR}{E_a}\right) - \frac{E_a}{RT_m} \quad \text{(Eq 9)}$$

The KAS method uses the Coats-Redfern approximation instead of the Doyle approximation. Similarly, this approximation can be rearranged to solve for the natural logarithm of β. This can be seen below [91, 92].

$$g(\propto) = \frac{A}{\beta}\frac{T^2}{E_a}e^{-\frac{E_a}{RT}} \quad \text{(Eq 10)}$$

$$\mathrm{Ln}\left(\frac{\beta}{T^2}\right) = \ln\left(\frac{AE_a}{Rg(\propto)}\right) - \frac{E_a}{RT} \quad \text{(Eq 11)}$$

TGA can also be used to gauge the thermal stability of a material. This is useful for determining if the material can function in the desired range as well as determining the temperature at which it begins to degrade. In thermally stable materials, there should be no mass change in the material over the given temperature range. Given that a material does degrade and decrease in mass, and given the temperature and composition of the material, one could determine the manner in which different components may be degrading or if there are any impurities in the material [90-92].

2.3 Scanning Electron Microscopy

Scanning Electron Microscopes (SEM) is used for scanning the surface of materials with a focused beam of electrons from the various signals produced by the electrons interacting with the sample. The various numbers of electron-sample interactions can reveal information about the sample's chemical composition, crystalline structure, orientation, and external morphology. When accelerated electrons are emitted onto an example, they can pass through without interaction, undergo elastic scattering, or be inelastically scattered. Signals from elastic and inelastic scattering can result in signals such as secondary electrons, backscattered electrons, cathodoluminescence, auger electron, and characteristic x-rays. The electron beam impinges on the surface of a sample. The electron interaction volume is generated by electron scattering, photon, and X-ray production [93, 94].

Depending on the energy of the incident beam, the mean atomic weight, and the angle of the impinging electron beam, the electron interaction volume can be increased or

decreased. Different electron interaction volumes can then produce different signals that are characterized by different resolutions. For example, signals that are generated in the highest volume generally have lower resolutions. For imaging of samples secondary electrons and backscattered electrons are commonly used. Secondary electrons are used for showing morphology and topography while backscattered electrons are used to illustrate contrast in composition in multiphase samples. During inelastic collision, elements are excited in the sample by the electron beam and produce X-rays as the excited electrons return to lower energy states. These X-rays are produced at fixed wavelengths relative to the given element they are generated from, enabling elemental analysis of specific materials [94].

The SEM instrumentation itself is made up of several components- namely, an electron source, electron lenses, sample stage, detectors, and display [95]. In addition to these key components, the machinery must prevent vibration to the machine, provide a vacuum in the sample chamber, provide cooling to specific elements, and power the instrumentation. The instrumentation operates by producing electrons from the electron gun. This gun is placed at the top of a column that contains a combination of lenses and apertures designed to focus the beam onto the sample positioned at the bottom of the column. Prior to analysis, the column and chamber are evacuated and kept at vacuum for the operation of the microscope [95, 96].

2.4 Brunauer-Emmett-Teller (BET) Analysis

There are many structural factors that contribute to a material's available surface area, such as porosity, average pore size, pore shape, and particle size. Using Brunauer-

Emmet-Teller (BET) analysis, it is possible to measure the surface area of materials and draw conclusions about its structure [97].

BET analysis is named for Stephen Brunauer, Paul Hugh Emmet, and Edward Teller, who are contributed to writing the paper in 1938 that proposes the theory of using multi-molecular adsorption processes to determine surface area. By exposing materials to various relative pressures and measuring the adsorbed gas to the surface of the particles, correlations can be made between the adsorbed gas and the surface area of the material. Furthermore, correlations can be made between the relative pressure at which the gas is adsorbed, the shape of the isotherm measured, and the size and shape of the pores, respectively. The method for this analysis will be explained later. Before discussing the theory and use of BET analysis, a note must be made concerning the Langmuir theory on which BET theory is based [98].

The first assumption in Langmuir theory is that the surface is homogeneous [96]. In other words, this assumption states that the adsorption of gas occurs equally across the whole material. This assumption discounts the existence of preferred adsorption sites within a material and treats the material as either one material or a uniformly distributed mixture. All other interactions, including interactions between gas-phase molecules, non-sorption interactions between gas and adsorbed gas molecules, and lateral interactions between adsorbed molecules, are not considered in this theory [96]. The third assumption is that the adsorbed surface exposed is in equilibrium with the gas phase molecules. This assumes that the system is at saturation when measured. The last assumption, which is unique to Langmuir theory, is that only one monolayer of adsorbed gasses forms [96, 97].

At the surface of the material, the adsorption reaction can be represented by the following equation [96].

$$A(g) + S(surface) \leftrightharpoons AS(surface) \quad \text{(Eq 12)}$$

Where

$$Rate\ of\ adsorption = k_1 PN(1-\theta) \quad \text{(Eq 13)}$$

$$Rate\ of\ desorption = k_{-1} N(\theta) \quad \text{(Eq 14)}$$

Here, P represents the pressure above the surface, N is the total number of sites, and θ is the fraction of the occupied sites over the number of available sites. Since it is assumed that each site can only be occupied by one molecule, this fraction can also be equal to the number of molecules adsorbed over the number of molecules in one monolayer. Furthermore, the product of θ and N gives us the total number of occupied sites and the product of (1-θ), and N is the total number of empty sites. Expressing the rate of change of θ in respect to time and applying the assumption that at our system is at equilibrium, meaning that the change is effectively zero, we obtain the following equations [96].

$$\frac{d\theta}{dt} = k_1 PN(1-\theta) - k_{-1} N(\theta) \quad \text{(Eq 15)}$$

$$\theta = \frac{k_1 P}{k_1 P + k_{-1}} \quad \text{(Eq 16)}$$

Additionally, this equation simplifies through the introduction of the binding equilibrium constant.

$$K = \frac{k_1}{k_{-1}} \quad \text{(Eq 17)}$$

$$\theta = \frac{KP}{KP+1} \quad \text{(Eq 18)}$$

This relationship shows that as the binding equilibrium constants increasing with magnitude, the rate of change for θ overpressure increases likewise. Effectively this means that as the K value increases for a certain material, the pressure at saturation decreases. While Langmuir theory provides a good approximation for this process, it inaccurately represents the behavior of nitrogen as it adsorbed to a surface. As discussed, Langmuir theory assumes that gas molecules are adsorbed randomly into available sites until one complete monolayer is formed. In reality, many layers form during the adsorption process, with certain layers not being completed before the next layer forms [96- 98]. As BET theory is based on Langmuir theory, all previous assumptions apply with the exception that many, rather than one, layers are formed during adsorption. When adsorbed, molecules can act as a single sorption site for another gas molecule. Another assumption states that surface adsorption kinetics are limited by kinetics rather than diffusion constraints [97]. In this assumption, the heat required for gas molecules for the first layer to adsorb is equal to the heat of adsorption. The energy required for each subsequent layer is based on the heat required for condensation as each subsequent layer is treated as a condensed liquid. Regardless of the current layers of molecules adsorbed, the heat required for more molecules to adsorb remains the same. Lastly, it assumes that the number of adsorbed layers is such that the material is completely surrounded by adsorbent at the saturation pressure [96. 97]. In BET theory certain values change due to the presence of multiple layers.

$$\theta \; becomes \; \theta_n = \frac{number \; of \; sites \; with \; n \; absorbed \; molecules}{number \; of \; sites \; total} \qquad \text{(Eq 19)}$$

$\frac{d\theta_0}{dt} = rate\ of\ evaporation\ from\ 1st\ layer -$

$rate\ of\ condensation\ onto\ bare\ surface$

(Eq 20)

$$\frac{d\theta_0}{dt} = Nk_{-1}\theta_1 - Nk_1P\theta_0 \quad \text{(Eq 21)}$$

$$\theta_1 = P\frac{k_1}{k_{-1}}\theta_0 \quad \text{(Eq 22)}$$

Here Nθ_1 is the number of sites with 1 layer of nitrogen on it and Nθ_0 is the number of sites with no nitrogen absorbed. For subsequent layers, this relation becomes more complex but can be generalized to follow a specific pattern.

$\frac{d\theta_n}{dt} = rate\ of\ condensation\ onto\ (n-1)\ layer\ + rate\ of\ evaporation\ from\ (n+1)\ layer - rate\ of\ condensation\ onto\ n\ layer -$

$rate\ of\ evaporation\ from\ n\ layer$ (Eq 23)

$$\frac{d\theta_n}{dt} = Nk_nP\theta_{n-1} + Nk_{-(n+1)}P\theta_{n+1} - Nk_{(n+1)}P\theta_n - Nk_{-(n)}P\theta_n \quad \text{(Eq 24)}$$

$$\theta_n = \frac{k_n}{k_{-(n)}}P\theta_{-(n-1)} \quad \text{(Eq25)}$$

$$\theta_n = \frac{k_n}{k_{-(n)}}\frac{k_{n-1}}{k_{-(n-1)}}\frac{k_{n-2}}{k_{-(n-2)}}\ldots\frac{k_1}{k_{-1}}P^i\theta_0 \quad \text{(Eq26)}$$

For all layers other than the first, BET theory assumes the nitrogen is liquid like, as such:

$$k_2 \cong k_3 \cong k_4 \cong k_i \neq k_1 \quad \text{(Eq 27)}$$

$$k_{-2} \cong k_{-3} \cong k_{-4} \cong k_{-i} \neq k_{-1} \quad \text{(Eq 28)}$$

Where k_i is the rate of adsorption onto the liquid nitrogen surface and k_{-i} is the rate of desorption off a liquid nitrogen surface. Here BET theory defines x and c, simplifying the equation.

$$x = P\frac{k_n}{k_{n-1}} \quad \text{(Eq 29)}$$

Resulting in:

$$\theta_n = x^{n-1}P\frac{k_1}{k_{-1}}\theta_0 \quad \text{(Eq 30)}$$

Define c thus:

$$c = P\frac{k_1}{xk_{-1}} \quad \text{(Eq 31)}$$

Resulting in:

$$\theta_n = x^n c\theta_0 \quad \text{(Eq 32)}$$

In general, it can be said that the total surface coverage, θ, is equal to the total number of molecules adsorbed, n_a, over the total number of sites, n.

$$\theta = \frac{n_a}{n} = \frac{\sum_{n=0}^{\infty} n\theta_n N}{\sum_{n=0}^{\infty} \theta_n N} = \frac{\sum_{n=1}^{\infty} n\theta_n}{\theta_0 + \sum_{n=1}^{\infty} \theta_n} = \frac{c\theta_0 \sum_{n=1}^{\infty} nx^n}{\theta_0 + c\theta_0 \sum_{n=1}^{\infty} x^n} \quad \text{(Eq 33)}$$

Using the relationship.

$$\sum_{n=1}^{\infty} x^n = \frac{x}{1-x} \quad \text{(Eq 34)}$$

We can say.

$$\sum_{n=1}^{\infty} nx^n = x\sum_{n=1}^{\infty} nx^{n-1} = x\sum_{n=1}^{\infty} \frac{d}{dx}x^n = x\frac{d}{dx}\frac{x}{1-x} = \frac{x}{(1-x)^2} \quad \text{(Eq 35)}$$

Substituting this relationship, the equation above is simplified in order to obtain.

$$\theta = \frac{c\theta_0 \frac{x}{(1-x)^2}}{\theta_0 + c\theta_0 \frac{x}{1-x}} = \frac{cx}{1-x} * \frac{1}{1-x+cx} = \frac{cx}{(1-x)(1+(c-1)x)} \quad \text{(Eq 36)}$$

At equilibrium, this equation simplifies further. At equilibrium, the rate of adsorption equals the rate of desorption meaning $k_1 PN = k_{-1}N$. Furthermore, the pressure of the system is equal to the vapor pressure of pure nitrogen, P_o, at the temperature of the experiment. These assumptions combined simplify x as the pressure of the system over the

vapor pressure of nitrogen. Substituting in this new x value and converting θ to volume, we can obtain the generalized BET equation [97].

$$v = \frac{v_m c P}{(P_o - P)\left(1 + (c-1)\frac{P}{P_o}\right)} \quad \text{(Eq 37)}$$

Where v represents the volume of adsorbed gas, and v_m is the adsorbed monolayer volume. This equation can be rearranged into a linear function of P/P_o [87].

$$\frac{1}{v\left(\left(\frac{P}{P_o}\right)-1\right)} = \frac{c-1}{v_m c}\left(\frac{P}{P_o}\right) + \frac{1}{v_m c} \quad \text{(Eq 38)}$$

As the BET machine varies the pressure and measures the volume, the values of c and v_m can be calculated from the slope and intercept. Using the calculated value, v_m, surface area, S, can be calculated with the following equation [96- 98].

$$S = \frac{v_m N_A A}{22{,}400 * m} \quad \text{(Eq 39)}$$

Where N_A is Avogadro's number, A is the cross-sectional surface area of a single adsorbed gas molecules, m is the mass of the material being tested, and 22,400 represents the standard temperature and pressure-volume of one mole of gas [98].

2.5 Chronopotentiometry

An instrument frequently used in the course of this work was a Model 600E Series Electrochemical Analyzer/Workstation. This instrument contains both a potentiostat and a galvanostat, enabling it to perform potential and controlled current experiments. The electrochemical cell uses a three-electrode configuration consisting of a working electrode, auxiliary electrode (counter electrode), and a reference electrode. In this configuration, a current is applied between the auxiliary and working electrodes while monitoring the potential of the working electrode against the reference electrode.

In a traditional battery, chemical reactions create a potential difference between the anode and cathode terminals that causes an electromotive force or voltage. On the anode side, a chemical reaction occurs between the electrolyte and the anode producing free electrons, which causes a buildup of negative charge at the terminal. While the anode is known as the reducing agent, we call the process of losing electrons oxidation. Similarly, on the cathode side, a similar chemical reaction occurs but produces an excess of positive ions building up a positive charge at the terminal. The process of gaining electrons here is called reduction, and the cathode is known as the oxidizing agent. The electrolyte functions as a medium for the transfer of charge, providing ionic conductivity. Metal ions, also known as cations, move through the electrolyte towards the positive electrode.

When initially subjected to the current, the measured potential changes due to iR loss but gradually change as the concentrations of the reactants and products change. To support an applied current, a redox reaction must occur at the surface of the working electrode. This leads to the reduction of chemical elements in the material. For example, when ferric oxide is reduced, it gains an electron and becomes ferrous oxide. By analyzing the behavior of the potential difference between the working electrode and the reference electrode in each type of chronopotentiometry technique, we can characterize the performance of the electrode material [99].

As this constant current is applied, the electroactive species is oxidized/reduced at a constant rate. This can be represented by the equation below:

$$O + e^- = R \qquad \text{(Eq 40)}$$

Where O is the concentration of the oxidized form the electrochemical species, and R is the reduced form. The active concentrations of O and R will determine the potential of the system, which can be calculated using the Nernst equation below [88]:

$$E = E^0 - \frac{RT}{nF} \ln \frac{C_O}{C_R} \qquad \text{(Eq 41)}$$

Where C_O and C_R are the surface concentrations of O and R respectively, E^0 is the standard reduction potential, n is the number of electrons transferred per redox reaction, R is the molar gas constant (8.314 $Jmol^{-1}K^{-1}$), T is the absolute temperature (K), and F is Faraday constant (96,485 C/equiv) [88].

Once the oxygen drops to zero at the surface of the electrode, the potentials will level off at the redox potential for the reaction. Due to an inability for the electrodes to continue to accept electrons being forced by the application of constant current.

The current is a quantitative measure of how fast a species is being reduced or oxidized at the surface of the electrode. While the current is affected by many material aspects of the electrode and electrolyte, such as shape, size, species, solution resistance, cell volume, and number of electrons transferred, the available concentrations of the redox series has a huge role. As these redox reactions occur at the surface of the electrode, it creates a concentration gradient for the oxidized species concentration between the bulk solution and the electrode surface that can be represented and described by Fick's law [88].

Chapter 3

Experimental Methods

3.1 Introduction

The list of materials and methods by which they were utilized is discussed in this section. Included in the list of materials is the purity of the chemical used and where it was purchased or obtained. The method for fabrication, including the electrospinning aspects and subsequent heat treatment of the metal-doped carbon material, will be discussed. The development of the bio-ink used to print the batteries will also be discussed. Lastly, the method and experimental design used to analyze the fabricated materials will be discussed.

3.2 Materials

3.2.1 Gelatin methacrylate (GelMA) synthesis. Polymers and chemicals synthesized in this work include GelMA, choline bitartrate, and polyglycerol sebacic acid acrylate. GelMA was synthesized in several steps. Gelatin Porcine Skin was added to PBS at 50°C in a 10 w/v% until melted. 6 mL Methacrylic Anhydride was added dropwise into the solution and stirred at 50°C for 2 hours. The reaction was then quelled by adding an equal volume of PBS preheated to 50°C. The solution was left to sit for 10 minutes and then transferred into dialysis membranes. These membranes containing the solution were placed into distilled water at 40°C for 7 days. The water surrounding the membranes was changed twice daily. Afterward, the solutions in the membranes were transferred to a beaker containing 200 mL of distilled water and stirred for 15 minutes at 40°C. The solution was transferred into 50 mL Falcon tubes, each containing 30 mL of the solution.

Tubes are then stored horizontally at -80°C to freeze. The frozen GelMA was then freeze-dried for several days until all water was removed from the tubes.

3.2.2 Mesoporous phenol- formaldehyde resin (MRP) synthesis. MPRs and metal doped MPRs were synthesized in one-step by the solvothermal reaction between resorcinol, formaldehyde and ethanolic-PEI/ aqueous-PEI solution. For MPR, 1.5 g resorcinol was dissolved in 4.4 mL of distilled water with vigorous stirring in a water bath (40 ºC) to obtain a clear solution. Then, 5.6 mL of 1.96 or 3.93 w/v% aqueous or ethanolic PEI solution was added to it and kept in the water bath for 15 minutes. Finally, 2.1 mL of formaldehyde (37% in water) was injected at high stirring speed (up to 750 rpm). After 20 minutes, the solution was poured in a Teflon hydrothermal autoclave chamber and baked for 12 hours at 120 ºC.

To synthesize metal-doped MPRs, after the reaction of resorcinol and PEI, a proper amount of metal salt was added and stirred gently for 20 min. Then formaldehyde (37% in water) was injected quickly. Other stages were the same as MRPs. Prepared catalyst was smashed and washed with DI water and ethanol 3 times and finally dried under vacuum at room temperature. The catalyst was ground and sieved for reaction efficiency consideration. Resorcinol- Formaldehyde resin (RF) synthesized as a control. The ratio of resorcinol and formaldehyde was as same as MRPs.

3.3 Thermal Gravimetric Analysis

TGA samples were prepared by preheating the samples at 50 °C in the vacuumed oven overnight. To analyze samples, a TA Instruments Discovery TGA 550 was used. 100 µL platinum pans were cleaned using a blowtorch and tared prior to loading the sample. Between 10 to 20 mg of sample was used for each test. Samples were run in an inert

atmosphere of nitrogen. The sample flow rate was set to 100 mL/min and the balance flow was set at 100 mL/min. Each sample underwent the same procedure of equilibration at 150 °C followed by a ramp heating of 10 °C/min to 700 °C. Afterwards samples were air cooled for 15 minutes.

3.4 SEM Analysis

For all SEM analysis, samples were prepped in the same manner. Samples were fixed onto 25 mm sample stubs using double sided ahesive carbon tape. The surface of the sample was sprayed with a can of supressed air to remove any loose particles.

Two machines were used to obtain SEM images. Electrode samples images were taken at a magnification of 100000X while EDX images were taken at a magnification of 5000X. For samples requiring EDX analysis, a ThermoFisher Quattro ESEM was used.

3.5 BET Measurements

To obtain data on the pore size, pore volume, and surface area of the carbonized material, BET measurements were conducted on the samples. 9 mm samples bulbs were used in these tests. Samples were degassed at 110°C for 24 hours. Samples were analyzed using nitrogen, and a full isotherm was conducted on the samples. During adsorption, 15 evenly spaced data points between 0.005 and 0.99 P/Po were taken while 15 points were taken for desorption.

3.6 Electrochemical Testing

Electrodes were tested in various ways based on material type. For all tests, a Model 600E Series Electrochemical Station from CH Instruments was used with electrodes provided by Bioanalytical Systems, Inc. Electrodes based on the parametric designed outlined above were tested to compare the electrical properties of the carbon material. Secondly, CO_2 electrochemical conversion electrodes based on the saturated electrolyte

solution by CO_2 or argon were tested. The two ways are outlined in the following subsections. For all electrochemical experiments in this work, an electrochemical cell, like the one shown in Figure 3 was used. The cell was comprised of a working electrode on which sample was placed, a counter electrode, and a reference electrode within a glass reservoir. In this three-electrode set-up, the current flows between the working and counter electrodes. Using the reference electrode, the applied potential is measured by comparison against a reference reaction.

3.7 Electrochemical Conversion Testing

3.7.1 Electrodes fabrication. Electrodes were fabricated from material set onto MF-2012 3.00 mm diameter Glassy Carbon electrodes. MR catalyst was ground into a fine powder using a mortar and pestle. 20 mg dissolved in 800 mL of 10 weight percent poly(vinylidene fluoride) (PVDF) in N-methyl-2-pyrrolidone (NMP). 30 mL of this solution was deposited onto the surface of the glass carbon and was left to the oven at 40 °C for 30 min. To test the electrochemical properties of the material, chronopotentiometry tests were conducted. 5 uA of current was applied to the electrodes over 30 min. Sodium hydrogen disulfide 1 M was used as an electrolyte, a MF-2113 3 mm diameter platinum electrode was used as a counter electrode, and a MF-2052 Ag/AgCl 3M NaCl electrode was used as the reference electrode. For the electrochemical conversion test, at first electrolyte solution was purged by carbon dioxide or argon based on an experiment. Then working and counting electrode immersed in the electrolyte solution and blanked by gas

during the experiment. The reference electrode was immersed in another container and two containers connected by a salt bridge (figure5).

3.7.2 Electrolyte testing. The ionic liquid electrolyte was tested using chronopotentiometry and A.C. impedance to measure the potential and conductivity of the electrolyte against a standard. Chronopotentiometry tests utilized a current 50 nA with an anodic polarity. The current switching priority was set to a 30-hour time limit to enable the tests to run until a stable potential value was reached. For the A.C. impedance tests, a voltage of 0.1 V, high frequency of 100000 Hz, low frequency of 1 Hz, and quest time of 60 s was used. For the cell set-up in both tests, a blank MF-2012 3.00 mm diameter Glassy Carbon electrode was used as the working electrode, a MF-2113 3 mm diameter platinum electrode was used as the counter electrode, and MF-2052 Ag/AgCl 3M NaCl electrode was used as the reference electrode. The set-up is shown in figure 3.

Figure 3. Caron dioxide electrochemical conversion set-up

3.8 Biology Testing

3.8.1 Cell culture. Prostate cancer cell line (PC3 cells) was cultured in RPMI-1640 containing 10% FBS and 1% penicillin/ streptomycin. The media was changed every two days. Trypsin 0.05% was used for trypsinizeing and passaging the cells.

For the 3D drug screening model, cells were encapsulated in GelMA- alginate hydrogel. GelMA and alginate powder were dissolved in PBS separately and sterilized by syringe filter 0.2 µm. Lithium phenyl-2,4,6-trimethylbenzoylphosphinate (LAP) was used as a photoinitiator and dissolved in PBS. For cell encapsulation, GelMA, alginate, and LAP solutions were mixed to the desired concentration, and then cell suspension was ($5* 10^{-6}$ cells/ml) added to it. 7 µl of this solution was put between spacers. Then it was covered by TMSPMA coated glass and cross-linked by visible light (intensity 400%) for 30S. Hydrogel which was formed on the surface of coated glass, and transferred into 12 well plate contained media.

3.8.2 Cell viability. The viability of PC3 cells grown on the surface of MR-Pd hydrogels was evaluated using a commercial Live/Dead viability kit (Invitrogen), according to instructions from the manufacturer. Briefly, cells were stained with 0.5 µl/ml of calcine AM and 2 µl/ml of ethidium homodimer-1 (EthD-1) in PBS for 5 min at 37 °C. Fluorescent image acquisition was carried out at days 1, 3, 5, and 7 post-seeding using an Axio Observer Z1 inverted microscope (Zeiss). Viable cells appeared as green and dead cells appeared as red. The number of live and dead cells was quantified using the ImageJ

software. Cell viability was determined as the number of live cells divided by the total number of live and dead cells.

3.8.3 Cell proliferation. The Presto/Blue assay was carried out in 12-well. Each well contained the cells to be tested with cultured medium or rinsing solution removed. 500 µl (for 12-well plates) Presto/Blue solution (10% in medium without serum) was added to each well, and the plates were incubated at 37 °C for a specified time period. Simultaneously, fresh serum-free media were incubated in a new well plate as blank. After incubation, 100 µl of the Presto/Blue solution from each well of the assay plates (96-well plates) was transferred to a new well in 96-well plate, and the change in the fluorescence of the test reagent was measured in the new plate using a fluorescence multi-well plate reader with the excitation/emission wavelengths set at 530/590 nm.

3.8.4 Cell viability for drug screening. The Muse® Annexin V & Dead Cell Kit was applied for the quantitative analysis of live, early, and late apoptosis and cell death cells on the flow cytometer (Guava® Muse® Cell Analyzer). Concentrations (cells/mL) and percentage for live, early apoptotic, late apoptotic, total apoptotic, and dead cells were calculated by MUSE software. For monolayer culture, cell scraper was used to detach cells. Then 20 µl of cell suspension was mixed with 20 µl of Muse® Annexin V & Dead Cell solution and incubate in a dark place at room temperature for 20 min. Then the sample was placed in the flow cytometer and ran the ® Annexin V & Dead Cell assay. Each sample was measured three times.

Chapter 4

One-Pot Aqueous and Template-Free Synthesis of Mesoporous Polymeric Resins

4.1 Introduction

Research interest in the subject of mesoporous polymeric resins (MPRs) has been current and extensive, with their applications spanning selective adsorption and water treatment, separation and insulation, and the field of heterogeneous catalysis [107-119]. MPRs proffer intrinsic characteristics such as tunable structures with tailorable mesopores size (2–30 nm) [120-128]. These are distinct advantages when compared to porous organic polymers entailing crystalline covalent organic or aromatic frameworks, conjugated microporous polymers, or mesoporous polydivinylbenzene. The active sites in MPRs structures are more accessible to substrates and hence provide superior catalytic activity. MPRs can be directly carbonized to ordered mesoporous carbons in a cost-effective manner [1-3,11, 24].

The conventional method for making MPRs entailed the usage of self-assembled network resins such as phenol-formaldehyde (PF) resins oriented using block copolymer templates (such as P123 and F127). The orientation of phenol-formaldehyde moieties was incumbent on strong hydrogen bond interaction with the pluronic template [1-4, 11,24]. The mesoporous structure can be produced by two types of templates (1) supramolecular aggregates like surfactant micelle arrays (made from block copolymers) and (2) rigid mesoporous solids, which are performed, such as mesoporous silica and colloidal crystals [129,130]. When supramolecular micellar aggregates are used, the process is called soft-templating, while the method involving rigid mesoporous templates is known as hard

templating or nano casting. The template must be removed after the process of synthesizing the mesoporous polymer is over. The primary limitation of using a template is difficulty in removing it after pore construction. The process of template removal is complicated and adds unit operations and cost to the process of MPRs synthesis.

In addition to the template, a central role in processing is played by the interface. The interface between the template material and the actual polymer (which will orient itself around the template to form the mesoporous solid) is crucial to the assembly and construction of the mesostructure. The interaction is considered to be critical in governing the soft-template route for the synthesis of MPRs materials. The method of using these external templates has significant limitations. The final products are obtained in the form of the powder, which prevents their application as films, and specific molded shapes. There is also a limit to the sizes and patterns of mesopores obtained.

Furthermore, conventional MPRs synthesis requires the use of organic solvents with acid or base catalyst and curing at temperatures from 75 °C–260 °C to crosslink phenol-formaldehyde precursors. Although this high-temperature hydrothermal synthesis ensures complete cure and enhanced thermomechanical stability of the PF resin [4], it also entails safety and environmental concerns with the use of solvents at high temperature. MPRs networks prepared as said-from the condensation of phenolics with aldehydes. To incorporate catalytically active heteroatoms, the synthesis must either include the use of appropriate precursors or incorporate these heteroatoms post-treatment. However, these processes may partially destroy the mesoporous structure in the MPRs. This results in ill-dispersed active catalyst sites [131-135]. The primary reason is the lack of appropriate sol-gel methods for precursors. Additionally, their air and water sensitive features are

considered destructive. This calls for the development of a synthetic organic solvent-free method as well as a template-free process for the preparation of MPRs.

In the paper, we present a novel one-pot aqueous phase synthetic method for making a phenolic mesoporous resin containing well-dispersed Pd nanoparticles without the usage of a template and organic solvent. Elimination of a template reduces at least one to two-unit operations entailing template breakdown and purification of the MPRs, thus making this process conducive to scaling up. The elimination of an organic solvent also establishes a green, low-toxicity process, laying the foundation for ease of scale-up, decreaseing the production cost, and applicability. Also, the proposed synthesis method offers a novel approach for anchoring metal particles in the structure of the catalyst polymer network for the efficient cross-coupling reaction to produce fine chemicals. Pd containing MPRs (Pd-MPRs) were synthesized using polyethyleneimine (PEI) in either water or ethanol/water media and loaded with varying levels of Pd nanoparticles. The MPRs were observed to allow sufficient loading of Pd nanoparticles for effective catalytic activity due to unique interactions between the Pd ions and amino groups during material synthesis [136]. The structure-catalytic performance relationship of the developed Pd-MPRs was determined via batch Suzuki- Miyaura cross-coupling (SMC) reactions and continuous SMC reactions in a microreactor.

4.2 Materials and Methods

4.2.1 Materials. Resorcinol, 98%, formaldehyde 37%, palladium acetate and PEI 99% (molecular weight 10000 DA) were purchased from Alfa-Aesar and used without purification.

4.2.2 Synthetic procedures. MPRs and Pd-MPRs were synthesized in one step by the reaction between resorcinol, formaldehyde, and PEI in water or ethanol solution. As a typical run, 1.5 g resorcinol was dissolved in 4.4 mL of distilled water with vigorous stirring in a water bath (40 ºC) to obtain a clear solution. Then, 5.6 mL of 1.96 or 3.93 w/v% aqueous or ethanolic PEI solution was added to it and kept in the water bath for 15 minutes. Subsequently, palladium acetate powder was added and kept stirring for 20 minutes. Finally, 2.1 mL of formaldehyde (37% in water) was injected at a high, stirring speed (up to 750 rpm). After 20 minutes, the solution was poured in a Teflon hydrothermal autoclave chamber and baked for 12 hours at 120 ºC. The synthesized Pd-MPRs were washed with DI water and dried under vacuum at room temperature. The catalyst was ground and sieved for reaction efficiency consideration. A control MR was also made with 0% PEI.

4.2.3 Characterizations. The N_2 adsorption and desorption analyses was measured by using a NOVA 2200 Surface Area Analyzer (Quantachrome, US) to determine the surface areas and volume distributions of the synthesized materials. X-ray photoelectron spectra (XPS) characterizations were performed on a PHI model Quantum 2000 spectrometer with scanning ESCA multiprobe (Physical Electronics Industries Inc.) and with Al Ka radiation (l=1486.6 eV) as the radiation source. The spectra were recorded in

the fixed analyzer transmission mode with pass energies of 187.85 eV and 29.35 eV for recording survey and high-resolution spectra, respectively. The powder samples were pressed on a double-sided carbon tape mounted on an Al coupon pinned to a sample stage with a washer and screw then placed in the analysis chamber. Binding energies (BE) were measured for Pd 3d, N 1s, C 1s and O 1s. The XPS spectra obtained were analyzed and fitted using CasaXPS software (version 2.3.16). Sample charging effects were eliminated by correcting the observed spectra with the C 1s BE value of 284.8 eV. The thermogravimetric properties of the synthesized materials were measured using a TA Instruments Q500 thermogravimetric analyzer. Approximately 5 mg of sample was placed in a platinum pan and heated to 700 °C at a rate of 10 °C/min in a N_2 atmosphere (40 mL/min balance gas flow rate and 60 mL/min sample gas flow rate). Thermo Scientific™ Quanta™ line 650 scanning electron microscopes (SEM) with low vacuum detector and EDAX Electron Backscattering Diffraction, Energy Dispersive Spectroscopy were used for elemental mapping analysis and SEM. Aztech software was applied to the analysis of EDAX data. JEOL 2010 FasTEM with an ultra-high-resolution pole-piece was used for evaluating mesoporosity. The resolution was 0.14nm. It was equipped with a Gatan Imaging Filter (GIF 2000).

4.2.4 Catalytic activity. A 15 ml three-neck flask that was fitted with a reflux condenser was chosen as the reactor in all batch experiments. For Suzuki- Miyaura cross-coupling reactions, the flask was filled with a mixture of 0.25 mmol of 4-iodotoluene, 0.375 mmol of phenylboronic acid, 0.5 mmol of potassium carbonate, and 3 mL of ethanol and 1 mL water as solvents. This was followed by the addition of the catalyst (0.15 g), and the mixture was stirred at 80 °C for 45 min. Similarly, a mixture of 1 mmol 4-boromotoluene,

3.0 mmol of phenylboronic acid, and 2.0 mmol of potassium carbonate was added together and then 3 mL of dimethylformamide (DMF) and 1 mL of water were used as solvents. This reaction was performed for 5 hours at 110 °C. The microreactor that was used for continuous reactor evaluations was a U shaped plastic tube (0.22 mm OD and 0.2 ID) The tube was surrounded by a shell, fabricated using a Formlabs Form 2 SLA printer with their black resin (RS-F2-GPBK-04), with both the input and output of the temperature regulating fluid on the same side. The reaction temperature was adjusted and controlled by pumping hot water through the shell. A Harvard syringe pump was used to feed the reactor. For all experiments, the samples were analyzed with a Varian GC 3900 gas chromatograph (Agilent Technologies, Santa Clara, CA, USA), using a Factor Four VF-5ht capillary column (30 m×0.25 mm ID), provided by Agilent Technologies (California). Measurement was run by raising the temperature from 50 to 200 °C at 20 °C min^{-1}.

4.3 Results

4.3.1 Pd-MPRs synthesis. PEI is a polymer with amine-containing repeat units, spaced out by an aliphatic ethylene CH_2CH_2 linkage. PEI can be synthesized as linear, highly dendrimeric, or branched polymers [137]. The hypothesis of the formation of a porous structure using PEI involves the crosslinking of the resorcinol-formaldehyde (RF) resin using a branched dendrimeric PEI that provides a large number of primary amines participating in the crosslinking (Scheme 1). The highly branched dendrimeric form of the PEI integrates into the chemical structure and provides porosity. The primary amines participate in the crosslinking mechanism, and as a result, orient the resorcinol-formaldehyde pre-polymer along the lines of its own dendrimeric structure. The

dendrimeric structure hence controls the extent and the type of porosity obtained in the final mesoporous structure.

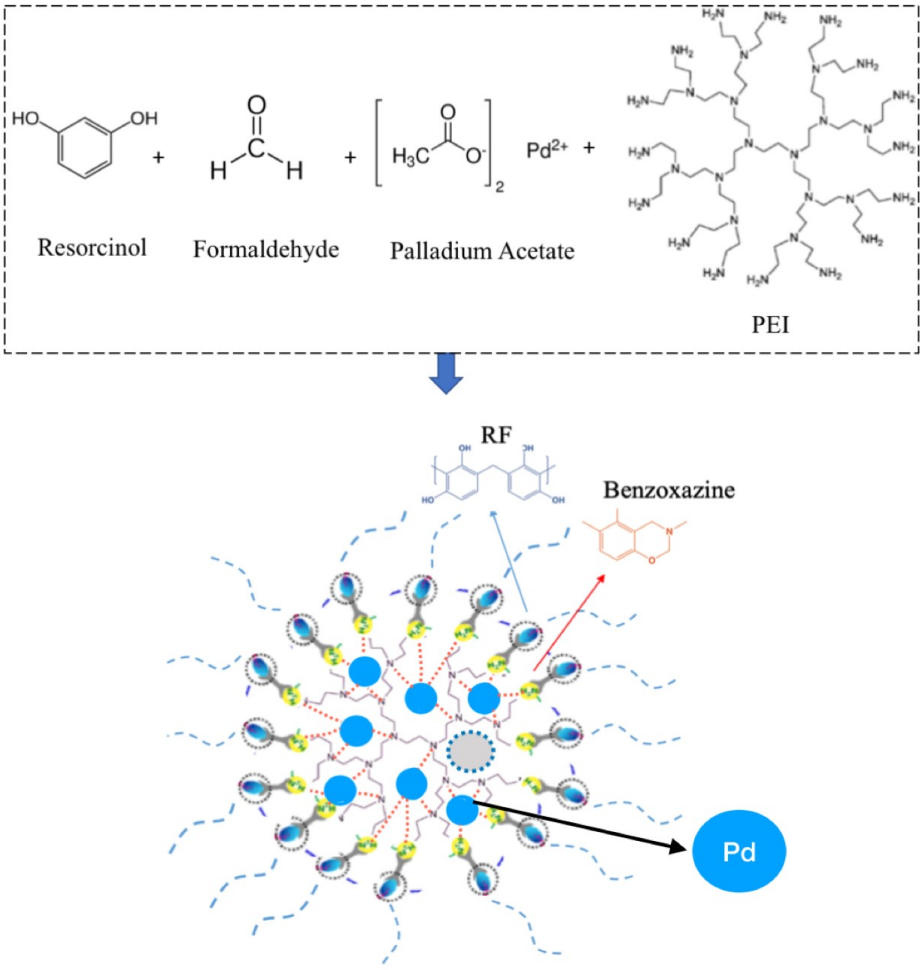

Figure 4. Scheme of aqueous phase synthesis of Pd-containing mesoporous polymeric resins, where RF represents the resorcinol-formaldehyde component of the formed crosslinked polymer network

Since hyperbranched PEIs are liquids at room temperature, the "body" of the resultant solid will be provided by the crosslinking and characteristics of the RF resin, while the involvement of the PEI will control the porosity. Thus, the polymerization of resorcinol and formaldehyde is accompanied by a reaction between amine groups in the PEI and resorcinol and formaldehyde as well as pre-polymerized linear oligomers of RF leading to the formation of benzoxazine rings in the crosslinked and porous polymer network. Since the process does not involve an external template and can be accomplished in a one-pot synthesis procedure, from a commercial processing point-of-view, major advantages include: (1) the reduced number of unit operations due to the absence of the template removal step, and (2) the ease of production and low manufacturing cost due to the elimination of wash solvents [138-139].

4.3.2 Nitrogen adsorption-desorption analysis. The Brunauer–Emmett–Teller (BET) surface area was calculated based on N_2 adsorption isotherms (Table 1). The table also includes NLDFT data. Figure 1(a) shows that the PEI concentration plays a vital role in enhancing the surface area. The resin (RF) made without PEI shows a significantly lower surface area with no porous structure. The addition of 110 mg PEI (1.96 wt%) to the reaction mixture results in a nearly 590% increase in surface area over the resin made without PEI. The relationship is not linear, as a further doubling in the amount of PEI to the reaction mixture to 220 mg (3.93 wt%) reduces the surface area by nearly 35% compared to 110 mg of PEI. The addition of PEI influences RF resin development, resulting in the formation of pores. However, too much PEI may result in "liquid" blocking of the developed pores, resulting in surface area reduction, as seen with the 220 mg PEI MPRs. Any further addition of PEI beyond the limit of crosslinking, determined by the

relative stoichiometric ratios of the components, may have merely caused the PEI to enter the pores as a "liquid" blocking the pores resulting in the aforementioned 35% reduction in surface area. A control MR with 0% PEI was also made, which had a very low (0- m^2/g) BET surface area.

Table 2

Surface Area and volume distribution of various catalysts based on BJH and NLDFT models (RF = non porous resorcinol-formaldehyde resin, 110 and 220 = 110mg and 220 mg PEI respectively; EW = ethanol-water, W=water solvent P1 and P3 = 1wt% Pd and 3wt% Pd, respectively

	Surface area (m^2/g)				Pore volume (cc/g)	
	BET (Meso)	BET (Micro)	BJH	NLDFT	BJH	NLDFT
RF	14	20	8	13	0.033	0.030
MPR110-EW	207	326	315	390	0.350	1.522
MPR220-EW	80	212	80	167	0.340	0.274
MPR110-EW-P1	108	257	109	177	0.240	0.175
MPR110-W-P1	74	149	74	114	0.850	0.493
MPR110-W-P3	129	205	129	139	0.170	0.802

Table 2 (continued)

	Surface area (m^2/g)				Pore volume (cc/g)	
	BET (Meso)	BET (Micro)	BJH	NLDFT	BJH	NLDFT
MPR110-EW-P3	226	432	226	384	0.350	0.447
MPR220-EW-P3	123	342	123	236	0.140	0.241

We also evaluated the effect of palladium concentration on the surface area of the Pd-MPRs (Figure 5b). The surface areas of MPR110-EW, MPR110-EW-P1, and MPR110-EW-P3 are 326, 257, and 433 m2/g, respectively (110 and 220 stand for 110 mg and 220 mg PEI, respectively; EW stands for ethanol-water solution, W stands for water solution; P1 and P3 stand for 1 (wt%) Pd and 3 (wt%) Pd, respectively). As seen in Figure 1b, the increase in Pd acetate content from 0 (wt%) to 3 (wt%) results in a significant increase in the surface area of MPRs containing the same concentration of PEI. The increase in surface area can be attributed to the formation of organometallic complexes between Pd and the nitrogen of the PEI, which tends to anchor and orient the PEI dendrimers as well as the RF moieties in spatially aligned networks contributing to enhanced porosity in general.

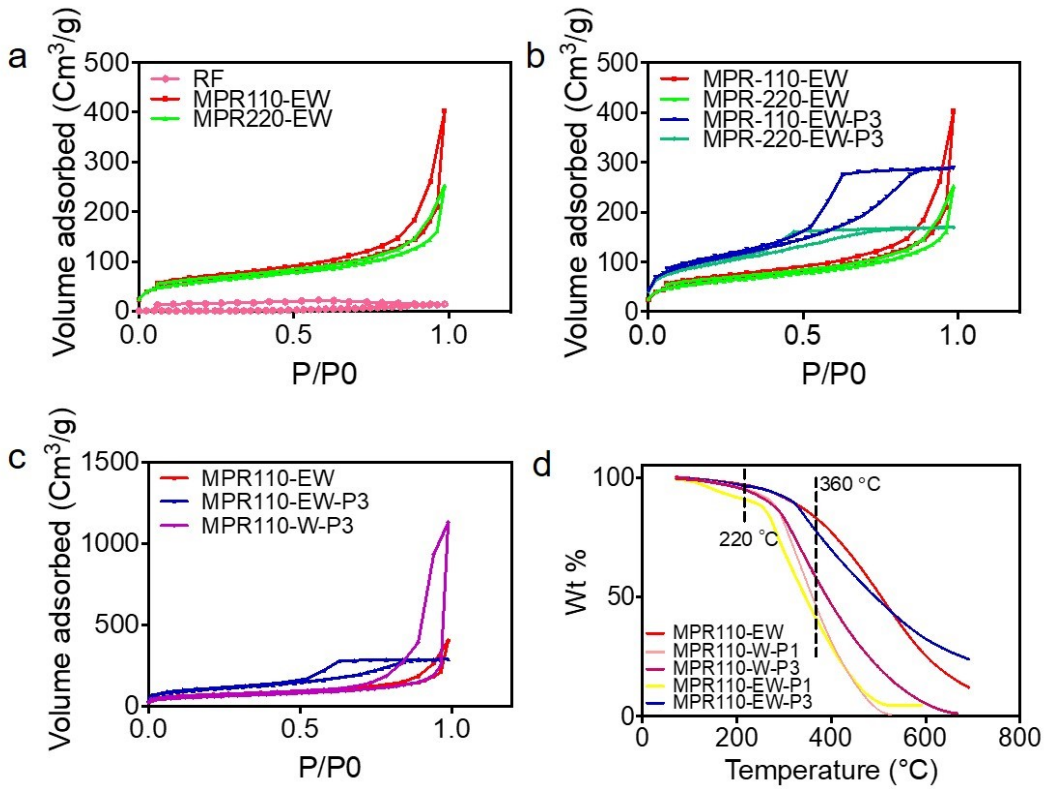

Figure 5. (a-c) N_2 adsorption−desorption isotherms of (a) MPR with varying PEI concentration, (b) Pd-MPRs with varying Pd concentrations, and (c) Pd-MPRs made either in the presence of water or water/ethanol as the solvent. (d) Thermal stability of MPR with varying PEI concentration (RF= nonporous resorcinol-formaldehyde resin; 110 and 220 = 110 mg and 220 mg PEI, respectively; EW= ethanol-water; W= water solvent; P1 and P3 = 1 and 3 wt% PD, respectively).

Figure 5c explores the effect of water versus ethanol/water as the solvent medium in the Pd-MPRs synthesis. While, in ethanol/water as a reaction medium, the addition of 3 wt% Pd acetate causes an increase in the surface area (as also seen in Figure 5a), the use of water as the reaction medium causes a slight decrease in the surface area in a comparable reaction set-up. The explanation could be tied to the solubility of Pd acetate. Pd acetate is soluble in organic solvents. However, it has low solubility in water. Therefore, Pd

distributed poorly at centers. As a result, orienting the nitrogen atoms of the PEI and RF moieties was incapable, through coordinate bonding, or clustering of Pd acetate, in the porous structure. Consequently, it leads to a lower surface area when compared to that obtained when using ethanol as the solvent. Despite this, making the porous catalyst in the water phase make the catalyst synthesis more environmenttal friendly with a less downstream process to reuse the solvent phase.

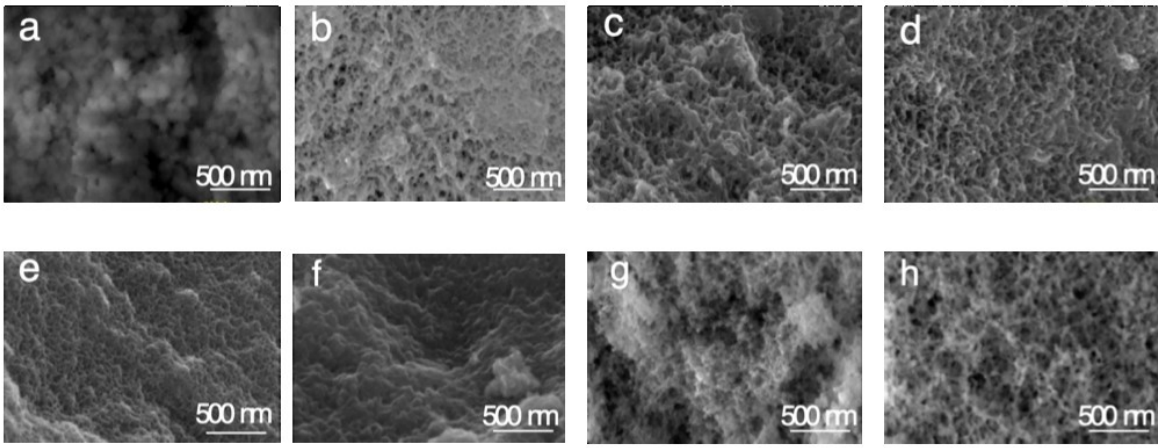

Figure 6. SEM of various samples: (a) RF (b) MPR110-EW, (c) MPR220-EW (d) MPR110-EW-P1 (e) MPR110-EW-P3 (f) MPR110-W-P1 (g) MPR110-W-P3 and (h) MPR220-EW-P3. (100000X)

4.3.3 Thermogravimetric analysis (TGA). Figure 7 illustrates the comparative thermal stabilities of the synthesized MPRs. In general, the MPR showed high thermal stability up to the temperatures of 320 to 360 ºC. The addition of 1 (wt%) Pd causes a steeper weight loss starting at around 220 ºC versus the weight loss commencement. With an increase in the Pd loading to 3%, the sharpness of the weight loss is also less. The weight

loss seems the least sharp with the usage of 3% Pd. From Figure 5d it can be inferred that the mesoporous resin held onto a significant amount of water, due to the usage of PEI, which induced hydrophilicity due to the presence of amine groups. The heating kick-starts water evaporation and hence the apparent weight loss at an earlier temperature. The reaction mixture in ethanol may have lost its solvent from its porous interstices due to the lower affinity of ethanol for the amino groups in PEI as well as ethanol's higher intrinsic volatility.

4.3.4 Scanning electron microscopy (SEM). Figure 6 shows the SEM images of the mesoporous catalyst with various compositions. Compositions made with palladium acetate and ethanolic PEI solution exhibit a uniform morphology with an interconnected framework and visible uniform micropores. These SEM images confirm the average pore size of the various catalyst, and they are listed in Table 2. The morphology of the resin compositions made without PEI is found to be spherical (Figure 6a). The addition of ethanolic PEI solutions was observed to increase pore interconnectivity. With the immobilization of Pd to these compositions, a further increase in pore interconnection was observed with a concomitant increase in the surface area, as mentioned above. However using water instead of ethanol, as the medium, to synthesize the same compositions with immobilized Pd, showed a non-uniform pore interconnection. These changes may be correlated to the results obtained with the BET isotherms in Figure 5. That is attributable to the formation of coordination complexes between Pd and the donor nitrogen atoms of PEI and the RF (including the benzocaine ring) anchoring. As a result, orienting the dendrimers rendered in the structured by the spatial alignment of polymer networks and

interconnected porous network design. Again, the poor solubility of Pd acetate in water and concomitant phase separation, renders Pd atoms incapable of uniform coordination with N atoms of PEI and benzoxazine groups, resulting in a poor spreading and inferior spatially connected network formation. Also, a competition between the oxygens of water and N atoms of the PEI for anchoring the Pd atoms may result in the randomness of the network shape.

4.3.5 TEM and XPS and elemental analysis. The transmission electron microscopy (TEM) image of MPR110-EW-P1, supported the existence of uniform mesopores inside the network (Figure 7a). Figure 7b-d shows the XPS spectra of MPR110-EW-P3, which show peaks associated with C 1s, N 1s, and Pd 3d. The deconvolution and fitting of the C 1s spectra yielded three peaks at around 284.8, 286.2, and 288 eV. These were attributed to C-C bonds of the aromatic benzene ring, C-N, and O-C=O bonds. The N1s peaks at around 387 and 405.5 eV belonged to amino group nitrogen and those associated with Pd through coordination. The peaks of Pd 3d at ~336.56 and 341.8 eV were those of Pd0. The peaks at ~338.6 and 343.2 eV were assigned to Pd^{2+}. Pd was hence concluded to have been incorporated successfully within the MPR compositions in various valence states. The coordination bonding with the Ns of the various amino groups and the nitrogen of the benzoxazine groups in the sample could be the reason for strong bonding. Figure 7 e and Figure 7f and Table 4 present the EDX elemental analysis for MPR110-EW-P3 catalyst. The results confirm a relatively high amount of nitrogen atoms (7-11 %w/w) in the catalyst structure which is related to the amine groups in the PEI structure.

The high content of nitrogen atom is a good indication for strong interaction of Pd and amine group in the sample as observed in XPS data.

Table 3

Carbon, Oxygen, Nitrogen, and Palladium in various Pd-MRs catalyst based on EDS

Sample	Carbon	Oxygen	Nitrogen	Palladium
MR110-EW	50.14	41.55	8.31	0
MR110-EW-P1	53.32	37.62	7.25	1.55
MR110-W-P1	51.87	35.42	11.08	1.63
MR110-W-P3	52.67	10.34	36.75	0.25
MR110-EW-P3	55.58	36.96	7.31	0.16
MR220-EW-P3	54.67	37.12	7.42	0.79

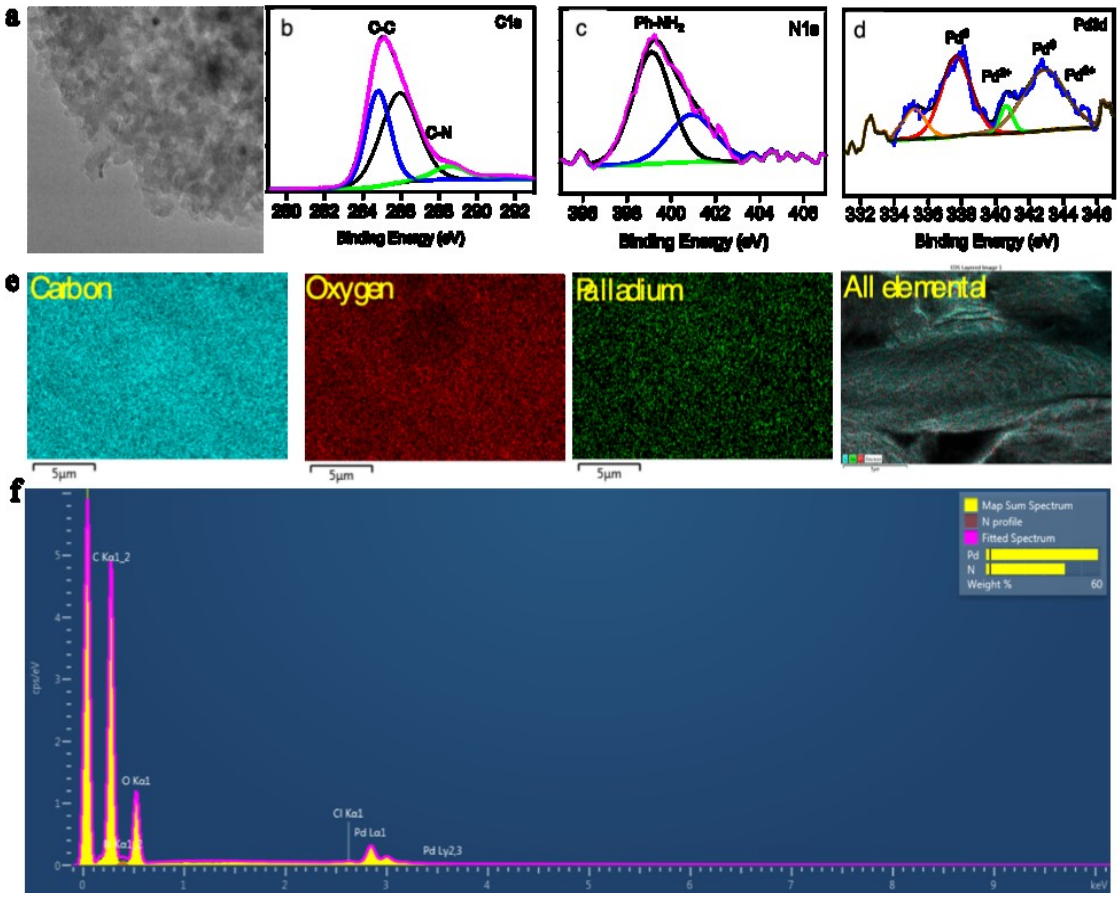

Figure 7. (a) TEM, (b) XPS spectra of C 1s, (c) XPS spectra of N 1s, (d) XPS spectra P 3d, (e) EDS elemental map and (f) elemental graph of MPR110-EW-P3.

4.3.6 Catalytic application. The catalytic efficiencies of the mesoporous catalysts, made with various compositions and under different reaction conditions, were tested in typical Suzuki-Miyaura reaction batches. The C-C bond of 4-iodotoluene was reacted with aryl boronic acid under mild conditions comprising the ethanol-water reaction medium and potassium carbonate as the base. Figures 8 a and d show the schematic and Suzuki-Miyaura reactions in a batch system using Pd-MPRs as catalysts for iodotoluene (using ethanol as

solvent) and bromotoluene (using DMF as solvent). The conversion versus time is shown for the respective reactions in Figures 8 b and c. The conversion climbs up faster and more abruptly, reaching a higher final value for the iodotoluene reaction. The primary difference between the two reactions could be attributed on one hand to the intrinsically more “labile” carbon-iodine bond in the iodotoluene, and on the other hand to the presence of different solvent systems in the two cases. The DMF solvent system is also expected to cause some amount of catalyst poisoning which reduces the rate of the reaction as well as the overall conversion. The catalyst MPR110-EW-P3 with the highest surface area (433 m^2/g) showed the maximum conversion rate of 98.98%. A control MR with 0% PEI was made and tasted. In addition to a very low (0-2 m^2/g) BET surface area, we obtained only 6.8% conversion.

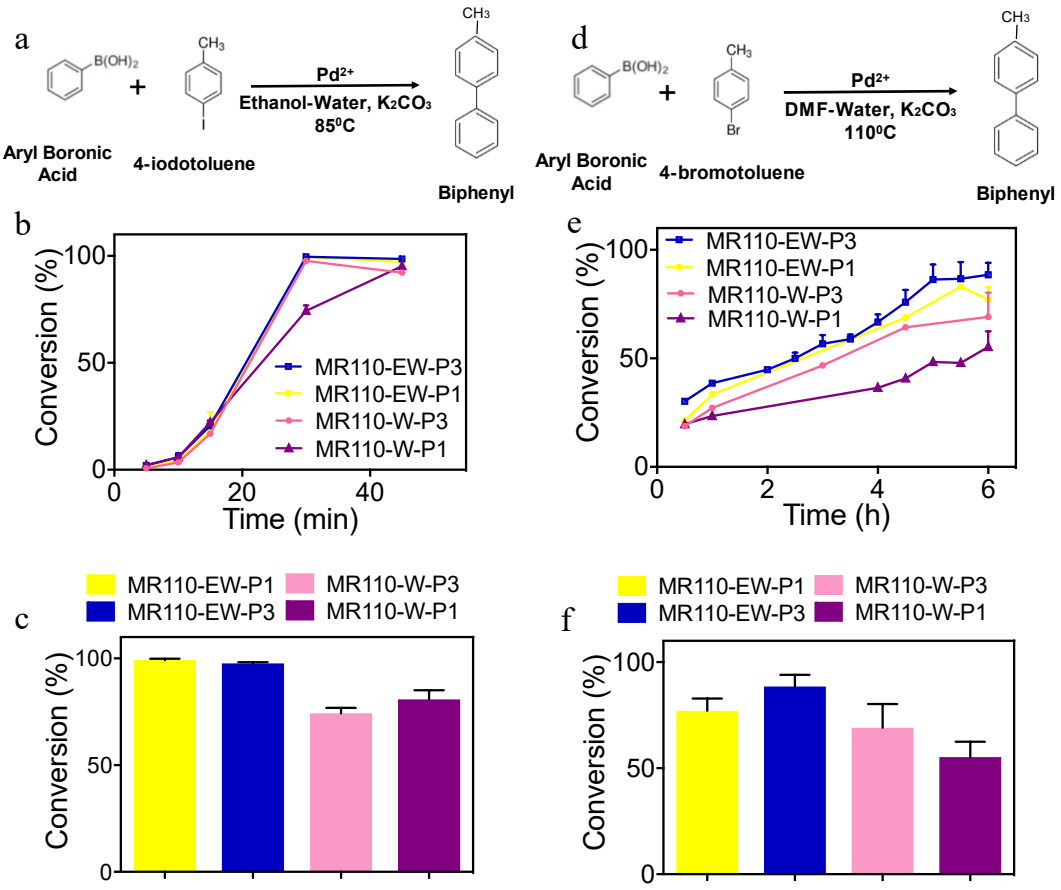

Figure 8. Suzuki- Miyaura reaction in batch system (a) Reaction schematic, (b) Time effect on conversion rate for Iodotoluene and ethanol as solvent, (c) Catalyst type effect on conversion rate for Iodotoluene and aryl boronic acid in the present of ethanol as solvent, (c) Reusing effect on conversion rate for Iodotoluene and ethanol as solvent (n=3) (d) Reaction schematic, (e) Time effect on conversion rate for Boromotoluene and DMF as solvent (f) Catalyst type effect on conversion rate for Boromotoluene and aryl boronic acid in the present of DMF as solvent (n=3).

In general, the results showed the catalytic efficiency of the Pd-MPRs depends on the type of PEI solution used to make the mesoporous catalyst and the percentage of palladium immobilization in the catalyst structure. The catalysts made using PEI in ethanol/water, and those with a higher amount of Pd immobilization have superior catalytic activity. The amount of active Pd sites is directly related to the center of coordinated

catalytic sites available for the reaction. The usage of water rather than ethanol/water in mesoporous catalyst synthesis has a direct bearing on the surface area and the porosity obtained with the catalyst, which, in turn, affects the diffusivity of reactants onto the active sites and hence the ensuing results. Additionally, we surmise that the lower solubility of Pd salts in water may have led to a non-uniform distribution of Pd anchoring centers in the catalyst structure. This would lead to clustering and poor extent of coordination with the PEI dendrimers and benzoxazine groups which automatically decreases the easy and uniform availability of active catalytic centers, hence corroborating the results.

The same Suzuki-Miyaura coupling of the C-C bond of 4-bromotoluene (Figure 8 d, e, and f) with aryl boronic acid in the presence of DMF-water and potassium carbonate at 110 ºC was also undertaken.

The reaction conversion rate for various catalysts is shown in Figure 8 e. The results show that MPR110-EW-P3 has a maximum conversion rate of 88.5% after 5 hr. After 5 hr, the conversion rate stagnates due to the saturation of the catalyst surface by the aromatic compound. The conversion rates of MPR110-EW-P1, MPR110-W-P3, and MPR110-W-P1 are 77%, 55.2%, and 65%, respectively. After 5hr, underscoring that while an increase in Pd content enhances the catalytic capacity. The effect that water has on clogging pores and reducing surface area is more detrimental to make up for the increase in catalytic activity. These results showed that surface area and the solvent used to dissolve PEI for making the catalyst played essential roles in catalyst efficiency.

We studied the recyclability of MPR110-EW-P3 in the model SMC reaction. Figure 9a shows the Suzuki- Miyaura reaction conversion rate in a batch system for iodotoluene after 5 cycles (n=3). Figure 9b shows the SEM and the corresponding EDX elemental

mapping analysis for used MPR110-EW-P3 after 5 runs. After each reaction cycle, the catalyst was separated by filtration and then washed thoroughly with copious amounts of cold water-ethanol solution, and the recovered catalyst was dried under vacuum at 40 ºC for 2 hr. Thus purified, the catalyst was re-employed in five successive cycles under equivalent conditions. As shown in Figure 9 b, the percentage of conversion rate was almost the same for all these runs (up to 98.9%).

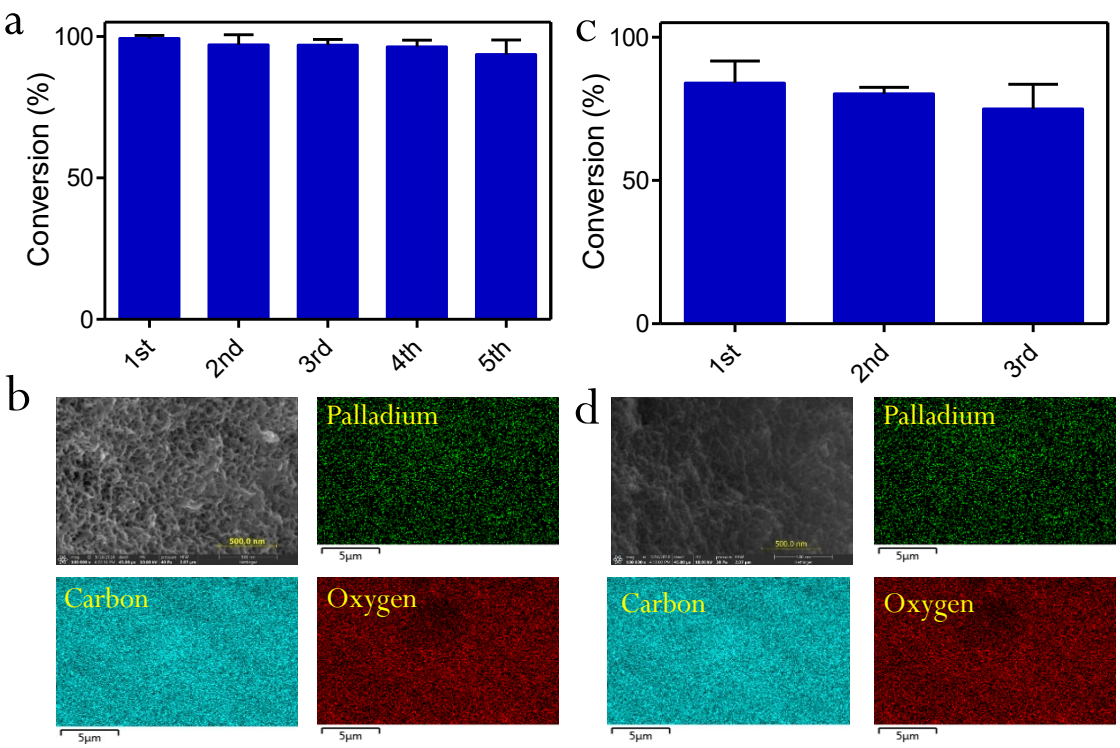

Figure 9. (a) Suzuki- Miyaura reaction conversion rate in batch system for Iodotoluene with ethanol as solvent for 5 reaction cycles (n=3), (b) SEM, and the corresponding EDS elemental mapping analysis for used MPR110-EW-P3 3% after 5 runs in ethanol-water as solvent (c) Suzuki- Miyaura reaction conversion rate in batch system for Bromotoluene and DMF as solvent for 3 cycles (n=3) , (d) SEM, and the corresponding EDS elemental mapping analysis for used MPR110-EW-P3 after 3 cycles with DMF- water solvent.

Recyclability of MPR110-EW-P3 in Suzuki-Miyaura reaction conversion rate for bromotoluene in DMF as a solvent for 3 cycles (n=3) is shown in Figure 9 c.

After each run, the catalyst was separated by filtration and then washed with copious amounts of cold DMF followed by water. The catalyst was dried under vacuum at 40 ºC overnight and then reused for the next run. The activity reduced from 86.3±3% in the first run to 80.5±2% and 80.3±4% in the second and third run, respectively. Based on the above results, and as per previous literature reports, catalyst activity decreases because of leaching palladium and shrinkage of the structure. Surface area declined for this catalyst in DMF solution more than five times. The DMF water medium for the second group of SMC reactions has a detrimental effect with progressive runs on the breakdown of the structure of the catalyst as well as rapid clogging of pores resulting in the reduction of surface area with the ensuing decrease in catalytic efficiency.

4.3.7 Continuous Suzuki- Miyaura reaction in a microreactor. A fixed bed microreactor was employed to establish the efficiency of the heterogeneous Pd-MPRs catalyst in a continuous flow set-up. A schematic of the microreactor set-up and results of the continuous reaction are shown in Figure 10 a. C-C bond coupling between 4-iodotoluene and aryl boronic acid, as the SMC reaction model. The U shape micro tube provides enough length of catalyst for proper Pd-MPRs residence time, as Glass beads shown in Figure 10. Various process parameters, such as the inlet flow rate and temperature, were considered and varied for studying the system. The conversion rate during the reaction time confirmed that the continuous process is almost steady-state, and catalyst efficiency remains at a steady and stable value for up to 20 min for minimum and maximum flow rate (0.1 and 0.5 µl/min (Figure 10 b). Additionally, Figure 10 c shows the

effect of temperature on the conversion rate for 4-Iodotoluene and ethanol as solvent at an initial velocity of 0.1 µl/min. Figure 10 d shows the effect of velocity on the conversion rate for 4-Iodotoluene and ethanol as a solvent at 85 ºC. On increasing the temperature from 65 to 86 ºC, the conversion rate was enhanced from 51.6 to 60.7% at the initial flow rate of 0.5 (µl/min). Increasing the flow rate can increase the conversion rate by enhancing the mass transport coefficient. On the contrary, this resulted in decreased residence time inside the reactor [138]. Therefore, it is not possible to observe a linear relationship between flow rate and conversion. The maximum conversion rate was reported for 0.2 µL/s (61.6%), and after that, it decreased to 46.4% at a flow rate of 0.4 µL/s. This translates to a space velocity of 0.1 and 0.5 h-1, respectively.

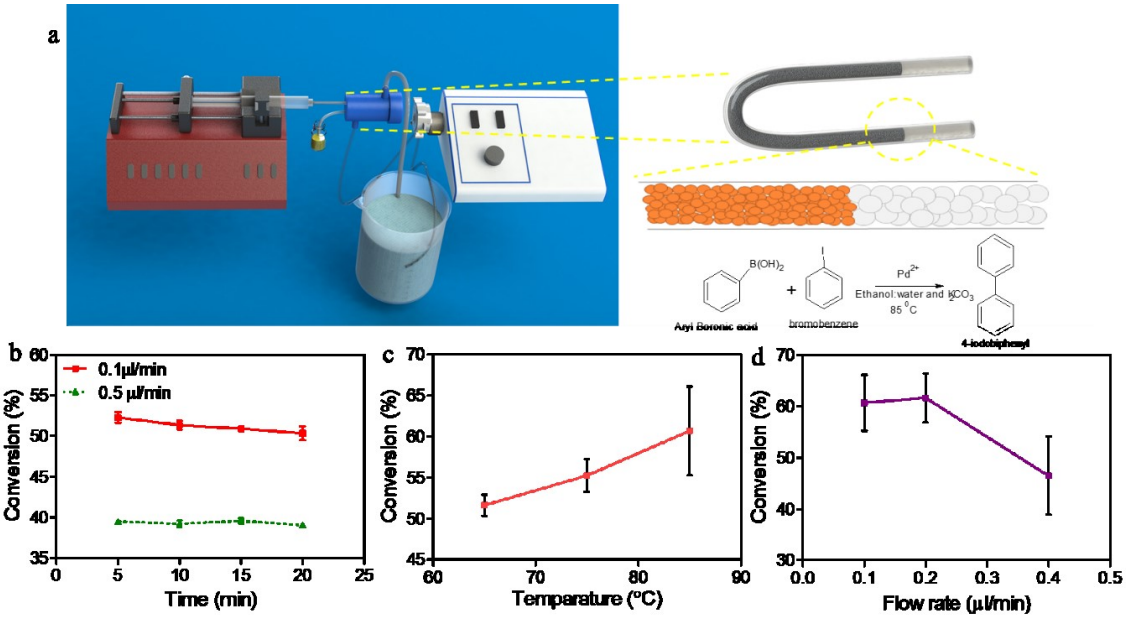

Figure 10. Suzuki-Miyaura reaction in microreactor (a) Microreactor set-up (b) Velocity effect on conversion rate for 4-Iodo toluene and ethanol as solvent at 65 ºC during time (c) Temperature effect on conversion rate for 4-Iodo toluene and ethanol as solvent at initial velocity of 0.1 µl/min (d) Velocity effect on conversion rate for 4-Iodo toluene and ethanol as solvent at 85 ºC (n=3).

4.4 Discussion

While mesoporous molecular silica or alumina sieves have been widely studied for anchoring Pd species, their hydrothermal instability limits high-temperature catalytic applications [133]. Thus, anchoring of Pd to the mesoporous catalyst structure has been tried by employing alternate functional groups, such as metal-organic frameworks [134], magnetic supports [136], carbons [139], and polymers [140-141]. The use of a functional framework, one end of which is tethered to the main mesoporous catalyst structure while the other end is likely managing to hold the Pd(II) moiety. This is expected to provide for a superior and a more uniform distribution of active metal centers. The only limitation that may occur with this method is the control of reactivity by the anchoring functional group, which may reduce the catalytic activity of the Pd center towards the intended reaction [134]. The amine group has been widely studied by way of (3-aminopropyl) triethoxysilane (APTES) [141-142], which is a good electron donor (NHC donor) and Pd anchoring group for coupling catalysis. N- heterocyclic groups have also been similarly used to anchor Pd with the concomitant formation of NHC donor-Pd catalysts for coupling reactions [142-143]. In this light, we may be able to visualize the anchoring of Pd in our work as schematically shown in Scheme 1 [134]. The Pd may be expected to be dispersed and held in place by the tertiary nitrogens from the PEI branched structure, as well as, to a lesser extent, from the N in the benzoxazine ring, due to the -I effect of the oxygen atom to the N in the benzoxazine.

Scheme 1 depicts the positions and anchoring of Pd centers in the PEI-RF network. As mentioned earlier, the lone pair of electrons on the tertiary nitrogen of the PEI as well as those in the benzoxazine group engage with the Pd (II) center, and one nitrogen atom

may coordinate once with a Pd center given the presence of only one lone pair of electrons per N atom. Pd (II) is known to form mostly four coordinated square planar complexes. Thus, the Pd is expected to anchor and form a complex where the structure of the RF-PEI infinite network provides four N centers in a square planar formation. In the absence of sufficient donor groups surrounding the Pd center in a square planar formation, not every "cavity" formation offered by the mesoporous network may successfully anchor and hold onto a Pd center, even if stoichiometric equivalence may allow so, and this is shown in Scheme 1 showing an empty "cavity". Pd (II) has an electronic configuration containing eight electrons in the 4d orbitals. The remnant available dz^2 may hybridize with the 5s and two 5p orbitals to form four dsp^2 hybridized orbitals oriented in a plane for accepting electron donors, such as the lone pair of the p orbitals of the N atoms. Thus, the anchoring of Pd(II) species may be limited by the presence of four neighboring N atoms in a square planar formation. From Scheme 1 there may be a paucity of N donors towards the periphery of the "globe" shown, and the coordinating N atoms predominantly arise from the benzoxazine group. However, the PEI-RF network is an "infinite" three-dimensional network, and only a visualizable symmetric section is shown in Scheme 1. Thus, the origin of the N donor atom-PEI versus benzoxazine is dependent on the relative stoichiometry of PEI: RF used in the reaction.

The cross-coupling in the Suzuki-Miyaura Pd catalyzed coupling goes through oxidative addition, followed by transmetallation and reductive elimination [134]. The rate constant of Suzuki couplings is known to be dependent on the Pd - donor ligand binding energy [144]. There may be a subtle difference in the donor ability of the nitrogen centers in the PEI versus that in the benzoxazine. Both the nitrogens are in the proximity of electron

withdrawing electronegative atoms. In the benzoxazine group, the N is separated from oxygen by one CH_2 link, while in PEI, the N is separated from another N by a CH_2-CH_2 link. The benzoxazine N, due to closer proximity to a more powerful electron withdrawing entity (oxygen), is expected to render itself as a weaker donor to the hybridized dsp^2 orbitals of Pd(II), making it more available as a base for the coupling. However, there may be an offset on the benzoxazine nitrogen's fundamental ability as a Lewis base due to its intrinsic proximity to oxygen trying to polarize the electron cloud towards the latter via a secondary -I effect. The stoichiometric ratio of benzoxazine nitrogen and PEI nitrogen may provide for an interesting future study on the kinetics of Suzuki couplings.

Additionally, the activity studies on immobilized Pd catalysts versus that in the form of homogenous complexes underscore the fact that Pd (II) acts as a catalyst in the heterogeneous rather than the homogenous form [145]. Thus, the development of a scalable, easy to manufacture catalyst structure, which may be retrofitted in versatile manners from the industrial plug flow bed type reactor designs to simple micro designs for biomedical applications, underscores the importance of this catalyst design method for Suzuki-Miyaura couplings under mild conditions with versatile reactions for wide application vistas.

In fact, PEI, a dendrimeric polymer, was used to develop a novel template free, simple, one-pot process for making an MPR structure. The mesoporous, template-free resorcinol-formaldehyde resin was used to immobilize palladium acetate, with resultant high surface area and interconnected porosity and distribution of Pd species guided by coordination complexes with the N centers. The Pd-MPRs catalyst exhibits excellent catalytic activity, applicability, and durability for the SMC reaction under varying

conditions - mild and harsh with ethanol/water and DMF/water mediums, respectively. The Pd-MPRs catalyst can efficiently catalyze SMC reactions with conversions reaching between 95-98% within 45 min to 5 hr, depending upon the exact conditions. The large surface area of the catalyst and high uniform distribution of Pd leads to excellent catalytic performance. The catalyst also shows excellent recyclability with minimal reduction in final conversions with repeated cycles.

Furthermore, proper thermal stability and low Pd leaching underscore the potential of this catalyst as an excellent candidate for drug synthesis applications. Further investigations into the stoichiometric ratio of catalyst components, their effect on the catalytic structure, and thereof on the SMC and catalytic mechanism would provide an interesting scientific platform for future study on the kinetics of Suzuki couplings. The catalysts were also tried in a micro-continuous PFR set-up, under various process and flow conditions, realizing nearly a 62% conversion. This general protocol platform may open new opportunities for the development of the catalyst for wide application vistas, for pharmaceuticals and therapeutics.

Chapter 5

Developing Eco-Friendly and Cost-Effective Porous Adsorbent for Carbon Dioxide Capture

To address global warming and climate change issues, recent research efforts have highlighted opportunities for capturing and electrochemically converting carbon dioxide (CO_2). Despite metal-doped polymers receiving widespread attention in this respect, the structures hitherto reported a lack of the ability to be easily synthesized with scale-up feasibility. In this study, a series of mesoporous metal-doped polymers (MRFs) with tunable metal functionality and hierarchical porosity were successfully synthesized using a one-step copolymerization of resorcinol and formaldehyde with Polyethyleneimine (PEI) under solvothermal conditions. The effect of PEI and metal doping concentrations were observed on physical properties and adsorption. The results confirmed the role of PEI on mesoporosity of the polymer networks and high surface area in addition to enhanced CO_2 capture capacity. The resulting Cobalt doped material shows excellent thermal stability and promising CO_2 capture performance, with equilibrium adsorption of 2.3 mmol CO_2 /g at 0 °C and 1 bar for at a surface area 675.62 m^2/g. This mesoporous polymer, with its ease of synthesis, is a promising candidate for promising for CO_2 capture and subsequent electrochemical conversion.

5.1 Introduction

With a significant rise in the average atmospheric CO_2 concentration from levels in the preindustrial age, the deleterious effects on global warming and climate change are visible [145-148]. Consequently, environmental concerns have convinced international

bodies and governments to take steps to address policies pertaining to CO_2 emissions. One of the most remarkable strategies includes CO_2 capturing and conversion technologies. Many methods have been suggested for CO_2 conversions such as chemical, photocatalytic [149-150], and electrocatalytic reduction [151-153]. In many of these technologies, heterogeneous catalysts are used as solid adsorbent and subsequent conversion, and they include materials such as silica [154-156], metal-organic frame (MOFs) [147], and carbon-based materials [155-158]. Some commonly, researched carbon-based adsorbent materials include activated carbon [159], ordered mesoporous polymer/carbon (OMP/OMC) [155, 160-161], activated carbon fibers [162- 163], carbon graphene[146, 158], and graphene oxide[164- 166]. Regular pore structure, high surface area, and inexpensive produce precursor afford potential advantageous OMP/OMC for CO_2 capture [155, 160- 161]. However, the main limitation lies in producing cost-effective catalystic structure with feasibility of process scale-up using an eco-friendly catalyst that can afford high capture capacity with the ability to convert CO_2 sustainably [145, 167- 168]. In order to increase adsorption capacity and activity of adsorbents, functionalizing the surface and pore lining has been recommended [155, 161, 169]. Basic nitrogen functional groups generally provide sites for enhanced interactions with acidic CO_2. Thus, nitrogen doping via functionalization with basic nitrogen containing groups is considered the most attractive methods to capture CO_2 [163, 167, 170]. Fujian et al. showed nitrogen not only increased CO_2 capture but also made anchoring a metal element to polymer network feasible for expediting CO_2 conversion. They synthesized ordered mesoporous phenol-formaldehydee polymer by using hexamethylenetetramine (HMTA) as a source of nitrogen. These structures exhibited high stability, CO_2 capture capacity, and selectivity [161].

Polyethylenimine (PEI) is a multipurpose polymer with amine-containing repeat units, spaced out by the aliphatic ethylene CH_2CH_2 ligand [171]. Due to its high basicity, high amine content, good thermal stability, and low volatility, it can be used to produce highly effective and stable functionalized adsorbents [172- 173]. Silica [174-175], nanocarbon tube, ordered mesoporous carbon, polymer [172, 176], and alumina [177] have been studied with PEI modifications. PEI functionalized Polymethyl methacrylate (PMMA), and polystyrene (PS)[176] showed high CO_2 adsorption capacity. Even though these structures have shown high CO_2 capture capacities, their commercial application has not yet been realized. The main hindrances for their commercial application are complicity and multi-stages synthesis methods, which not only increases the cost of adsorbent but also puts significant limitations on the scalability [172, 178]. To overcome this, Wang et al. has developed organic amine- mediated synthesis of polymers for CO_2 capturing and energy storage [179].

Solid metal-doped polymers are considered effective and environment-friendly catalyst for carbon dioxide conversion. Their advantageous features include high surface area, thermal stability, and good activity [146]. MOFs have also been reported as good adsorbents and catalysts owing to the active metal sites [147]. Cobalt, zinc, and nickel have been extensively used for this purpose. In addition to enhanced CO_2 capture, these metals also facilitate photo or chemical-electro conversion. The solvothermal method is a common method for metal impregnation into heterogeneous structures which these compounds use to modify organic frame for improving capture and entrapment of CO_2 and its subsequent conversion [146- 147]. The elimination of multistep catalyst synthesis can pave way to realizable scale-up and hence commercial application.

This paper focuses on the potential of nitrogen-doped mesoporous polymer (MRF), made using PEI, with or without a metal center, for CO_2 capturing for a possibility of subsequent electrochemical conversion. In this paper, we studied cobalt and nickel doped MR. The effect of metal and PEI concentration on MRF properties such as surface area, pore size, pore structures and morphology, thermal stability were studied. For the synthetic procedure we used resorcinol and formaldehyde as precursor. Contrary to multi-stage synthesis, the one-pot solvothermal method not only decreases the cost of production by practically eliminating the use of high solvent volumes, it also eliminates scalp- up barriers. In addition, low temperature of synthesis without the calcination stage makes it more ecofriendly. It also exhibits superior surface area and a uniform mesoporous structure, as observed from scanning electron microscopy. The elemental analysis map confirmed homogenous metal distribution. This approach also provides the opportunity for producing multi metal centered catalyst structures.

5. 2 Experimental

5.2.1 Material. Resorcinol (99%), Formaldehyde solution (37% in water), and branched polyethylenimine (MW=10000) were purchased from Alfa Aesar and used without any further processing. Cobalt acetylacetonate and nickel acetylacetonate (95%) were obtained from Bean Town Chemicals and used as received. Ethanol proof 200 (VWR) and sodium hydrogen sulfate were purchased from Sigma-Aldrich.

5.2.2 Synthesis of My-x-RFs. My-x-RFs were synthesized by a one-pot solvothermal method. 1.5 g resorcinol was dissolved in 4.4 mL of deionized water (DI). Then 5.6 mL of PEI (1.96% or 3.98%) w/v in ethanol was added, and the mixture was kept stirring at 40 °C for 20 min. Then the metal salt was added and stirred for an additional 20

min at 40 °C. Then 2.1 ml of formaldehyde solution 37% was injected by syringe quickly, and the milky solution stirred at high speed for 20 min at 40 °C. Finally, this emulsion was transferred to a Teflon autoclave chamber and kept under the static condition at 120 °C for 12h. After cooling to room temperature, the polymer was smashed and washed three times with water and then three times by ethanol. M-RFs were dried at room temperature overnight. The obtained mesoporous catalyst was named as My-x-RFs, where M is metal type, y is the metal concentration in the reaction mixture, and x is the PEI concentration denoted as N (0% PEI), M (1.96% PEI) and H (3.98% PEI). RF is denoted for mesoporous resorcinol formaldehyde polymer without metal salt and PEI.

5.2.3 Characterization. Scanning electron microscope (SEM) was used to look at the morphology and pore structure of the samples. Thermo Scientific™ FEI Quanta™ line 650 SEM (Waltham, MA, USA) with a low vacuum detector under 10 kV took images. Then energy-Dispersive Spectroscopy (EDS) was used for elemental mapping analysis by FEI Quanta FEG 250 detector. Aztec software (Oxford Instruments, Abdington, UK) was applied to the analysis of EDS data. Thermogravimetric analyzer (TG) was performed on TA Instruments Q500 with 10 °C·min^{-1} to 750 °C under N_2 with 100 m^2/hr. To remove moisture from the samples, temperature was increased to 100 °C, and data acquisition was started after cooling down to 50 °C. The N_2 adsorption was measured by Quantachrome NOVA Tech LX4. Prior the measurement, the sample was degassed at 120 °C for 24 h under vacuum to remove the adsorbed species on the surface of sample and finally cooled to room temperature. The Brunauer-Emmett-Teller (BET) method was utilized to calculate the specific mesoporous surface area of the samples by using the adsorption branch acquired at a relative pressure (P/P_0) range of 0.05–0.30 (Eq. 1). Barrett, Joyner, and

Halenda (BJH) model was applied to estimate pore size volume from the quantity of N_2 adsorbed at a relative pressure (P/P_o) of 0.99. Touch Win^{TM} software was used for all calculations, which was reported in Table 1.

$$\frac{1}{W\left(\left(\frac{P_0}{p}\right)-1\right)} = \left(\frac{1}{W_m C}\right) + \frac{C-1}{(W_m C)}\left(\frac{P}{P_0}\right) \quad (1)$$

Where W is the weight of gas adsorbed at a relative pressure, P/P_0, W_m is the weight of adsorbate constituting a monolayer of surface coverage, and C "Constant," is related to the energy of adsorption in the first adsorbed layer. Consequently, its value is an indication of the magnitude or strength of the adsorbent/ adsorbate interactions.

Molecular speciation of the samples was explored by Fourier transform infrared spectroscopy (FT-IR). IR spectra were recorded on a PerkinElmer Spectrum 100 FT-IR spectrometer.

5.2.4 Carbon dioxide adsorption. CO_2 adsorption was measured by the same system (Quantachrome NOVA Tech LX4) up to 1 bar, but an ice bath was used for 0 °C and a water bath for room temperature experiments. The samples were degassed, as mentioned above. The isosteric heat of adsorption (Qst) was calculated based on the Clausius-Clapeyron equation [65] for which the CO_2 adsorption was conducted at two different temperatures of 273 and 298 K by Eq. (2).

$$\mathrm{Qst} = \mathrm{RT}^2\left(\frac{\partial \mathrm{Ln\ p}}{\mathrm{Ln\ T}}\right) \quad (2)$$

Where R is universal gas constant, T_2 and T_1 are two different temperatures based on Kelvin, P_2 and P_1 are the partial pressure at the same amount of adsorbed CO_2 for T_2 and T_1.

5.2.5 Electrochemical conversion of carbon dioxide. An electrochemical setup for electrochemical conversion measurement was shown in Figure 12. The system includes a working electrode made of glassy carbon, a reference electrode made of Ag/AgCl electrode, a counter electrode made of platinum, and gas-flowing ports. According to convention, the working and reference electrodes were configured in a working compartment filled with 0.1 M $NaHSO_4$ aqueous solution, and the reference electrode was placed in the reference compartment filled with 3 M KCl aqueous solution. The two compartments related to the liquid bridge junction which was filled with agarose 5%, which is dissolved in saturated KCl. To prepare a working electrode, 80 mg of MRFs was grounded and mixed with 20 µl poly(vinylidene-fluoride) (PVDF, 10% w/v in N-methyl-2-pyrrolidone (NMP)), glassy carbon 3mm was covered by this paste and dried at 50 °C for 30 min.

Before every measurement, the working compartment was purged by Argon gas for 15 min, and CO_2 or Argon was flown at for 15 min based on an experiment. A voltage was swept from 0 to -2 V at 50 mV/sec between the working and reference electrode by a potentiated, which was followed by the reverse sweep from -2 V to 0 V at the same rate.

5.3. Results and Discussion

5.3.1. Chemical structure and thermal stability. Elemental analysis results on various compositions is presented in Table 5. EDS elemental analysis of these compositions is illustrated in Supplementary Figures S1 and S2. Elemental mapping results, in addition the results in Table 4, confirm that an increase in PEI concentration corresponded to an increase nitrogen content. The Figures S1 and S2 underscore uniformity of distribution of cobalt and nickel in the test sample. PEI plays an important role in

developing a uniform mesoporous structure. In fact, nitrogen, indicative of the presence of the amine group of the branched PEI structure, helps to increase nano porosity by tethering to the Co or Ni nucleation centers on one hand while participating in the crosslinking kinetics on the other. While the nitrogen content in H-RF is expected to be double that of M-RF, it may be assumed that some of the excess PEI remains adsorbed in the porous structure leading to the inordinately high nitrogen content as seen in Table 5. The additional affinity of Ni to the PEI nitrogen can be assumed to play a part in affecting the porous structure of the formed MRFs, and this is discussed in some detail in a later section. The actual incorporation of Ni is 0.7wt% as compared to 1.3wt % for Co, which will be translated to nearly half, in terms of molar incorporation, given their comparable atomic weights. The incorporation of Co with progressively increasing content in reaction mixture is representative of the expected ratios of incorporation.

Table 4

Carbon, Oxygen, Nitrogen, Cobalt and Nickel in various RF catalyst based on elemental analysis by E DS ((%W)

Sample	**Carbon**	**Oxygen**	**Nitrogen**	**Cobalt**	**Nickel**
RF	62.6	31.4	0	0	0
M-RF	77.6	20.1	2.3	0	0
H-RF	60.7	28.9	10.4	0	0
Co1-M-RF	60.9	31.3	7.4	0.4	0

Table 4 (continued)

Sample	Carbon	Oxygen	Nitrogen	Cobalt	Nickel
Co3-H-RF	63.9	33.3	2.0	0.8	0
Ni3-M-RF	73.2	23.4	2.7	0	0.7

Fourier transform infrared (FTIR) spectra was used to characterize the chemical structures of synthesized N-OMPs, and these are shown in Figures 12 a-d. While Figure 12 a, shows the spectrum of a general resorcinol formaldehyde resin, Figure 11 b shows the FTIR spectra of the MRF made with 1.96% PEI. In Figure 11 c, the spectra of MRF with 1.96% PEI and 3% Co is shown as an example, while figure 11 d shows the corresponding resin with 3% Ni instead of Co. The change in the positions of the characteristic peaks with a change in the metal center is insignificant, pointing to very little difference in the bonding characteristic with the metal center. In the FTIR spectra, the characteristic peaks associated with phenolic resins are observed, like the absorption bands of benzene rings at 800–900 cm^{-1}, the bending vibration of the C-O bond at 1157 cm^{-1}, the absorption band of the methyl group at 1219 cm^{-1}, the absorption bands of the methylene bridge at 1445 and 2827–2963 cm^{-1}, and the stretching vibration of the O-H bond at 3200–3400 cm^{-1}. Besides, the characteristic peaks associated with nitrogen species are also observed. For example, the stretching vibration of the C-N bond at 1110 cm^{-1}, the bending vibration of the N-H bond at 1605 cm^{-1}, and the stretching vibration of the N-H bond at 3400–3500 cm^{-1}.

The thermal stability of the MRFs was evaluated by employing thermal analysis by heating the samples in an inert atmosphere. To remove moisture, the samples were warm up to 100 °C and then the weight loss measurement started at 50 °C to 600 °C under a constant nitrogen flow rate. The various compositions differed substantially in their thermal stability profiles and this is shown in Figures 11d-f. Thermal stability of RF is slightly better than M-RF as seen in Figure 11d. It could be construed that the presence of the amine functionality causes a more rapid breakdown of the polymeric structure with temperature due to a catalytic action. The thermal stability of 3% Co is superior to both that containing 1% and 5% Co contents. The MRF with Co3-M-RF showed more thermal stability compared to a composition containing a closely comparable content of nickel.

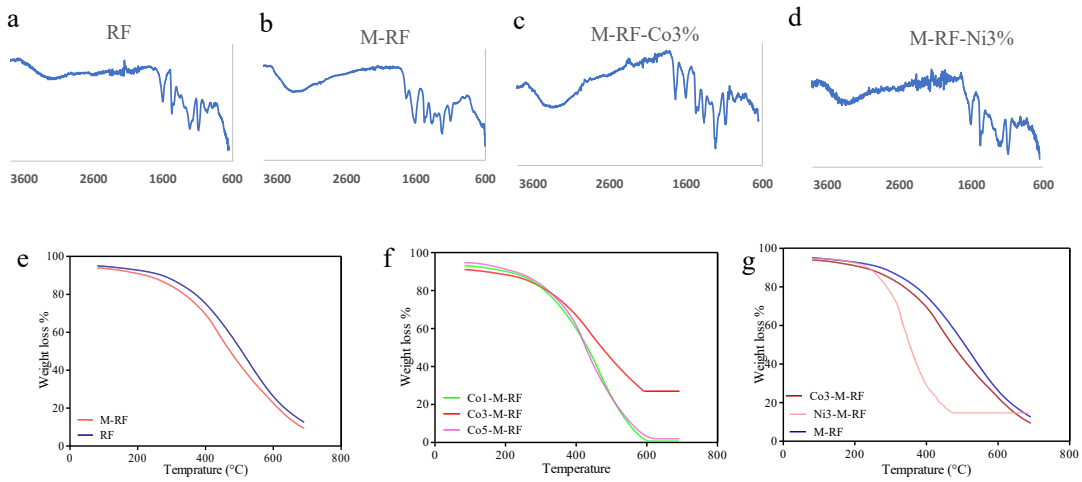

Figure 11. FTIR spectra (a) RF resin (b) Mesoporous catalyst without metal centers (C MRF with 3%Co (d) MRF with 3% Ni, Thermogravimetric Analysis (e) RF and MRF without metal centers (f) MRF with Co 1%,3% and 5%, (g) Comparison of M-RF with M-RF-3% Co and M-RF-3% Ni

Usually, the presence of a higher loading of PEI with a high loading of amino groups causes rapid carbonization of the polymer network resulting in a sharp and rapid weight loss. PEI may attract moisture and cause an earlier breakdown of benzoxazine connectors with concomitant thermal breakdown. Samples containing a Co have more thermal stability compared to those containing Ni. Ni is known to exhibit greater bonding to PEI nitrogens entailing the coordination of a donor heteroatom with an eletrodeficient metal center. The lone pair of electrons on PEI nitrogens form a donor complex with Ni, causing a catalytic effect on the breakdown of Ni containing MRFs compared to the more innocuous Cobalt nucleated MRFs [180-181].

5.3.2. Surface area and pore structure. The nitrogen adsorption/desorption isotherms were obtained by NOVA Tech at 76K and plotted in Figure 12. The surface area

for all samples was calculated by multipoint BET model based on adsorption plot and showed in Table 5. The detailed porosity parameters of pore size volume and diameter were calculated by BJH model and are summarized in this table. Varying the concentrations of PEI, cobalt, and metal salt has a visible influence on the textural and surface morphologies of the MRFs. The porosity can be significantly improved by varying the PEI and Co concentrations. However, the effect is not linearly correlated to their concentration. Increasing PEI concentration, as seen in the metal-free mesoporous polymers, from 0% (RF) to a content of 1.96% (M-RF) increases the BET surface area from 19.6749 m^2/g to 325.99 m^2/g. A further increase in the PEI content to 3.98% (H-RF) decreases it to 212.125 cc/g.). It may be argued that, as per the RF-PEI network formation reaction, a PEI addition over and above the limit of crosslinking - which is determined by relative component stoichiometries may be thought to cause the PEI to merely enter the already formed pores in the form of a liquid, blocking them, thereby reducing the available surface area in the BET experiment.

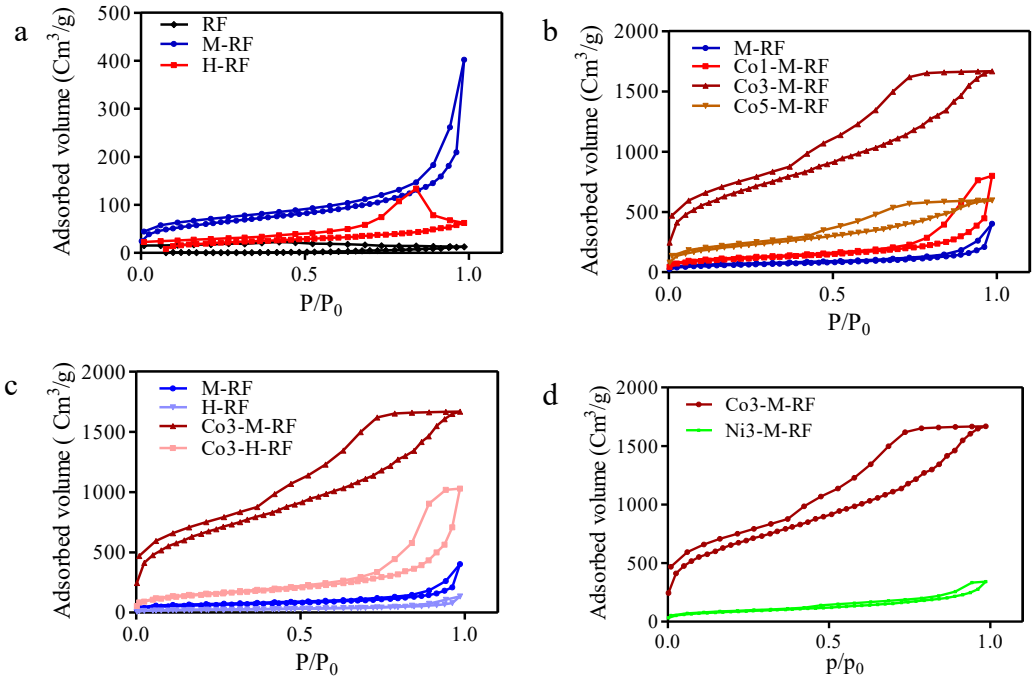

Figure 12. N_2 adsorption−desorption isotherms of (a) RF with varying PEI concentration, (b) Co-M-RFs with varying cobalt concentrations, (c) Cobalt doped RF made with varying PEI and Cobalt concentration, and (d) Metal -doped M-RF with cobalt and nickel (RF = nonporous resorcinol-formaldehyde resin; M and H refers to 1.96 and 3.98% w PEI, Co= Cobalt, and Ni= Nickel, 1= 1 wt% and 3= 3 wt% of cobalt or nickel, respectively).

With 3% Co doping using the 1.96% PEI containing MRF, the BET surface area increases to 977.111 m^2/g. This composition is designated as Co3-M-RF. With 1% Co the BET surface area decreases compared to the composition without Co doping. With a much higher 5% Co doping there is an insignificant change in surface area compared to the undoped MRF structure. The percentage increase in the surface area for 1.96% PEI MRF (M-RF) with Co doping is much starker compared to those containing a higher PEI content of 3.98% (H-RF). With M-RF, incorporation of 3% Co increases the surface area by more than 200%, while with a higher PEI loading (H-RF), the same incorporation of Co increases

the surface area by only 61.3%. The doping using Co may be thought to induce morphological nucleation of the polymer, which, in tandem with the crosslinking kinetics, forms an optimized structure with the maximum possible surface area. The nucleation and cross-linking have their kinetic rates, which appear to be experimentally optimized at 3% Co content. Neither lower nor higher percentage of Co doping seen to have obtained the same optimization to maximization of surface area, and this is seen in Figure 12b. In Figure 12 c, the significantly higher surface area of the polymer with 3% Co and 1.96% PEI, merely underscores the points made above of the optimized level of Co and PEI incorporation to achieve the best possible results.

Table 5

Surface area and pore size distributions of various catalyst based on BJH model

Sample	BET data	Mesoporous Based on BJH Model		
	Surface area BET (m^2/gr)	Surface area (m^2/gr)	Pore Volume (Cm^3/g)	Pore size radius (nm)
RF	19.6746	13.5263	0.0408888	28.7892
M-RF	325.99	207.011	0.354766	1.61736
H-RF	212.125	80.068	0.344372	2.38722
Co1-M-RF	220.117	108.112	1.14271	1.99524
Co3-RF	149.802	149.802	0.2471165	1.8915

Table 5 (continued)

Sample	BET data	Mesoporous Based on BJH Model		
	Surface area BET (m^2/gr)	Surface area (m^2/gr)	Pore Volume (Cm^3/g)	Pore size radius (nm)
Co3-M-RF	977.111	226.094	1.83419	1.1158
Co3-H-RF	342.222	123.286	0.1460002	1.6842
Co5-M-RF	375.19	98.7302	0.707911	1.52765
Ni3-M-RF	264.819	87.0842	0.203323	1.69119

Co has a more pronounced effect in increasing surface area than Ni does on the polymer composition made 1.96% PEI and this is seen in Figure 12 d. While both Co and Ni have six coordination sites each, Ni is known to have a higher affinity for amino coordination, as seen in polyhistidine tag chromatography. The weaker affinity of Co in protein chromatography results it in being less deleterious on the structure of the protein by way of lower bonding affinity. A similar process can be thought to occur in this structure. Here, morphological nulceation is expected to work alongside cross linking of the polymeric structure. The lone pair of electrons on the PEI amine center coordinate with the Ni vacant orbitals. This nucleation competes with the rate of crosslinking. Hence a higher affinity with Ni may cause a more pronounced disruptive effect on structure

formation and porosity. A milder coordination between PEI amine lone electron pairs and the Co centers causes a more even distribution of crosslinking and nucleation leading to a better development of surface area and porosity [182-183]. The isotherm was found to match to Type IV adsorption curves, indicating the presence of multilayers. However, in the case of RF, the obtained isotherm showed Type IV and V. The SEM images of various MRFs was illustrated in Figure13 a-g, and confirmed uniform microporosity of samples containing PEI.

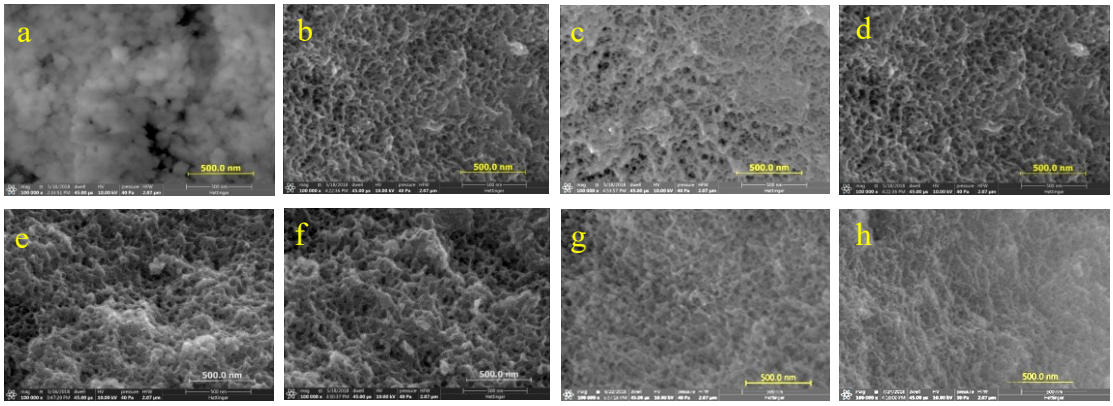

Figure 13. SEM of various samples: (a) RF (b) M-RF (c) Co1-M-RF (d) Co3-M-RF (e) Co5-M-RF(f) Co3-H-RF (g) H-RF (h) Ni3-RF

The SEM images reflect the results and observations in the figure 13 and table above. The spherical morphology of RF (Figure 13 a) is another proof for the importance of PEI in developing a uniform morphology with an interconnected framework, which can be seen in subsequent images. The immobilization of Co increases pore interconnection with consequent enhancement in surface area, as mentioned above. It is obvious that excessive incorporation of either PEI or Co destroys the clean morphology that is obtained

with 1.96% PEI and 3% Co, which again is testament to the empirically obtained optimization of the nucleation and cross-linking reactions. The SEM images also affirm that Ni is not as effective in inducing the morphological optimization as is seen with Co doping.

5.3.3. Carbon dioxide adsorption. The carbon dioxide adsorption results are presented in Figure 14 a-f. The MRFs were utilized as adsorbents for CO_2 adsorption at 25 °C or 0 °C and 1 bar. CO_2 adsorption isotherms of MRFs are shown in Figure 14 a and d. The CO_2 uptake at 1 bar is presented in Figure 14 b,c,e, and f. The adsorption results with 3% Co and 1.96% PEI content shows the best adsorption results. One primary reason is that the surface areas of this sample were seen to be higher than other samples. The high PEI containing samples perhaps had quite a bit of the pore blocked by the presence of PEI in liquid form blocking gaseous movement through the mesopores and hence its subsequent adsorption. This is reflected in Figure 14 b, where despite higher PEI ratios, which is expected to attract more CO_2 due to its alkaline disposition, the reality remains that the compositions with higher PEI incorporation results in lower surface area and hence diminished adsorption.

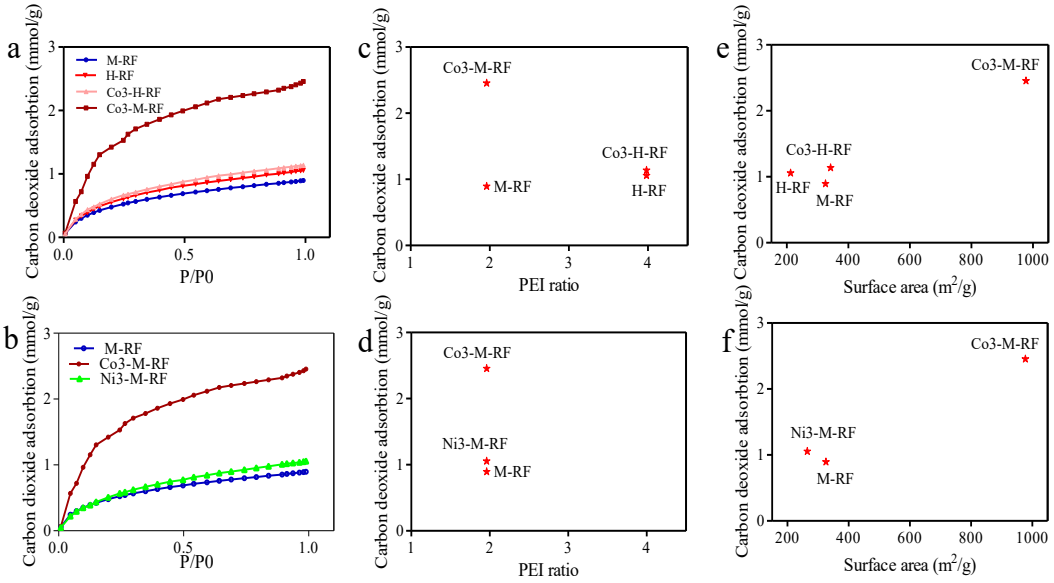

Figure 14. Carbon dioxide absorption of various composition(a-b) at 0 ºC (c-d) Carbon absorption at 0 ºC and 1 bar verse PEI ratio(e-f) Carbon absorption at 0 ºC and 1 bar verse surface area

The importance of surface area available for adsorption is underscored in Figure 14 c where the composition with the higher surface area adsorbs the higher amount of CO_2 despite having lower incarnation of PEI compared to H-RF structures. M-RF, which has a low surface area (325 m^2 g^{-1}) and pore volume (0.13 cm^3 g^{-1}), exhibits a CO_2 uptake of 1.15 mmol g^{-1}. Co doped sample with same PEI concentration Co3-M-RF also shows a high CO_2 adsorption capacity (2.5 $mmolg^{-1}$ at 0 °C and 1 bar). Ni3-M-RF displays a CO_2 adsorption capacity of 1.05347 mmol g^{-1} at 0 °C, 1 bar. Previous research demonstrates that resorcinol- formaldehyde resin exhibit stronger Lewis basicity, and generally have good CO_2 capture capabilities. In Figures 4 e and f, despite a comparable amount of PEI, the sample containing Co has superior CO_2 adsorption simply owing to the much higher surface area. By increasing the concentration of PEI, from 0 to 3.98%, little increase in

CO_2 adsorption was observed, while by increasing Co concentration, the CO_2 adsorption enhanced sharply. By increasing the PEI concentration from 1.96 to 3.98%, the adsorption efficiency decreased from 2.58 to 2.27, for Co-doped M-RF (3.1% decrease), which trend looks like BET surface area.

5.3.4 Carbon dioxide electrochemical conversion. For evaluating the catalytic activity, different MR catalysts were coated on the top of the glassy carbon electrode. Then electrolyte solution was saturated by argon (inert gas) or carbon dioxide. LSV and MCA experiments were done under the blanket of argon/carbon dioxide at room temperature. As seen in Figure 15, the trend showed MR-Ni showed maximum electrochemical conversion activity and then MR-Co and MR.

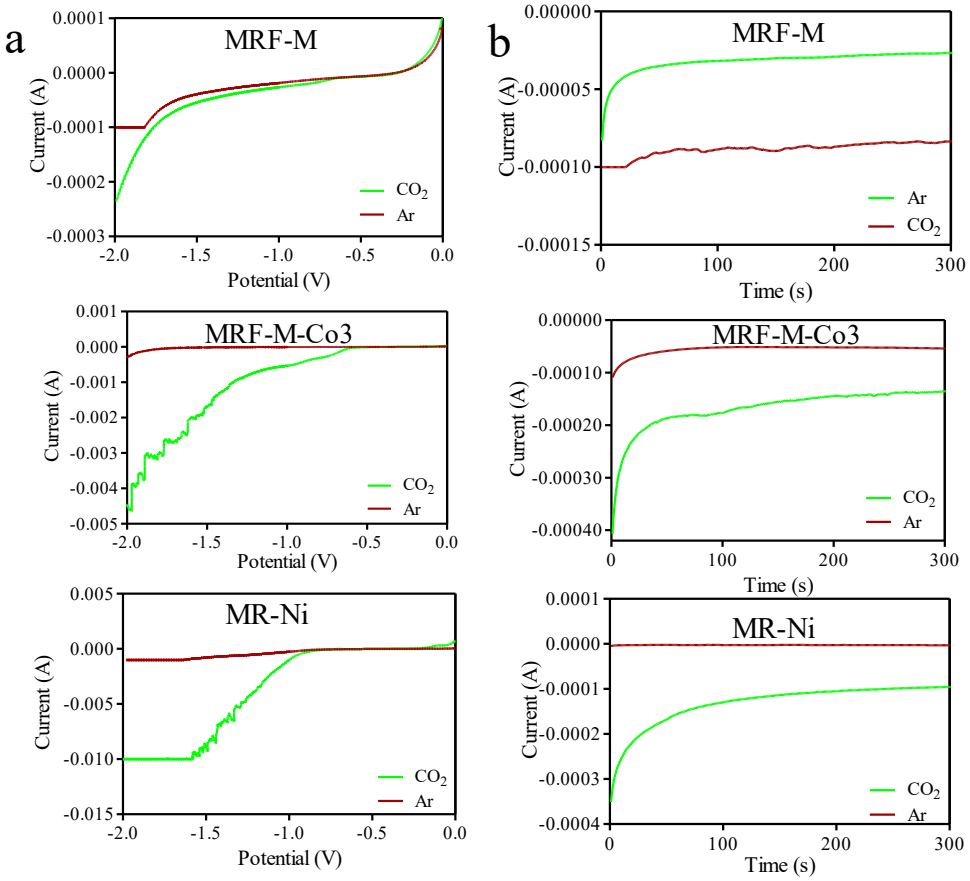

Figure 15. Carbon dioxide Conversion rate for various MR catalyst under argon and carbon dioxide (a) LSV (b) MCA at Constant voltage -1 V

5.4. Conclusion

In summary, this chapter presented a novel, template-free, and generalized method for the fast and scalable synthesis of metal-centered mesoporous polymer for CO_2 capturing and for its possible subsequent conversion by metal-catalyzed electrochemical reduction. The presented method can strongly promote the industrial application of mesoporous polymer by overcoming a series of process and scale-up limitations associated with the traditional template-based self-assembly route. Owing to abundant nitrogen

content, high functionality, and predominantly mesoporous nature, the synthesized MRFs demonstrated excellent capacity for CO_2 adsorption. Moreover, the N-OMPs derived catalysts show excellent performance for the transformation of CO_2 into CO. Based on these results, it can be concluded that a combination of metal functionality and meosporosisity is very important for CO_2 adsorption and catalytic conversion of CO_2. Thus, this work provides an initial novel insight for designing porous materials with high performance for the selective capture and conversion of CO_2 from flue gas. The FTIR results, SEM, and elemental analysis validated the incorporation of different kinds and contents of nitrogen species into the framework synthesized MRFs. The nitrogen adsorption isotherms at -196 °C and SEM images revealed that the synthesized MRFs have large surface areas and abundant meso–macropores. The CO_2 and N_2 adsorption experiments demonstrated that the synthesized MRFs have a high capacity for CO_2 at a relatively low pressure of 0.15 bar (0.64–1.47 mmol g^{-1} at 0 °C and 0.49–0.87 mmol g^{-1} at 25 °C). This work provides a facile approach to the targeted synthesis of nitrogen functionalized MRFs with potential applications in the s capture and electrochemical conversion of CO_2.

Chapter 6

Evaluation Biocompatible Palladium Doped Resin for In-Situ Drug Synthesis

6.1 Introduction

Cross-coupling reactions can be used for in-situ synthesis of an active compound from its nonactive precursors. Different substrates, catalysts, and reaction conditions have been used in vitro; however, applications in the more complex biological environment, like cells or living organisms, are still limited. This is mainly due to catalyst deactivation caused by the complex cellular environment that includes proteins and thiols [82-84]. To overcome these limitations, a possible solution would be to trap the metal catalyst into solid support, therefore protecting the active site from the deactivating agents. Also, coupling an active metal complex to a cell delivery agent could be used to increase tissue/cell selectivity, biocompatibility, uptake of the active compound, and subsequently perform intracellular chemical reactions [88]. For example, Rotello and co-workers used the encapsulation of a homogeneous Pd catalyst on the surface of gold nanoparticles and evaluated their ability to intracellularly activate a prodrug of the anticancer agent (5-fluorouracil) [88-92]. In another research, heterogeneous palladium nanoparticles were embedded in polymer structure and applied successfully in the intra- and extracellular activation of caged fluorophores [93]. The entrapped palladium was used to catalyze the C–C bond formation *via* Suzuki-Miyaura cross-coupling reactions and C–O bond cleavage inside living cells. Despite the progress, there are few reports. Indigo at et al. used heterogeneous palladium catalyst for synthesis PP121 anticancer agent against the PC3 cells in 2D in vitro culture [94].

In this chapter. The synthesized Pd-MPRs are a biocompatible heterogeneous catalyst with high efficiency for in situ Suzuki-Miyaura reaction to produce PP121

anticancer molecule. The high surface area, pore-volume, and pore size of Pd-MPRs catalysts are favorable for highly efficient PP121 synthesis. Also, the high thermal stability prevents the decomposition of the polymeric backbone which leads to cytocompatibility.

In-situ synthesis of PP121 (anti-cancer drug) catalyzed by Pd-MPRs was evaluated on the prostate cancer cell line (PC3 cells) in 2D and 3D model culture in vitro. To study biocompatibility of catalyst, cells metabolism was evaluated by Presto-Blue assay. In addition, cell viability and morphology were studied by live and dead assay and Actin-DAPI staining. Figure 16 demonstrates the schematic.

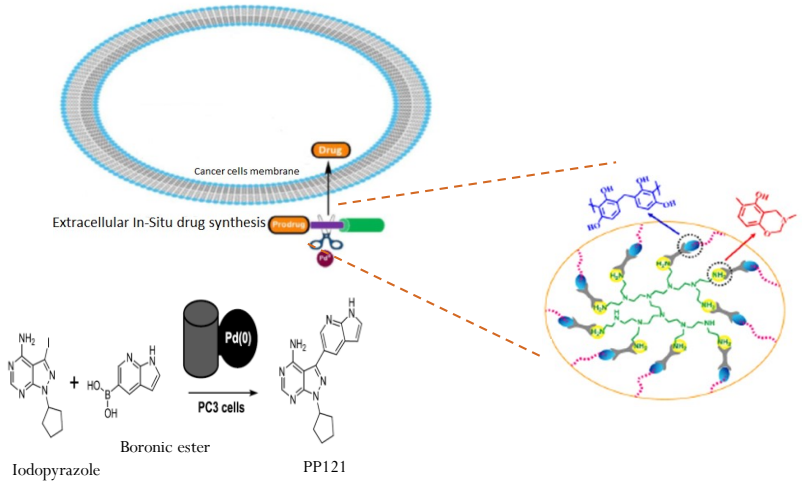

Figure 16. Schematic of extracellular in-situ drug synthesis

6.2 Materials and Methods

Pd-MPRs catalyst was synthesized as explained in chapter four. PC3 cells were a gift from Dr. Pandey's lab and cultured in RPMI-1640, containing 10% FBS and 1%

penicillin/ streptomycin. GelMA was synthesized, as explained in chapter three. Sodium alginate powder dissolved in PBS and sterilized by syringe filter 0.2 μm. Lithium phenyl-2,4,6-trimethylbenzoylphosphinate (LAP) was used as photo initiator and dissolved in PBS. For cell encapsulation, GELMA, alginate, and LAP was mixed to desired concentration and then cell suspension (5* 10^{-6} cells/ml) was added to it. The viability of PC3 cells grown on the surface of MR-Pd hydrogels was evaluated using a commercial Live/Dead viability kit (Invitrogen), according to instructions from the manufacturer. Briefly, cells were stained with 0.5 μl/ml of calcein AM and 2 μl/ml of ethidium homodimer-1 (EthD-1) in PBS for 5 min at 37 °C. Fluorescent image acquisition was carried out at days 1, 3, 5, and 7 post-seeding using an AxioObserver Z1 inverted microscope (Zeiss). Viable cells appeared as green and dead cells appeared as red. The number of live and dead cells was quantified using the ImageJ software. Cell viability was determined by the number of live cells divided by the total number of live and dead cells. The Presto/Blue assay was carried out in 12-well. Each well contained the cells to be tested with cultured medium or rinsing solution removed. 500 μl (for 12-well plates) Presto/Blue solution (10% in medium without serum) was added to each well, and the plates were incubated at 37 °C for a specified time period. Simultaneously, fresh serum-free media were incubated in new well plate as blank. After incubation, 100 μl of the Presto/Blue solution from each well of the assay plates (96-well plates) was transferred to a new well in 96-well plate, and the change in the fluorescence of the test reagent was measured in the new plate using a fluorescence multi well plate reader with the excitation/emission wavelengths set at 530/590 nm.

The Muse® Annexin V & Dead Cell Kit was applied for the quantitative analysis of live, early, and late apoptosis and cell death cells on the flow cytometer (Guava® Muse® Cell Analyzer). Concentrations (cells/mL) and percentage for live, early apoptotic, late apoptotic, total apoptotic, and dead cells were calculated by MUSE software. For monolayer, cell scraper was used to detach cells, then 20 µl of cell suspension mixed with 20 µl of Muse® Annexin V & Dead Cell and incubate at the dark place at room temperature for 20 min. Then the sample was placed in the flow cytometer and ran the ® Annexin V & Dead Cell assay. Each sample was measured three times.

6.3 Results

6.3.1 Pd-MPRs synthesis and characterization. As mentioned above, a successful catalyst should have some special properties. Figure 17 a showed the nitrogen adsorption of Pd-MPRs. This graph confirmed meosporosity of this catalyst with high surface are (675 m^2/gr. In addition, uniform structure and homogenous distribution of palladium considered by SEM and EDX respectively (Figure 17 b and c). For catalyzing this in-situ drug synthesis, the catalyst should be contained enough Pd0, which illustrated by XPS analysis in Figure 17e.

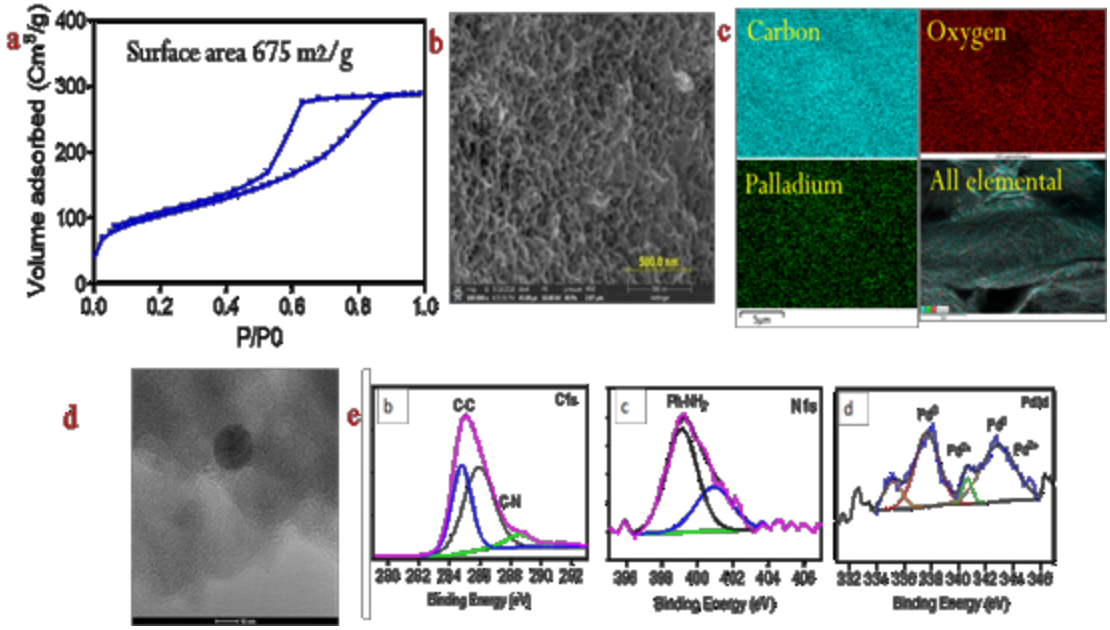

Figure 17. (a) N2 adsorption–desorption isotherms based on Brunauer– Emmett–Teller (BET) surface area method (b) SEM (c) EDS elemental analysis (d) TEM (e) XPS of MR-Pd

6.3.2 Pd-MPRs biocompatibility. The main key for using this catalyst for in-situ drug synthesis is biocompatibility. The monolayer in-vitro model was used to evaluate this property. Figure 18 showed the results of the biocompatibility test. The cells were seeded in a 24-well plate, and after one day, 10mg of sterile catalyst (300 to 500 μm) was added to each well. And then, at various time points (1, 3, and 5 day) cells stained by live/dead kit and 5 images were taken from each well (some of the images showed in Figure 18-a). The images were processed by Image J software and the quantitative data demonstrated in Figure 18-b. As this plot showed, cell viability of control is equal with catalyst one. The metabolism activity of cells was measured by Presto- Blue assay. Figure 6.3-d displayed

the cell expansion fold is almost equal for control (cells cultured without catalyst) and catalyst one. These results confirmed the biocompatibility of this catalyst. Furthermore, Actin-DAPI cell staining disclosed proper interaction between the cells and catalyst (Figure 18-c).

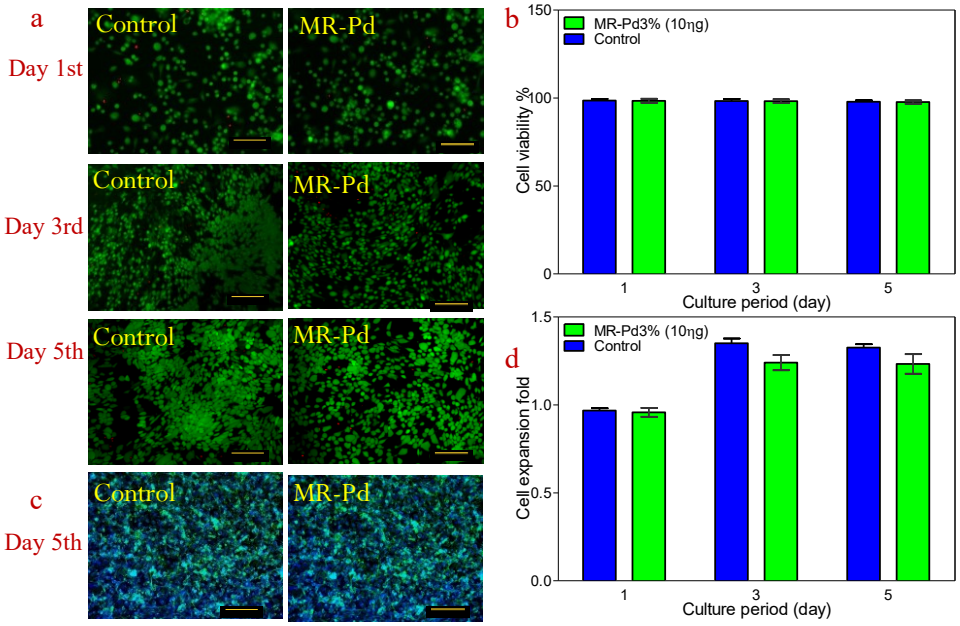

Figure 18. Biocompatibility of MR-Pd catalyst (a) Live & dead assay florescent microscopic images (b) Quantitated cell viability based on image processing (c) Actin-DAPI staining day 5th (d) Cell expansion fold based on Presto-Blue assay

6.3.3 Mono layer model for in-situ drug synthesis. Standard monolayer cultured was used to considered in-situ drug synthesis. After seeding the cells for two-day, monolayer with confluency, 50% was used for in-situ drug screening. The results illustrated in Figures 19 and 20.

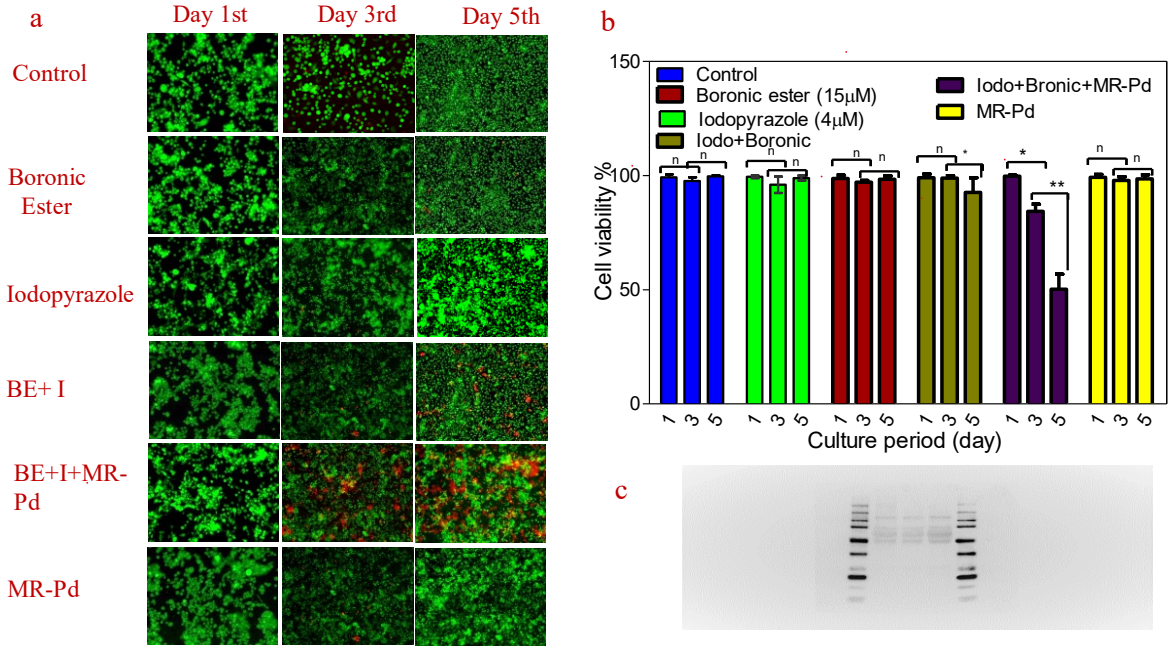

Figure 19. In-situ drug synthesis for monolayer PC-3 cells culture model. (a) cell viability based on live & dead assay (b). Cell expansion based on Presto-Blue assay (c) Western blot

The result of processing image of cells viability Figure 19 a) showed in Figure 19 b. These results confirmed PC3 cells death by in-situ PP121 synthesis. The number of dead cells increased from 10% to 57% on day 3rd and 5th by live/dead assay, respectively. The flow cytometry results also confirmed the increasing rate of early and late apoptosis (Figure 20 b). Besides, cell metabolism activity declined (Figure 20 c) based on the Presto-Blue

assay. In fact, these three assays confirmed cells death because of synthesized PP121 extra cellular in-situ.

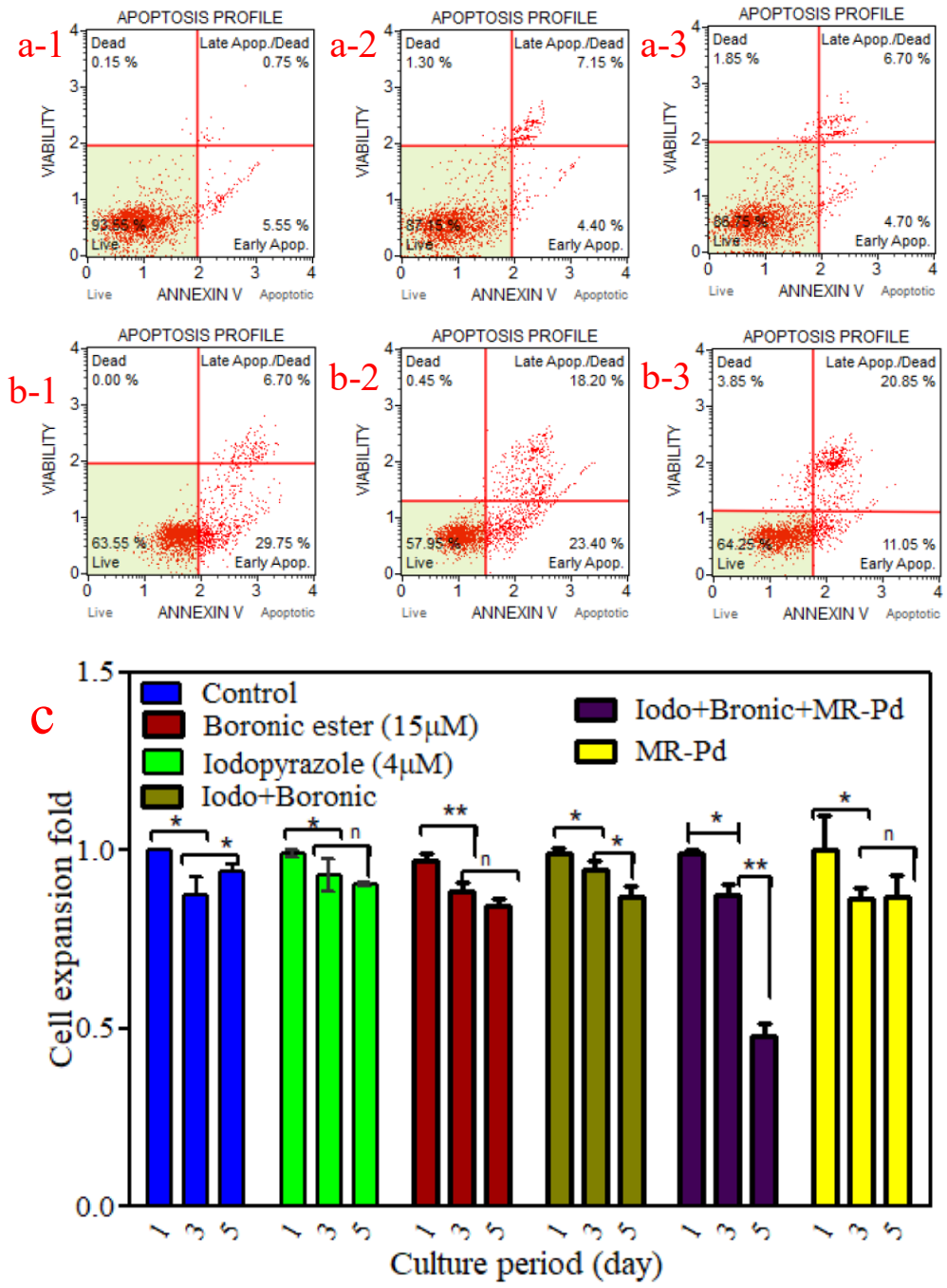

Figure 20. In-situ drug synthesis for monolayer PC-3 cells. cell viability based on flowcytometry assay (a1-3) Control day 1,3, and 5 respectively (b1-3) In-situ drug synthesis in present of MR-Pd catalyst day 1,3, and 5 respectively (c) Cell expansion fold based on Presto-Blue assay

6.3.4 Developing 3-D model for in-situ drug synthesis. The literature review showed 3D model is more proper to evaluate drug screening due to mimicking cells microenvironment. In this section, GelMA – alginate hydrogel was used to encapsulate PC3 cell line. Then this simple model was used to evaluate drug screening. At first, two main compositions were used to encapsulate PC3 cells, GeLMA5%-Alginate 1.5%- LAP 0.1% and GeLMA7%-Alginate 1.5%-LAP 0.1%. The SEM results showed by increasing concentration of GelMA from 5 to 7 porosity decreased. While the swelling ratio of these two compositions is almost the same, but a hydrogel containing 7% GelMA is more stable (degradation ratio plot Figure 21 c).

The cells proliferation rate based on Presto-Blue assay established in Figure 21 e. The data showed by increasing GelMA to 7%, cell proliferation rate increased. However, western blot showed CXCR4 expression for monolayer, and encapsulated cells are equal (Figure 21f).

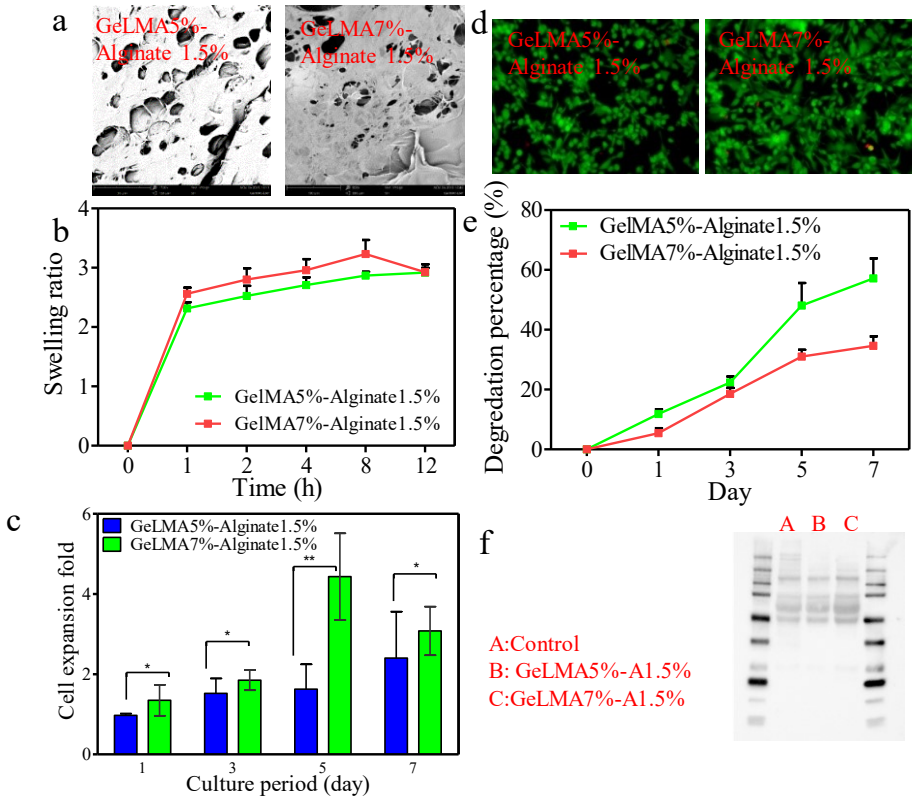

Figure 21. Evaluation encapsulated prostate cells (PC-3) in hydrogel (a)SEM (b) swelling ratio (c) degradation percentage of various hydrogel composition (d) cell staining by live & dead kit day 1st (e) cell expansion based on Presto-Blue assay (f) Western Blot for incapsulated cells

We used two strategies for this section. First, PC3 cells were encapsulated in GelMA7% -Alginate 1.5%- LAP1%, and then after 5 days of encapsulation, the in-situ drug screening test was started. Second, PC3 cells encapsulated in GelMA7% -Alginate 1.5%- LAP1% with 5mg catalyst. Then at day 3 drug screening test is started. In both strategies, the prodrug dissolved in medium culture as same as monolayer study. The catalyst was added to the well plate or injected into the encapsulated cells. The catalyst was injected on 4 days, and the test started at 5 days. Presto-Blue results showed in Figure 22 a and b for these two strategies, respectively.

Also, flow cytometry results showed after 7 days of the drug screening test, the population percentage of late apoptosis cells for the samples which catalyst injected inside of encapsulated cells were more significant (Figure 22 c-2 and d-2).

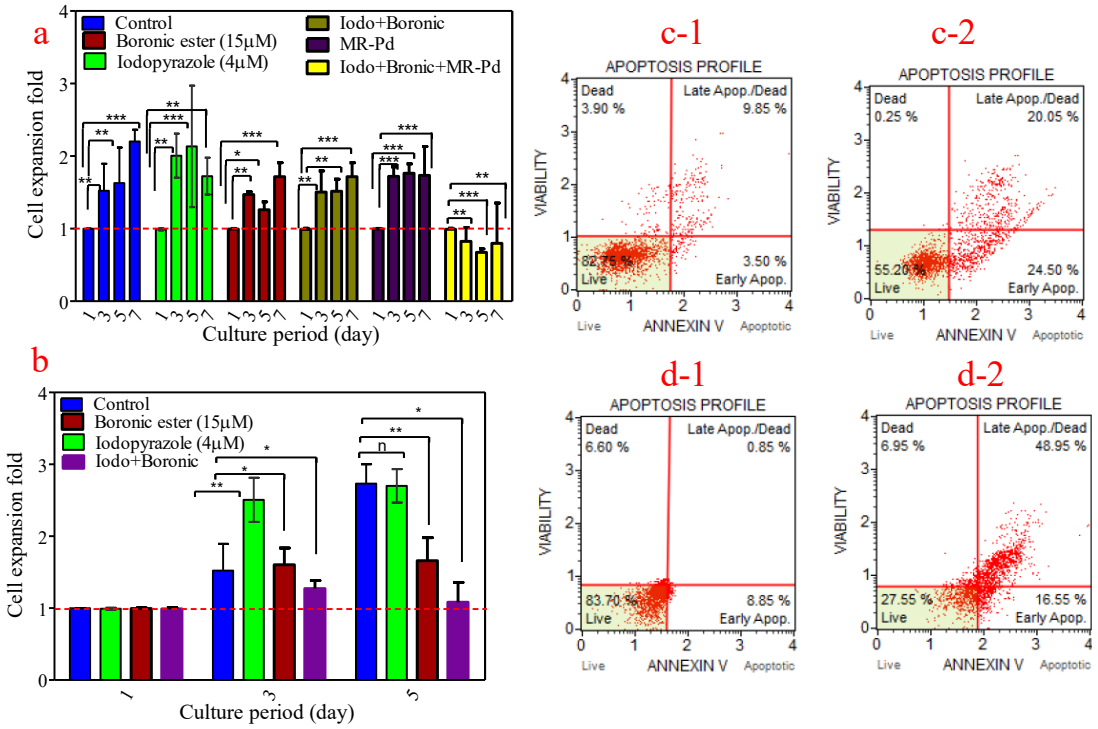

Figure 22. In-situ drug synthesis for encapsulated PC-3 cells (started after 7 days of culture). cell proliferation based on Presto-Blue assay (a) Encapsulated PC-3 cells in GelMA- Alginate (7%:1% w/v)(b) Encapsulated PC-3 cells in GelMA- Alginate-MR-Pd (7%:1%:0.1% w/v) Cell viability based on flowcytometry (c1-c2) Encapsulated PC-3 cells in GelMA- Alginate (7%:1% w/v) (d1-d2) Encapsulated PC-3 cells in GelMA- Alginate-MR-Pd (7%:1%:0.1% w/v)

6.4 Discussion

Loading of an active metal to a polymeric solid support is a common method to generate heterogeneous catalysts. Palladium nanoparticles have been successfully

absorbed onto phenol-formaldehyde resin and showed high catalytic activity in biological systems. In this study, Pd-MPRs was evaluated to synthesize PP121 (anticancer drug), giving two precursors that can be coupled together via a palladium-catalyzed Suzuki-Miyaura cross-coupling reaction. This strategy offers a way to activate anticancer drugs in response to an external stimulus, thus expanding the chemotherapy efficiency. In the future, an inactive drug precursor will be activated just in the presence of a selectively delivered palladium catalyst, thus minimizing the side effects of the treatment on the whole body. The cytotoxicity of PP121 was evaluated with PC3 cell lines in previous work, and here a Presto-Blue assay and flow cytometry was used to consider it. Pd-MPRs showed remarkable efficiency for extracellular in-situ drug synthesis in two models. Cytotoxicity towards PC3 cells monolayer is more than a 3D model.

Chapter 7

Conclusion and Expanded Recommendations for Future Work

7.1 Conclusion

Mesoporous Phenol- formaldehyde Resin (MRF) structures offer simultaneous advantages of functional groups on the polymer structure and a high surface area due to control of configuration, which finds multiple applications in catalysis, energy storage, sensors, adsorption, and separation process. In this work, MRF was synthesized by a single step template-free, low cost, and hydrothermal method, to overcome a major drawback of the common hard/soft-template method. Resorcinol and formaldehyde were used precursors along with the branched Polyethyleneimine (PEI) to arrive at a mesoporous resin structure. The facile, solvent, and template-free, low-temperature synthesis proffers these materials as easy to use catalysts for metal ion-doped for cross-coupling or carbon dioxide capturing and conversion. The template-free, aqueous phase, one-pot synthetic procedure facilitates scaling up of this catalyst for commercialization. Besides, the results in Chapter 4-6 confirm the high potential of these catalyst structures for pharmaceutical, environmental, and medical applications.

The catalysts are metal centered in the structures with palladium, cobalt, and nickel. The mesoporous structure is a cost-effective and chemo/thermal stable support for the metal centers. The experimental results in Chapter 4 showed that the palladium doped MRF catalyst achieves a high conversion rate (98%) for cross-coupling reactions. The high surface area (675.34 m^2/g) and thermal stability achieved with a 3% palladium acetate (w/w) structure make the structure an excellent candidate for heterogeneous Suzuki-

Miyaura cross-coupling catalysis, achieving a high conversion rate of up to 5 reaction cycles. Applicability in a model micro packed bed reactor confirmed the possibility of industrial usage. This synthesis strategy provides a benchmark for fabricating a well-defined mesoporous structure with the potential for catalyst applications in pharmaceuticals synthesis.

In Chapter 6, a review of biocompatible performance opens a new vista of biomedical applications in oncology. In-situ drug synthesis was introduced in the early 2000s to reduce the side effect of chemotherapy, with increased efficiency. This chapter aimed to evaluate the palladium doped resin (Pd3-M-RF) as a biocompatible catalyst for extracellular in-situ drug synthesis. Pd-MPRs catalyzed two prodrugs for anti-cancer P121 drug synthesis in 2D and 3D in-vitro models. Cell proliferation rate was monitored during drug screening tests. Flow cytometry, done to understand the process efficiency showed early cancer cell apoptosis after one day of adding prodrug, achieving maximum results after seven days. However, due to mass transfer limitation, cytotoxicity towards PC3 cells is more in the 3D model, despite effectively killing cancer cells in large numbers. Pd-MPRs showed remarkable efficiency for extracellular in-situ drug synthesis in both models.

In addition, this method was used to synthesize catalysts doped with other metals, using a facile method for targeted synthesis of nitrogen-functionalized MRFs for potential CO2 capture and electrochemical conversion. Co and Ni-doped resin (MRFs) with tunable metal functionality and hierarchical porosity were evaluated. The effect of PEI and metal doping concentrations were observed on physical and adsorption properties. The results confirmed the role of PEI on the mesoporosity of the polymer networks and high surface area, which enhanced CO_2 capture capacity. The CO_2 and N_2 adsorption experiments

demonstrated that the MRFs have high CO_2 adsorption at a relatively low pressure of 0.15 bar (0.64–1.47 mmol g-1 at 0°C and 0.49–0.87 mmol g-1 at 25°C). The resultant Co-doped material shows excellent thermal stability and promising CO_2 capture performance, with equilibrium adsorption of 2.3 mmol CO_2/g at 0°C and 1bar for at a surface area 675.62 m^2/g. This mesoporous polymer, with its ease of synthesis, is a promising candidate for promising for CO_2 capture and subsequent electrochemical conversion.

7.2 Expanded Recommendations for Future Work

7.2.1 Developing 3D tumor model for evaluation in-situ drug synthesis. The Prostate cancer tumor is a complicated tissue due to its heterogeneous nature, and the 2D in-vitro model is not adequate for studying drug efficiency. This problem is more important for in- situ drug synthesis, which mass transfer plays a vital role in increasing reaction yield. As prostate tumor contains extracellular matrix (ECM) and high cell density, mimicking the 3D microenvironment of the tumor is too complicated, and the main barrier to designing a proper model for in-vitro study. Indeed, ECM decreases prodrug contacts with the cells. Hence, it will not as easy as the 2D model to consider the drug effect on the cells. Therefore, it is necessary to have a proper 3D model for the in-situ drug synthesis study in-vitro. Our goal in this stage is to mimic the tumor's heterogeneous nature by printing encapsulated cells. Then this 3D printed model was used for studying the in-situ drug synthesis in-vitro and evaluated the effect of PP121 extracellular in-situ synthesis in the presence of heterogeneous palladium catalyst (MR-Pd). HPLC, H-NMR, LC-MS spectroscopy will be used to assess the yield of reaction and conversion. Also, fluorescent

microscopy, confocal microscopy, plate reader, and flow cytometry will be used to evaluate toxicity and reaction efficiency in-vitro. The primary data were shown in Figure S3.

As our goal was to evaluate this catalyst at the in-vitro condition, the prostate tumor mimicked by printing encapsulated PC3 cells in GelMA (Gelatin methacrylate). This model is more useful than a 2D study because of the similarity of the 3D structure of hydrogel with the primary tumor in the body. After we developed cancer entirely, at the next step, the catalyst particles will be inserted into it. Then in-situ drug synthesis would be evaluated by MTT assay and confocal microscopy imaging based on live and dead staining.

References

[1] Danis TG, Albanis TA, Petrakis DE, Pomonis PJ. Removal of chlorinated phenols from aqueous solutions by adsorption on alumina pillared clays and mesoporous alumina aluminum phosphates. Water Research. 1998 1998/02/01/;32(2):295-302.

[2] Xu J, Wang A, Wang X, Su D, Zhang T. Synthesis, characterization, and catalytic application of highly ordered mesoporous alumina-carbon nanocomposites. Nano Research. 2011 2011/01/01;4(1):50-60.

[3] Liu F, Kong W, Qi C, Zhu L, Xiao F-S. Design and Synthesis of Mesoporous Polymer-Based Solid Acid Catalysts with Excellent Hydrophobicity and Extraordinary Catalytic Activity. ACS Catalysis. 2012 2012/04/06;2(4):565-72.

[4] Kung, Shih-Chieh, Chun-Chih Chang, Wei Fan, and Mark A. Snyder. "Template-Free Ordered Mesoporous Silicas by Binary Nanoparticle Assembly." Langmuir 30, no. 39 (2014/10/07 2014): 11802-11811

[5] Muylaert I, Verberckmoes A, De Decker J, Van Der Voort P. Ordered mesoporous phenolic resins: Highly versatile and ultra stable support materials2012.

[6] Choma J, Jedynak K, Fahrenholz W, Ludwinowicz J, Jaroniec M. Microporosity development in phenolic resin-based mesoporous carbons for enhancing CO2 adsorption at ambient conditions. Applied Surface Science. 2014 2014/01/15/;289(Supplement C):592-600.

[7] Liu F, Gao Y, Zhang S, Yan X, Fan F, Zhao C, et al. Application of mesoporous carbon and modified mesoporous carbon for treatment of DMF sewage. Journal of Nanoparticle Research. 2016 2016/02/08;18(2):38.

[8] Fang Y, Huang X-J, Chen P-C, Xu Z-K. Polymer materials for enzyme immobilization and their application in bioreactors. BMB reports. 2011 2011/02//;44(2):87-95.

[9] Khan MK, Giese M, Yu M, Kelly JA, Hamad WY, MacLachlan MJ. Flexible Mesoporous Photonic Resins with Tunable Chiral Nematic Structures. Angewandte Chemie International Edition. 2013;52(34):8921-4.

[10] Inagaki M, Toyoda M, Soneda Y, Tsujimura S, Morishita T. Templated mesoporous carbons: Synthesis and applications. Carbon. 2016 2016/10/01/;107(Supplement C):448-73.

[11] Jiao, Yucong, Dandan Han, Yi Ding, Xianfeng Zhang, Guannan Guo, Jianhua Hu, Dong Yang, and Angang Dong. "Fabrication of Three-Dimensionally Interconnected Nanoparticle Superlattices and Their Lithium-Ion Storage Properties." Nature Communications 6 (03/03/online 2015): 6420.

[12] Kailasam K, Jun Y-S, Katekomol P, Epping JD, Hong WH, Thomas A. Mesoporous Melamine Resins by Soft Templating of Block-co-Polymer Mesophases. Chemistry of Materials. 2010 2010/01/26;22(2):428-34.

[13] Tanaka S, Doi A, Nakatani N, Katayama Y, Miyake Y. Synthesis of ordered mesoporous carbon films, powders, and fibers by direct triblock-copolymer-templating method using an ethanol/water system. Carbon. 2009 2009/09/01/;47(11):2688-98.

[14] pH-Responsive anionic wormlike micelle based on sodium oleate Induced by NaCl hongsheng Lu, Qianping Shi, and Zhiyu Huang The Journal of Physical Chemistry B 2014 118 (43), 12511-12517

[15] Huang Y, Cai HQ, Yu T, Zhang FQ, Zhang F, Meng Y, et al. Formation of Mesoporous Carbon with a Face-Centered-Cubic Fd(3)over-Barm Structure and Bimodal Architectural Pores from the Reverse Amphiphilic Triblock Copolymer Ppo-Peo-Ppo. Angew Chem Int Ed 2007;46:1089–93.

[16] Huang Y, Cai HQ, Yu T, Sun XL, Tu B, Zhao DY. Highly Ordered Mesoporous Carbonaceous Frameworks from a Template of a Mixed Amphiphilic Triblock-Copolymer System of Peo-Ppo-Peo and Reverse Ppo-Peo-Ppo. Chem Asian J 2007;2:1282–9.

[17] Zhang FQ, Meng Y, Gu D, Yan Y, Chen ZX, Tu B, et al. An Aqueous Cooperative Assembly Route to Synthesize Ordered Mesoporous Carbons with Controlled Structures and Morphology. Chem Mater 2006;18:5279–88.

[18] Li XX, Larson AB, Jiang L, Song LY, Prichard T, Chawla N, et al. Evolution of Mechanical, Optical and Electrical Properties of Self-Assembled Mesostructured Phenolic Resins During Carbonization. Microporous Mesoporous Mater 2011;138:86–93.

[19] Jin T, Xiong Z, Zhu X, Mehio N, Chen Y, et. al., Template-Free Synthesis of Mesoporous Polymers for Highly Selective Enrichment of Glycopeptides, ACS Macro Letters, 2015 4 (5) : 570-574.

[20] Zhang FQ, Meng Y, Gu D, Yan Y, Yu CZ, Tu B, et al. A Facile Aqueous Route to Synthesize Highly Ordered Mesoporous Polymers and Carbon Frameworks with Ia(3)over-Bard Bicontinuous Cubic Structure. J Am Chem Soc 2005;127: 13508–9.

[21] Wan Y, Shi YF, Zhao DY. Supramolecular Aggregates as Templates: Ordered Mesoporous Polymers and Carbons. Chem Mater 2008;20:932–45.

[22] Liu F, Wu Q, Liu C, Qi C, Huang K, et.al., Ordered Mesoporous Polymers for Biomass Conversions and Cross-Coupling Reactions, Chem Sus Chem 2016 vol: 9 (17) pp: 2496-2504

[23] Wu ZX, Hao N, Xiao GK, Liu LY, Webley P, Zhao DY. One-Pot Generation of Mesoporous

[24] Carbon Supported Nanocrystalline Calcium Oxides Capable of Efficient CO2 Capture over a Wide Range of Temperatures. Phys Chem Chem Phys2011;13:2495–503.

[25] Wan Y, Qian X, Jia NQ, Wang ZY, Li HX, Zhao DY. Direct Triblock-Copolymer-Templating Synthesis of Highly Ordered Fluorinated Mesoporous Carbon. Chem Mater 2008;20:1012–8.25.

[26] Gao P, Wang A, Wang X, Zhang T. Synthesis of Highly Ordered Ir-Containing Mesoporous Carbon Materials by Organic-Organic Self-Assembly. Chem Mater 2008;20:1881–8.

[27] Li JS, Gu J, Li HJ, Liang Y, Hao YX, Sun XY, et al. Synthesis of Highly Ordered Fe- Containing Mesoporous Carbon Materials Using Soft Templating Routes. Microporous Mesoporous Mater 2010;128:144–9.

[28] Zhang TM, Zhao DL, Yin L, Shen ZM. Synthesis and Magnetic Properties of Iron Nanoparticles Confined in Highly Ordered Mesoporous Carbons. J Alloys Compd 2010;508:147–51.

[29] Wang H, Wang AQ, Wang XD, Zhang T. One-Pot Synthesized Moc Imbedded in Ordered Mesoporous Carbon as a Catalyst for N2h4 Decomposition. Chem Commun 2008:2565–7.

[30] Sterk L, Gorka J, Jaroniec M. Polymer-Templated Mesoporous Carbons with Nickel Nanoparticles. Colloids Surf A 2010;362:20–7.

[31] Yao JY, Li LX, Song HH, Liu CY, Chen XH. Synthesis of Magnetically Separable Ordered

[32] Mesoporous Carbons from F127/[Ni(H2O)(6)](No3) (2)/Resorcinol-Formaldehyde, Composites. Carbon 2009;47:436–44.

[33] Wan Y,Wang HY, Zhao QF, KlingstedtM, Terasaki O, Zhao DY. Ordered Mesoporous Pd/Silica-Carbon as a Highly Active Heterogeneous Catalyst for Coupling Reaction of Chlorobenzene in Aqueous Media. J Am Chem Soc 2009;131:4541–50.

[34] Jin ZH, Yu C, Wang XY, Wan Y, Li D, Lu GZ. Liquid Phase Hydrodechlorination of Chlorophenols at Lower Temperature on a Novel Pd Catalyst. J Hazard Mater 2011;186:1726–32.

[35] T. Das, H. Uyama, N. Mahasweta, Pd-bound functionalized mesoporous silica as active catalyst for Suzuki coupling reaction: Effect of OAc^-, PPh 3 and Cl^- ligands on catalytic activity, J Sol State Chem 2018;260:132-141.

[36] Li XH, Shen YL, Song LY, Wang HN, Wu HH, Liu YM, et al. Efficient Hydrogenation of Benzaldehydes over Mesopolymer-Entrapped Pt Nanoparticles in Water. Chem Asian J 2009;4:699–706.

[37] Xu JM,Wang AQ,Wang XD, SuDS, Zhang T. Synthesis, Characterization, and Catalytic Application of Highly Ordered Mesoporous Alumina-Carbon Nanocomposites. Nano Res 2011;4:50–60.

[38] Shen YL, Li XH, Song LY, Wang HN, Wu P. Asymmetric Hydrogenation of Ethyl Pyruvate on Chirally Modified Pt Catalysts Supported on Periodic Mesoporous Resols. Chem J Chin Univ 2009;30:1375–9.

[39] Ji ZH, Liang SG, Jiang YB, Li H, Liu ZM, Zhao T. Synthesis and Characterization of Ruthenium-Containing Ordered Mesoporous Carbon with High Specific Surface Area. Carbon 2009;47:2194–9.

[40] Gao P, Wang AW, Wang XD, Zhang T. Synthesis and Catalytic Performance of Highly Ordered Ru-Containing Mesoporous Carbons for Hydrogenation of Cinnamaldehyde. Catal Lett 2008;125:289–95.

[41] Song LY, Li XH, Wang HN, Wu HH, Wu P. Ru Nanoparticles Entrapped in Mesopolymers for Efficient Liquid-Phase Hydrogenation of Unsaturated Compounds. Catal Lett 2009;133:63–9.

[42] Liu R, Ren Y, Shi Y, Zhang F, Zhang L, Tu B, et al. Controlled Synthesis of Ordered Mesoporous C-Tio2 Nanocomposites with Crystalline Titania Frameworks from Organic–inorganic-Amphiphilic Coassembly. Chem Mater 2008;20:1140–6.

[43] Liu D, Lei JH, Guo LP, Deng KJ. A Nanoparticle AssemblyMethod for the Production of Crystalline Ordered Mesoporous Titanium Oxide/Carbon Composites. Microporous Mesoporous Mater 2011;139:87–93.

[44] Muylaert I, Borgers M, Bruneel E, Schaubroeck J, Verpoort F, Van Der Voort P. Ultra Stable Ordered Mesoporous Phenol/Formaldehyde Polymers as a Heterogeneous Support for Vanadium Oxide. Chem Commun 2008:4475–7.

[45] Li Q, Xu J, Wu ZX, Feng D, Yang JP, Wei J, et al. Facile Synthesis of Highly Stable and

[46] Well-Dispersed Mesoporous Zro(2)/Carbon Composites with High Performance in Oxidative Dehydrogenation of Ethylbenzene. Phys Chem Chem Phys 2010;12: 10996–1003.

[47] Yan SY, Gao Y, Xing R, Shen YL, Liu YM, Wu P, et al. An Efficient Synthesis of (E)-Nitroalkenes Catalyzed by Recoverable Diamino-Functionalized Mesostructured Polymers. Tetrahedron 2008;64:6294–9.

[48] Xing R, Wu HH, Li XH, Zhao ZL, Liu YM, Chen L, et al. Mesopolymer Solid Base Catalysts with Variable Basicity: Preparation and Catalytic Properties. J Mater Chem 2009;19:4004–11.

[49] Xing R, Liu N, Liu YM, Wu HW, Jiang YW, Chen L, et al. Novel Solid Acid Catalysts: Sulfonic Acid Group-Functionalized Mesostructured Polymers. Adv Funct Mater 2007;17:2455–61.

[50] Fang L, Xing R, Wu HH, Li XH, Liu YM, Wu P. Clean Synthesis of Biodiesel over Solid Acid Catalysts of Sulfonated Mesopolymers. Sci China Chem 2010;53: 1481–6.

[51] Xing R, Liu YM, Wu HH, Li XH, He MY, Wu P. Preparation of Active and Robust Palladium

[52] Nanoparticle Catalysts Stabilized by Diamine-Functionalized Mesoporous Polymers. Chem Commun 2008:6297–9.

[53] Ramin Ghorbani-Vaghei, Saba Hemmati, Hojat Veisi, Pd immobilized on amidoxime-functionalized Mesoporous SBA-15: A novel and highly active heterogeneous catalyst for Suzuki–Miyaura coupling reactions, J Mol Cat A: Chem, 393, 2014, 240-247.

[54] Fang Y, Huang X-J, Chen P-C, Xu Z-K. Polymer materials for enzyme immobilization and their application in bioreactors. BMB reports. 2011 2011/02//;44(2):87-95.

[55] S.C. Kung, C.C. Chang, W. Fan, M.A. Snyder, Template-Free Ordered Mesoporous Silicas by Binary Nanoparticle Assembly, Langmuir, 2014, 30, 11802–11811.

[56] Muylaert, A. Verberckmoes, J. De Decker, P. Van Der Voort, Ordered mesoporous phenolic resins: highly versatile and ultra-stable support materials, Adv. Colloid Interface Sci., 2012, 175, 39–51.

[57] R. Martin, S.L. Buchwald, Palladium-Catalyzed Suzuki−Miyaura Cross-Coupling Reactions Employing Dialkylbiaryl Phosphine Ligands Accounts, Chem. Res., 2008, 41, 1461–1473.

[58] J. P. Wolfe, R.A. Singer, B.H. Yang, S.L. Buchwald, Highly Active Palladium Catalysts for Suzuki Coupling Reactions, J. Am. Chem. Soc., 1999, 121, 9550–9561.

[59] J. Choma, K. Jedynak, W. Fahrenholz, J. M. Ludwinowicz, Jaroniec, Microporosity development in phenolic resin-based mesoporous carbons for enhancing CO2 adsorption at ambient conditions, Appl. Surf. Sci., 2014, 289, 592–600.

[60] F. Liu, Q. Wu, C. Liu, C. Qi, K. Huang, A. Zheng, S. Dai, Ordered Mesoporous Polymers for Biomass Conversions and Cross-Coupling Reactions, ChemSusChem, 2016, 9, 2496–2504.

[61] K.C. Nicolaou, P.G. Bulger, D. Sarlah, Palladium-catalyzed cross-coupling reactions in total synthesis, Angew. Chemie (International ed. English), 2005, 44, 4442–4489.

[62] Y. Fang, X.J. Huang, P.C. Z.K. Chen, Xu, Polymer materials for enzyme immobilization and their application in bioreactors, BMB Reports, 2011, 44, 87–95.

[63] M.K. Khan, M. Giese, M.Yu, J.A. Kelly, W.Y. Hamad, M. MacLachlan. Flexible Mesoporous Photonic Resins with Tunable Chiral Nematic Structures J, Angew. Chemie Int. Ed., 2013, 52, 8921–8924.

[64] M. Inagaki, M. Toyoda, Y. Soneda, S. Tsujimura and T. Morishita, Templated mesoporous carbons: Synthesis and applications, Carbon, 2016, 107, 448–473.

[65] Y. Jiao, D. Han, Y. Ding, X. Zhang, G. Guo, J. Hu, D. Yang and A. Dong, Fabrication of three-dimensionally interconnected nanoparticle superlattices and their lithium-ion storage properties, Nat. Commun., 2015, 6, 6420.

[66] K. Kailasam, Y.-S. Jun, P. Katekomol, J. D. Epping, W. H. Hong and A. Thomas, Mesoporous Melamine Resins by Soft Templating of Block-co-Polymer Mesophases, Chem. Mater., 2010, 22, 428–434.

[67] S. Tanaka, A. Doi, N. Nakatani, Y. Katayama and Y. Miyake, Synthesis of ordered mesoporous carbon films, powders, and fibers by direct triblock-copolymer-templating method using an ethanol/water system, Carbon , 2009, 47, 2688–2698.

[68] H. Lu, Q. Shi and Z. Huang, pH-Responsive Anionic Wormlike Micelle Based on Sodium Oleate Induced by NaCl, J. Phys. Chem. B, 2014, 118, 12511–12517.

[69] Indra, C. S. Gopinath, S. Bhaduri and G. Kumar Lahiri, Hydroxyapatite supported palladium catalysts for Suzuki–Miyaura cross-coupling reaction in aqueous medium. Catal Sci & Techno, 2013, 3, 1625–1633.

[70] Biffis, P. Centomo, A. Del Zotto and M. Zecca, Pd Metal Catalysts for Cross-Couplings and Related Reactions in the 21st Century: A Critical Review Chem. Rev., 2018, 118, 2249–2295.

[71] F. J. Liu, R. K. Kamat, I. Noshadi, D. Peck, R.S. Parnas, A.M. Zheng, C.Z.Qi, Y. Lin, Depolymerization of crystalline cellulose catalyzed by acidic ionic liquids grafted onto sponge-like nanoporous polymers, Chem. Commun. 2013, 49, 8456.

[72] F.J. Liu, A. M. Zheng, I. Noshadi, F.-S. Xiao, Design and synthesis of hydrophobic and stable mesoporous polymeric solid acid with ultra strong acid strength and excellent catalytic activities for biomass transformation, Appl. Catal. B. 2013, 193, 136–137.

[73] Noshadi , B. Kanjilal B, S. Du , G.M. Bollas ,S.L. Suib, A. Provatas, F. Liu , R.S. Parnas. Catalyzed production of biodiesel and bio-chemicals from brown grease using Ionic Liquid functionalized ordered mesoporous polymer, Applied Energy. 2014, 129, 112–122.

[74] I.Noshadi I, T. Jafari , B. Kanjilal, E. Moharreri, N. Khakpash, A. Masoumi, F. Liu, S.L. Suib. Amine/Thiol functionalized mesoporous polydivinylbenzene for CO2 adsorption Materials Today Energy. 2017, 4, 81–88.

[75] T. Jafari, E. Moharreri, P.Toloueinia, A.S. Amin, S. Sahoo, N. Khakpash, I. Noshadi, A.P. Alpay, S.L. Suib. Microwave-assisted synthesis of amine functionalized mesoporous polydivinylbenzene for CO2 adsorption, Journal of CO2 Utilization. 2017, 19, 79–90.

[76] T. Jin, Z. Xiong, X. Zhu, N. Mehio, Y. Chen, J. Hu, W. Zhang, H. Zou, H. Liu and S. Dai, Facile synthesis of magnetic covalent organic frameworks for the hydrophilic enrichment of N-glycopeptides, ACS Macro Lett., 2015, 4, 570–574.

[77] J. Dupont and M. Pfeffer, Palladacycles: Synthesis, Characterization, and Applications, Wiley Publications, 2014, 4.

[78] Y. Wan, H. Wang, Q. Zhao, M. Klingstedt, O. Terasaki and D. Zhao, Ordered Mesoporous Pd/Silica−Carbon as a Highly Active Heterogeneous Catalyst for Coupling Reaction of Chlorobenzene in Aqueous MediaJ. Am. Chem. Soc., 2009, 131, 4541–4550.

[79] Z. Jin, C. Yu, X. Wang, Y. Wan, D. Li and G. Lu, Liquid phase hydrodechlorination of chlorophenols at lower temperature on a novel Pd catalyst, J. Hazard. Mater., 2011, 186, 1726–1732.

[80] M. Wang, H. Xue, F. Ju and H. Yang, Acceleration of Batch-type Heterogeneous Ligand-free Suzuki-Miyaura Reactions with Polymer Composite Supported Pd Catalyst, Sci. reports, 2017, 7, 7006.

[81] Z. Wu, N. Hao, G. Xiao, L. Liu, P. Webley and D. Zhao, One-pot generation of mesoporous carbon supported nanocrystalline calcium oxides capable of efficient CO2 capture over a wide range of temperatures, Phys. Chem. Chem. Phys. PCCP, 2011, 13, 2495.

[82] Y. Wan, X. Qian, N. Jia, Z. Wang, H. Li and D. Zhao, Direct Triblock-Copolymer-Templating Synthesis of Highly Ordered Fluorinated Mesoporous Carbon, Chem. Mater., 2008, 20, 1012–1018.

[83] O. Yemul and T. Imae, Synthesis and characterization of poly(ethyleneimine) dendrimers, Colloid Polym. Sci., 2008, 286, 747–752.

[84] Zhu L., Dasgupta T., Huang Q., A D-optimal design for estimation of parameters of an exponential-linear growth curve of nanostructures, Technometrics, 2014, 56, 432–442.

[85] L. Zhu, T. Dasgupta and Q. Huang, A physical–statistical model for density control of nanowires, IIE Trans., 2011, 43, 233–241.

[86] T. Dasgupta, B. Weintraub and V. R. Joseph, Palladium PEPPSI complexes: Synthesis and catalytic activity on the Suzuki-Miyaura coupling reactions for aryl bromides at room temperature in aqueous media, Inorganica Chim. Acta, 2018, 478, 187–194.

[87] N. Touj, N. Gürbüz, N. Hamdi, S. Yaşar and İ. Özdemir, The palladium(II) complex of N,N-diethyl-1-ferrocenyl-3-thiabutanamine: synthesis, solution and solid state structure and catalytic activity in Suzuki–Miyaura reaction, RSC Adv., 2014,4, 43792-43799.

[88] M. Opanasenko, P. Stepnicka, J. Cejka., Heterogeneous Pd catalysts supported on silica matrices, RSC Adv., 2014, 4, 65137.

[89] S. Gao, N. Zhao, M. Shu and S. Che, Palladium nanoparticles supported on MOF-5: A highly active catalyst for a ligand- and copper-free Sonogashira coupling reaction, Appl. Catal., A, 2010, 388, 196–201.

[90] V. Polshettiwar, R. Luque, A. Fihri, H. Zhu, M. Bouhrara and J.-M. Bassett, Magnetically Recoverable Nanocatalysts, Chem. Rev., 2011, 111, 3036–3075.

[91] L. Zhang, G. Wen, H. Liu, N. Wang and D. S. Su, Preparation of Palladium Catalysts Supported on Carbon Nanotubes by an Electrostatic Adsorption Method, ChemCatChem, 2014, 6, 2600–2606.

[92] V. Farina, Adv. Synth. High-Turnover Palladium Catalysts in Cross-Coupling and Heck Chemistry: A Critical Overview, Catal., 2004, 346, 1553–1582.

[93] E. Groppo, G. Agostini, E. Borfecchia, L. Wei, F. Giannici, G. Portale, A. Longo and C. Lamberti, Formation and Growth of Pd Nanoparticles Inside a Highly Cross-Linked Polystyrene Support: Role of the Reducing Agent, J. Phys. Chem. C, 2014, 118, 8406–8415.

[94] M. Capka and J. Hetflejs, Hydrosilylation catalysed by transition metal complexes coordinately bound to inorganic supports, Collect. Czech. Chem. Commun., 1974, 39, 154–166.

[95] V. Z. Sharf, A. S. Gurovets, L. P. Finn, I. B. Slinyakova, V. N. Krutii and L. K. Freidlin, Acad. Sci. USSR, Div. Chem. Sci., 1979, 28, 93–96.

[96] R. K. Alan, Advances in Heterocyclic Chemistry, ed. Academic Press, 2013, 326.

[97] Tamami, F. Farjadian, S. Ghasemi and H. Allahyari, Synthesis and applications of polymeric N-heterocyclic carbene palladium complex-grafted silica as a novel recyclable nano-catalyst for Heck and Sonogashira coupling reactions, New J. Chem., 2013, 37, 2011–2018.

[98] S. Paul and J. H. Clark, Structure-activity relationship between some novel silica supported palladium catalysts: a study of the Suzuki reaction, Mol. Catal. A: Chem., 2004, 215, 107–111.

[99] O. Vassylyev, J. Chen, A. P. Panarello and J. G. Khinast, Catalytic properties of several supported Pd(II) complexes for Suzuki coupling reactions, Tetrahedron Lett., 2005, 46, 6865–6869.

[100] S.C. Kung, C.C. Chang, W. Fan, M.A. Snyder, Template-Free Ordered Mesoporous Silicas by Binary Nanoparticle Assembly, Langmuir, 2014, 30, 11802–11811.

[101] Muylaert, A. Verberckmoes, J. De Decker, P. Van Der Voort, Ordered mesoporous phenolic resins: highly versatile and ultra-stable support materials, Adv. Colloid Interface Sci., 2012, 175, 39–51.

[102] R. Martin, S.L. Buchwald, Palladium-Catalyzed Suzuki−Miyaura Cross-Coupling Reactions Employing Dialkylbiaryl Phosphine Ligands Accounts, Chem. Res., 2008, 41, 1461–1473.

[103] J. P. Wolfe, R.A. Singer, B.H. Yang, S.L. Buchwald, Highly Active Palladium Catalysts for Suzuki Coupling Reactions, J. Am. Chem. Soc., 1999, 121, 9550–9561.

[104] J. Choma, K. Jedynak, W. Fahrenholz, J. M. Ludwinowicz, Jaroniec, Microporosity development in phenolic resin-based mesoporous carbons for enhancing CO2 adsorption at ambient conditions, Appl. Surf. Sci., 2014, 289, 592–600.

[105] K. Kailasam, Y.-S. Jun, P. Katekomol, J. D. Epping, W. H. Hong and A. Thomas, Mesoporous Melamine Resins by Soft Templating of Block-co-Polymer Mesophases, Chem. Mater., 2010, 22, 428–434.

[106] S. Tanaka, A. Doi, N. Nakatani, Y. Katayama and Y. Miyake, Synthesis of ordered mesoporous carbon films, powders, and fibers by direct triblock-copolymer-templating method using an ethanol/water system, Carbon , 2009, 47, 2688–2698.

[107] H. Lu, Q. Shi and Z. Huang, pH-Responsive Anionic Wormlike Micelle Based on Sodium Oleate Induced by NaCl, J. Phys. Chem. B, 2014, 118, 12511–12517.

[108] Indra, C. S. Gopinath, S. Bhaduri and G. Kumar Lahiri, Hydroxyapatite supported palladium catalysts for Suzuki–Miyaura cross-coupling reaction in aqueous medium. Catal Sci & Techno, 2013, 3, 1625–1633.

[109] Biffis, P. Centomo, A. Del Zotto and M. Zecca, Pd Metal Catalysts for Cross-Couplings and Related Reactions in the 21st Century: A Critical Review Chem. Rev., 2018, 118, 2249–2295.

[110] F. J. Liu, R. K. Kamat, I. Noshadi, D. Peck, R.S. Parnas, A.M. Zheng, C.Z.Qi, Y. Lin, Depolymerization of crystalline cellulose catalyzed by acidic ionic liquids grafted onto sponge-like nanoporous polymers, Chem. Commun. 2013, 49, 8456.

[111] F.J. Liu, A. M. Zheng, I. Noshadi, F.-S. Xiao, Design and synthesis of hydrophobic and stable mesoporous polymeric solid acid with ultra strong acid strength and excellent catalytic activities for biomass transformation, Appl. Catal. B. 2013, 193, 136–137.

[112] Noshadi , B. Kanjilal B, S. Du , G.M. Bollas ,S.L. Suib, A. Provatas, F. Liu , R.S. Parnas. Catalyzed production of biodiesel and bio-chemicals from brown grease using Ionic Liquid functionalized ordered mesoporous polymer, Applied Energy. 2014, 129, 112–122.

[113] I.Noshadi I, T. Jafari , B. Kanjilal, E. Moharreri, N. Khakpash, A. Masoumi, F. Liu, S.L. Suib. Amine/Thiol functionalized mesoporous polydivinylbenzene for CO2 adsorption Materials Today Energy. 2017, 4, 81–88.

[114] T. Jafari, E. Moharreri, P.Toloueinia, A.S. Amin, S. Sahoo, N. Khakpash, I. Noshadi, A.P. Alpay, S.L. Suib. Microwave-assisted synthesis of amine functionalized mesoporous polydivinylbenzene for CO2 adsorption, Journal of CO2 Utilization. 2017, 19, 79–90.

[115] T. Jin, Z. Xiong, X. Zhu, N. Mehio, Y. Chen, J. Hu, W. Zhang, H. Zou, H. Liu and S. Dai, Facile synthesis of magnetic covalent organic frameworks for the hydrophilic enrichment of N-glycopeptides, ACS Macro Lett., 2015, 4, 570–574.

[116] J. Dupont and M. Pfeffer, Palladacycles: Synthesis, Characterization, and Applications, Wiley Publications, 2014, 4.

[117] Y. Wan, H. Wang, Q. Zhao, M. Klingstedt, O. Terasaki and D. Zhao, Ordered Mesoporous Pd/Silica−Carbon as a Highly Active Heterogeneous Catalyst for

Coupling Reaction of Chlorobenzene in Aqueous MediaJ. Am. Chem. Soc., 2009, 131, 4541–4550.

[118] Z. Jin, C. Yu, X. Wang, Y. Wan, D. Li and G. Lu, Liquid phase hydrodechlorination of chlorophenols at lower temperature on a novel Pd catalyst, J. Hazard. Mater., 2011, 186, 1726–1732.

[119] M. Wang, H. Xue, F. Ju and H. Yang, Acceleration of Batch-type Heterogeneous Ligand-free Suzuki-Miyaura Reactions with Polymer Composite Supported Pd Catalyst, Sci. reports, 2017, 7, 7006.

[120] Z. Wu, N. Hao, G. Xiao, L. Liu, P. Webley and D. Zhao, One-pot generation of mesoporous carbon supported nanocrystalline calcium oxides capable of efficient CO2 capture over a wide range of temperatures, Phys. Chem. Chem. Phys. PCCP, 2011, 13, 2495.

[121] Y. Wan, X. Qian, N. Jia, Z. Wang, H. Li and D. Zhao, Direct Triblock-Copolymer-Templating Synthesis of Highly Ordered Fluorinated Mesoporous Carbon, Chem. Mater., 2008, 20, 1012–1018.

[122] O. Yemul and T. Imae, Synthesis and characterization of poly(ethyleneimine) dendrimers, Colloid Polym. Sci., 2008, 286, 747–752.

[123] Zhu L., Dasgupta T., Huang Q., A D-optimal design for estimation of parameters of an exponential-linear growth curve of nanostructures, Technometrics, 2014, 56, 432–442.

[124] L. Zhu, T. Dasgupta and Q. Huang, A physical–statistical model for density control of nanowires, IIE Trans., 2011, 43, 233–241.

[125] T. Dasgupta, B. Weintraub and V. R. Joseph, Palladium PEPPSI complexes: Synthesis and catalytic activity on the Suzuki-Miyaura coupling reactions for aryl bromides at room temperature in aqueous media, Inorganica Chim. Acta, 2018, 478, 187–194.

[126] N. Touj, N. Gürbüz, N. Hamdi, S. Yaşar and İ. Özdemir, The palladium(II) complex of N,N-diethyl-1-ferrocenyl-3-thiabutanamine: synthesis, solution and solid state structure and catalytic activity in Suzuki–Miyaura reaction, RSC Adv., 2014,4, 43792-43799.

[127] M. Opanasenko, P. Stepnicka, J. Cejka., Heterogeneous Pd catalysts supported on silica matrices, RSC Adv., 2014, 4, 65137.

[128] S. Gao, N. Zhao, M. Shu and S. Che, Palladium nanoparticles supported on MOF-5: A highly active catalyst for a ligand- and copper-free Sonogashira coupling reaction, Appl. Catal., A, 2010, 388, 196–201.

[129] V. Polshettiwar, R. Luque, A. Fihri, H. Zhu, M. Bouhrara and J.-M. Bassett, Magnetically Recoverable Nanocatalysts, Chem. Rev., 2011, 111, 3036–3075.

[130] L. Zhang, G. Wen, H. Liu, N. Wang and D. S. Su, Preparation of Palladium Catalysts Supported on Carbon Nanotubes by an Electrostatic Adsorption Method, ChemCatChem, 2014, 6, 2600–2606.

[131] V. Farina, Adv. Synth. High-Turnover Palladium Catalysts in Cross-Coupling and Heck Chemistry: A Critical Overview, Catal., 2004, 346, 1553–1582.

[132] E. Groppo, G. Agostini, E. Borfecchia, L. Wei, F. Giannici, G. Portale, A. Longo and C. Lamberti, Formation and Growth of Pd Nanoparticles Inside a Highly Cross-Linked Polystyrene Support: Role of the Reducing Agent, J. Phys. Chem. C, 2014, 118, 8406–8415.

[133] M. Capka and J. Hetflejs, Hydrosilylation catalysed by transition metal complexes coordinately bound to inorganic supports, Collect. Czech. Chem. Commun., 1974, 39, 154–166.

[134] V. Z. Sharf, A. S. Gurovets, L. P. Finn, I. B. Slinyakova, V. N. Krutii and L. K. Freidlin, Acad. Sci. USSR, Div. Chem. Sci., 1979, 28, 93–96.

[135] R. K. Alan, Advances in Heterocyclic Chemistry, ed. Academic Press, 2013, 326.

[136] Tamami, F. Farjadian, S. Ghasemi and H. Allahyari, Synthesis and applications of polymeric N-heterocyclic carbene palladium complex-grafted silica as a novel recyclable nano-catalyst for Heck and Sonogashira coupling reactions, New J. Chem., 2013, 37, 2011–2018.

[137] S. Paul and J. H. Clark, Structure-activity relationship between some novel silica supported palladium catalysts: a study of the Suzuki reaction, Mol. Catal. A: Chem., 2004, 215, 107–111.

[138] O. Vassylyev, J. Chen, A. P. Panarello and J. G. Khinast, Catalytic properties of several supported Pd(II) complexes for Suzuki coupling reactions, Tetrahedron Lett., 2005, 46, 6865–6869.

[139] R. Najman, J. K. Cho, A. F. Coffey, J. W. Davies and M. Bradley, Entangled palladium nanoparticles in resin plugs, 44Chem. Commun., 2007, 5031–3.

[140] J. Li, J. Yu, J. Zhao, J. Wang, S. Zheng, S. Lin, L. Chen, M. Yang, S. Jia, X. Zhang and P. R. Chen, Palladium-triggered deprotection chemistry for protein activation in living cells, Nat. Chem., 2014, 6, 352–361.

[141] Bonnier, D. D. Machin, O. Abdi and B. D. Koivisto, Manipulating non-innocent π-spacers: the challenges of using 2,6-disubstituted BODIPY cores within donor–acceptor light-harvesting motifs, Org. Biomol. Chem., 2013, 11, 3756–3760.

[142] Wang F, Zhang Y, Du Z, Ren J, Qu X, Designed heterogeneous palladium catalysts for reversible light-controlled bioorthogonal catalysis in living cells, Nature Communications, 2018, 9 (1) 1209- 1217.

[143] T.H. Oh, Carbon capture and storage potential in coal-fired plant in Malaysia—A review, Renew. Sustain. Energy Rev. 14 (2010) 2697–2709.

[144] X. Liu, L. Zhu, H. Wang, G. He, Z. Bian, Catalysis performance comparison for electrochemical reduction of CO 2 on Pd–Cu/graphene catalyst, RSC Adv. 6 (2016) 38380–38387.

[145] J.W. Maina, C. Pozo-Gonzalo, L. Kong, J. rg Schü tz, M. Hill, L.F. Dumé, Metal organic framework based catalysts for CO 2 conversion, 4 (2017) 345.

[146] P.R. Yaashikaa, P. Senthil Kumar, S.J. Varjani, A. Saravanan, A review on photochemical, biochemical and electrochemical transformation of CO2 into value-added products, J. CO2 Util. 33 (2019) 131–147.

[147] C.S. Chen, A.D. Handoko, J.H. Wan, L. Ma, D. Ren, S. Yeo, Stable and Selective Electrochemical Reduction of Carbon Dioxide to Ethylene on Copper Mesocrystals ARTICLE TYPE Stable and Selective Electrochemical Reduction of Carbon Dioxide to Ethylene on Copper Mesocrystals Catal. Sci. Technol., 2015,5, 161-168

[148] Zhao, J. Wang, Electrochemical reduction of CO2 to formate in aqueous solution using electro-deposited Sn catalysts, Chem. Eng. J. 293 (2016) 161–170.

[149] T. Zhang, X. Li, Y. Qiu, P. Su, W. Xu, H. Zhong, H. Zhang, Multilayered Zn nanosheets as an electrocatalyst for efficient electrochemical reduction of CO2, J. Catal. 357 (2018) 154–162.

[150] N. Han, Y. Wang, L. Ma, J. Wen, J. Li, H. Zheng, K. Nie, X. Wang, F. Zhao, Y. Li, J. Fan, J. Zhong, T. Wu, D.J. Miller, J. Lu, S.-T. Lee, Y. Li, Supported Cobalt Polyphthalocyanine for High-Performance Electrocatalytic CO2 Reduction, Chem. 3 (2017) 652–664.

[151] Q. Tang, Y. Wang, J. Zhang, R. Qiao, X. Xie, Y. Wang, Y. Yang, Cobalt(II) acetylacetonate complex immobilized on aminosilane-modified SBA-15 as an efficient catalyst for epoxidation of trans -stilbene with molecular oxygen, Appl. Organomet. Chem. 30 (2016) 435–440.

[152] X.-M. Hu, H.H. Hval, E.T. Bjerglund, K.J. Dalgaard, M.R. Madsen, M.-M. Pohl, E. Welter, P. Lamagni, K.B. Buhl, M. Bremholm, M. Beller, S.U. Pedersen, T. Skrydstrup, K. Daasbjerg, Selective CO2 Reduction to CO in Water using Earth-Abundant Metal and Nitrogen-Doped Carbon Electrocatalysts, ACS Catal. 8 (2018) 6255–6264.

[153] J. Yu, M. Guo, F. Muhammad, A. Wang, F. Zhang, Q. Li, G. Zhu, One-pot synthesis of highly ordered nitrogen-containing mesoporous carbon with resorcinol–urea–formaldehyde resin for CO2 capture, Carbon N. Y. 69 (2014) 502–514.

[154] Z. Chen, S. Deng, H. Wei, B. Wang, J. Huang, G. Yu, Polyethylenimine-Impregnated Resin for High CO2 Adsorption: An Efficient Adsorbent for CO2 Capture from Simulated Flue Gas and Ambient Air, (2013).

[155] T. Ma, Q. Fan, X. Li, J. Qiu, T. Wu, Z. Sun, Graphene-based materials for electrochemical CO2 reduction, J. CO2 Util. 30 (2019) 168–182.

[156] G. Sethia, A. Sayari, Comprehensive study of ultra-microporous nitrogen-doped activated carbon for CO2 capture, Carbon N. Y. 93 (2015) 68–80.

[157] Z. Liu, Z. Du, H. Song, C. Wang, F. Subhan, W. Xing, Z. Yan, The fabrication of porous N-doped carbon from widely available urea formaldehyde resin for carbon dioxide adsorption, J. Colloid Interface Sci. 416 (2014) 124–132.

[158] Liu, K. Huang, Q. Wu, S. Dai, Solvent-Free Self-Assembly to the Synthesis of Nitrogen-Doped Ordered Mesoporous Polymers for Highly Selective Capture and Conversion of CO 2, Adv. Mater. 29 (2017) 1700445.

[159] E.T. Thostenson, W.Z. Li, D.Z. Wang, Z.F. Ren, T.W. Chou, Carbon nanotube/carbon fiber hybrid multiscale composites, J. Appl. Phys. 91 (2002) 6034–6037.

[160] Y.-C. Chiang, W.-L. Hsu, S.-Y. Lin, R.-S. Juang, Enhanced CO_2 Adsorption on Activated Carbon Fibers Grafted with Nitrogen-Doped Carbon Nanotubes., Mater. (Basel, Switzerland). 10 (2017).

[161] M. Razmkhah, M.T.H. Mosavian, F. Moosavi, A. Ahmadpour, CO2 gas adsorption into graphene oxide framework: Effect of electric and magnetic field, Appl. Surf. Sci. 456 (2018) 318–327.

[162] Y. Zhang, Y. Chi, C. Zhao, Y. Liu, Y. Zhao, L. Jiang, Y. Song, CO2 Adsorption Behavior of Graphite Oxide Modified with Tetraethylenepentamine, (2017).

[163] K. Christian Kemp, V. Chandra, M. Saleh, K.S. Kim, Reversible CO2 adsorption by an activated nitrogen doped graphene/polyaniline material, Nanotechnology. 24 (2013) 235703.

[164] H. Ju, G. Kaur, A.P. Kulkarni, S. Giddey, Challenges and trends in developing technology for electrochemically reducing CO2 in solid polymer electrolyte membrane reactors, J. CO2 Util. 32 (2019) 178–186.

[165] A.A. Olajire, Recent progress on the nanoparticles-assisted greenhouse carbon dioxide conversion processes, J. CO2 Util. 24 (2018) 522–547.

[166] Y. Sun, K. Li, J. Zhao, J. Wang, N. Tang, D. Zhang, T. Guan, Z. Jin, Nitrogen and sulfur Co-doped microporous activated carbon macro-spheres for CO2 capture, J. Colloid Interface Sci. 526 (2018) 174–183.

[167] Z. Jin, J. Wang, R. Zhao, T. Guan, D. Zhang, K. Li, Synthesis of S, N co-doped porous carbons from polybenzoxazine for CO2 capture, New Carbon Mater. 33 (2018) 392–401.

[168] Liu, K. Huang, C.J. Yoo, C. Okonkwo, D.J. Tao, C.W. Jones, S. Dai, Facilely synthesized meso-macroporous polymer as support of poly(ethyleneimine) for highly efficient and selective capture of CO2, Chem. Eng. J. (2017).

[169] Z. Chen, S. Deng, H. Wei, B. Wang, J. Huang, G. Yu, Polyethylenimine-Impregnated Resin for High CO 2 Adsorption: An Efficient Adsorbent for CO 2 Capture from Simulated Flue Gas and Ambient Air, ACS Appl. Mater. Interfaces. 5 (2013) 6937–6945.

[170] P. Li, B. Ge, S. Zhang, S. Chen, Q. Zhang, Y. Zhao, CO2 Capture by Polyethylenimine-Modified Fibrous Adsorbent, (2008).

[171] X. Yan, L. Zhang, Y. Zhang, K. Qiao, Z. Yan, S. Komarneni, Amine-modified mesocellular silica foams for CO2 capture, Chem. Eng. J. 168 (2011) 918–924.

[172] D.J.N. Subagyono, M. Marshall, G.P. Knowles, A.L. Chaffee, CO2 adsorption by amine modified siliceous mesostructured cellular foam (MCF) in humidified gas, Microporous Mesoporous Mater. 186 (2014) 84–93.

[173] M.L. Gray, J.S. Hoffman, D.C. Hreha, D.J. Fauth, S.W. Hedges, K.J. Champagne, H.W. Pennline, Parametric Study of Solid Amine Sorbents for the Capture of Carbon Dioxide †, Energy & Fuels. 23 (2009) 4840–4844.

[174] M.A. Sakwa-Novak, C.-J. Yoo, S. Tan, F. Rashidi, C.W. Jones, Poly(ethylenimine)-Functionalized Monolithic Alumina Honeycomb Adsorbents for CO2 Capture from Air, ChemSusChem. 9 (2016) 1859–1868.

[175] Dindi, D.V. Quang, E. Nashef, M.R.M.A. Zahra, Effect of PEI Impregnation on the CO2 Capture Performance of Activated Fly Ash, Energy Procedia. 114 (2017) 2243–2251.

[176] J. Wang, L. Yao, C. Ma, X. Guo, W. Qiao, L. Ling, D. Long, Organic Amine-Mediated Synthesis of Polymer and Carbon Microspheres: Mechanism Insight and Energy-Related Applications, ACS Appl. Mater. Interfaces. 8 (2016) 4851–4861.

[177] Kyungmin Min, Woosung Choi, Chaehoon Kim, and Minkee Choi, Oxidation-stable amine-containing adsorbents for carbon dioxide capture, Nat Commun. 2018; 9: 726.,

[178] Liyan Huang , Yi Shi , Liusheng Chen, Xigao Jin, Ronghua Liu, Mitchell A. Winnik, David Mitchell, Thermal decomposition of amide and imide derivatives of maleated polyethylene,

[179] Ute Krämer, Janet D. Cotter-Howells, John M. Charnock, Alan J. M. Baker & J. Andrew C. Smith , Free histidine as a metal chelator in plants that accumulate nickel, Nature , volume 379, pages, 635–638 (1996)

[180] Seraphine V. Wegner, Joachim P. Spatz, Angew. Cobalt(III) as a Stable and Inert Mediator Ion between NTA and His6‐Tagged Proteins, Chem. Int. Ed., 2013, 52, 7593 –7596)

[181] V. Z. Sharf, A. S. Gurovets, L. P. Finn, I. B. Slinyakova, V. N. Krutii and L. K. Freidlin, Acad. Sci. USSR, Div. Chem. Sci., 1979, 28, 93–96.

[182] R. K. Alan, Advances in Heterocyclic Chemistry, ed. Academic Press, 2013, 326.

[183] Tamami, F. Farjadian, S. Ghasemi and H. Allahyari, Synthesis and applications of polymeric N-heterocyclic carbene palladium complex-grafted silica as a novel recyclable nano-catalyst for Heck and Sonogashira coupling reactions, New J. Chem., 2013, 37, 2011–2018.

[184] S. Paul and J. H. Clark, Structure-activity relationship between some novel silica supported palladium catalysts: a study of the Suzuki reaction, Mol. Catal. A: Chem., 2004, 215, 107–111.

[185] O. Vassylyev, J. Chen, A. P. Panarello and J. G. Khinast, Catalytic properties of several supported Pd(II) complexes for Suzuki coupling reactions, Tetrahedron Lett., 2005, 46, 6865–6869.

[186] R. Najman, J. K. Cho, A. F. Coffey, J. W. Davies and M. Bradley, Entangled palladium nanoparticles in resin plugs, 44Chem. Commun., 2007, 5031–3.

[187] J. Li, J. Yu, J. Zhao, J. Wang, S. Zheng, S. Lin, L. Chen, M. Yang, S. Jia, X. Zhang and P. R. Chen, Palladium-triggered deprotection chemistry for protein activation in living cells, Nat. Chem., 2014, 6, 352–361.

[188] Bonnier, D. D. Machin, O. Abdi and B. D. Koivisto, Manipulating non-innocent π-spacers: the challenges of using 2,6-disubstituted BODIPY cores within donor–acceptor light-harvesting motifs, Org. Biomol. Chem., 2013, 11, 3756–3760.

[189] Wang F, Zhang Y, Du Z, Ren J, Qu X, Designed heterogeneous palladium catalysts for reversible light-controlled bioorthogonal catalysis in living cells, Nature Communications, 2018, 9 (1) 1209- 1217.

Appendix A

Solvent- Free Synthesis of Ordered Mesoporous Polymeric Resins as a Catalyst

Efficacious application of ordered mesoporous resin (OMR) is dependent on the design and controlled fabrication. In this work, uniform OMR was synthesized by straightforward, low cost, and two-step procedures. The soft-template method overcomes a major drawback of the hard-template method. Besides, this solvent-free procedure can overcome the weak self-assembly ability of precursor components during a hydrothermal process. For this purpose, resorcinol, terephthaldehyde, and sodium isotonic acid (precursors) were grounded with F127 to create a soft paste. This paste was baked for 24 hours at 140 ºC, and then calcination process was used at 360 ºC for removing the template. The effects of template concentration (0.5, 1, 1.5, 2 g template for the same amount of precursors) and temperature calcination ramp (0.5, 1, 1.5 ºC/min) on OMR structure were examined. Surface area measurements were gathered by BET, and the results confirmed a polynomial relation between template concentration and surface area. The maximum BET surface area 786.264 m^2/g for using 1 g of the template. The SEM results showed that the hexagonal mesoporous structure was uniform. Furthermore, this OMR can be successfully synthesized in a solid phase with two stages, and ease of functionalization emanates tremendous application of it for catalyst application. Therefore, OMR was functionalized with Chlorosulfonic acid and used as a biomass conversion heterogeneous catalyst. Also, palladium acetate was grounded with solid raw precursors and used for a cross-coupling reaction after calcination. High BET surface area (662.66 m^2/g for using 1 gr of template/0.46 g resorcinol and 1% palladium acetate (w/w)) and high thermal stability (TG more than 450 ºC) made it a great heterogeneous catalyst for 98% conversion up to 5 cycles.

This synthesis strategy provides a benchmark for fabricating well-defined ordered mesoporous structures with potential for catalyst applications.

1 Introduction

Ordered mesoporous resin (OMR) plays a vital role as a heterogeneous catalyst in the pharmaceutical industry to produce drugs. In this work, we produce a new OMR catalyst based on a solvent-free procedure. The main advantage of this procedure is minimizing environmental impact by removing solvent and synthesis in the solid mixing phase. Also, the temperature of calcination and the rate are mild, then the required energy decreases. This resin has high thermal stability and easy functional ability. Multi applications of this OMR as a catalyst is encluded acid group such as SO_3H, SO_3CF_3, or metal such as platinum and palladium.

2 Materials and Methods

Pluronic F-127, Resorcinol, Terephthalaldehyde, and Isotonic acid sodium, and Hexamethylenediamine (HMTA) were purchased from Alfa- Acer and used without any further purification. Two versions of OMRs have been made in solid-phase, just only powder of various amounts of F-127, Resorcinol, Terephthalaldehyde, and Isotonic acid sodium, and Hexamethylenediamine (HMTA) were grounded and baked in an oven at 140 °C for 24 hours. Then, calcination was done at 350 °C for 2 hours. In this work, uniform OMR was synthesized by straightforward, low cost, and with two-step procedures of the soft-template method, which overcame a significant drawback of the hard-template method and using the organic solvent. The effect of template concentration (0.5, 1, 1.5, 2 g template for the same amount of precursors) and temperature calcination ramp (0.5, 1, 1.5 ºC/min) on the OMR structure was examined. OMR pore size was independent of composition and

ramp rate calcination stage. One variation of the catalyst has been doped with a small percentage of Palladium Acetate so that Cross-Coupling Reactions have been run on this specific sample.

3 Results

3.1 Maximizing Surface Area of OMR

Surface area measurements were gathered by BET, and the results confirmed a polynomial relation between template concentration and surface area. The maximum BET surface area 786.264 m^2/g for using 1g of the template. The data was shown in figure A1. It is interesting, OMR pore size was completely independent of composition and ramp rate calcination stage. However, the surface is a function of them. HMTA discompose to formaldehyde and ammonia. Ammonia plays as a catalyst to expedite the reaction between phenol and formaldehyde, causing reducing the time of micelles formation. Therefore, the

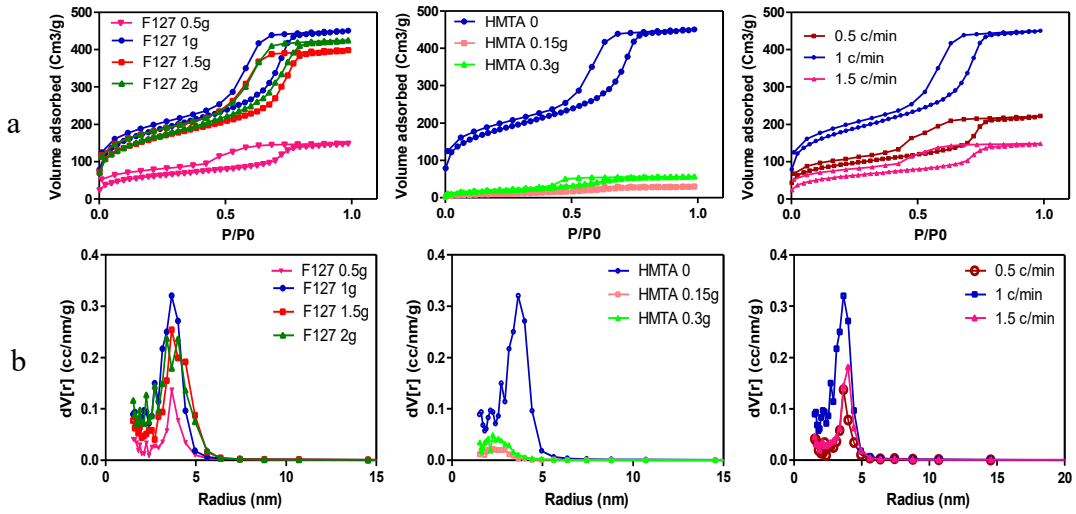

Figure A1. a Nitrogen adsorption–desorption isotherms, b. Pore size distribution based on BJH model of OMR with various composition and calcination condition.

surface area of OMR decreases by increasing the concentration of HMTA.

3.2 Acid Functionalization OMR and OMR-H (OMR-HSO_3 and OMR-H-HSO_3)

For acid functionalization catalyst, after the calcination stage, OMR was grounded and then the chlorosulfuric acid solution in toluene at ice bath. After 24 hours, the catalyst washed adequately with water to remove unreacted acid. Figure A2-a showed the functionalized catalyst surface area. FTIR spectra of OMR-HSO_3 and OMR-H-HSO_3 were illustrated in Figure A2-b, a peak at approximately 1042, and 1180 cm^{-1} associated with the C-S and S=O bonds can be clearly observed, indicating successful grafting of a sulfonic group in the sample.

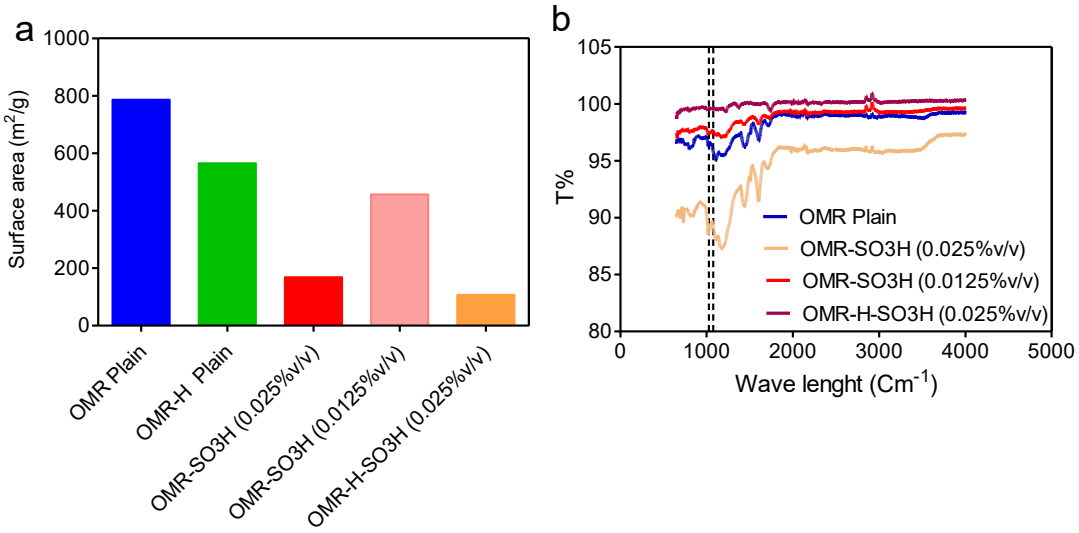

Figure A2. (a). Surface area (b). FTIR spectra of various acid functionalized OMR (c) Conversion rate of esterification of oleic acid

3.3 Palladium Doped OMR (Pd-OMR)

Also, palladium acetate was grounded with solid raw precursors and used for cross-coupling reaction after calcination. High BET surface area (662.66 m^2/g for using 1 gr of template/0.46 gr resorcinol and 1% palladium acetate (w/w)) and by increasing the concentration of palladium to 2% (w/w) as illustrated in figure A3-a. Increasing palladium decreased pore size diameter (figure A3-b).

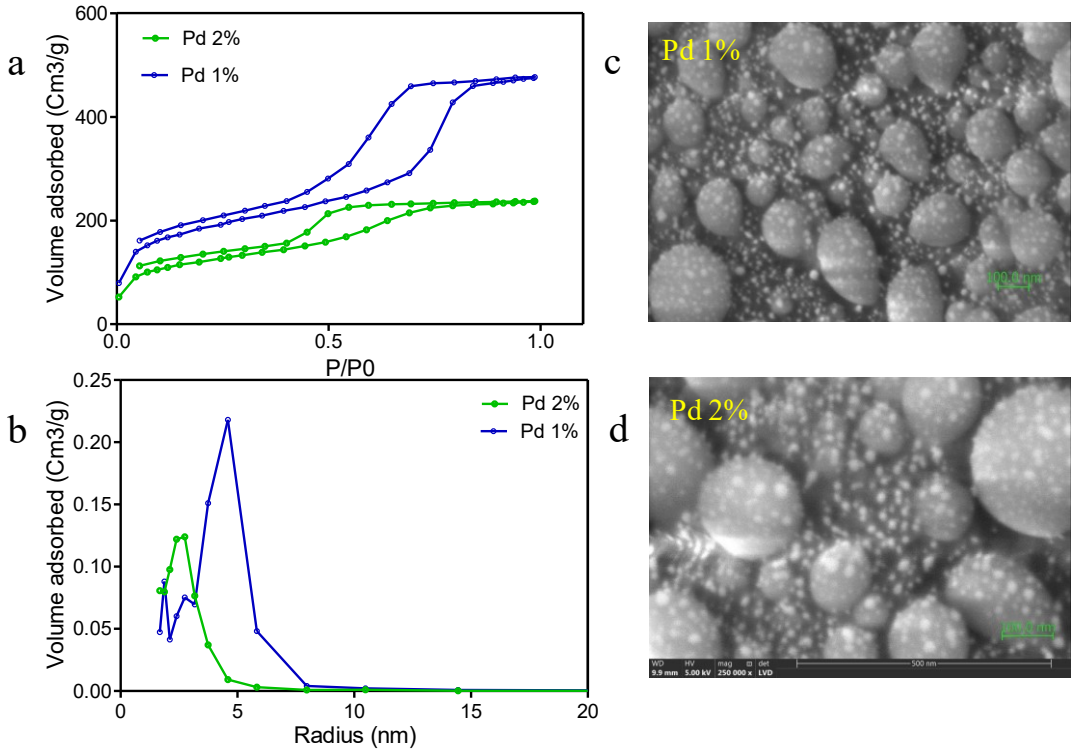

Figure A3. OMR Palladium characterization (a) Nitrogen adsorption isotherm (b) size distribution, (c-d) SEM images

3.4 Catalytic Application

3.4.1 Esterification Reaction. Esterification of oleic acid with methanol, which is a proper model reaction to produce biodiesel from raw feedstocks. Therefore 1.0 g of oleic acid was mixed with 10 mL of methanol and 10 mg of acid-functionalized catalyst in a three-neck round flask equipped with a condenser and a magnetic stirrer. The reaction was performed at 110 °C for five hours. As shown in Figure A4, the conversion rate reached to maximum after 3 hours. Then the reusability of catalyst was considered. OMR-H-HSO_3 was showed (Figure A4-b) higher conversion rate and more stability.

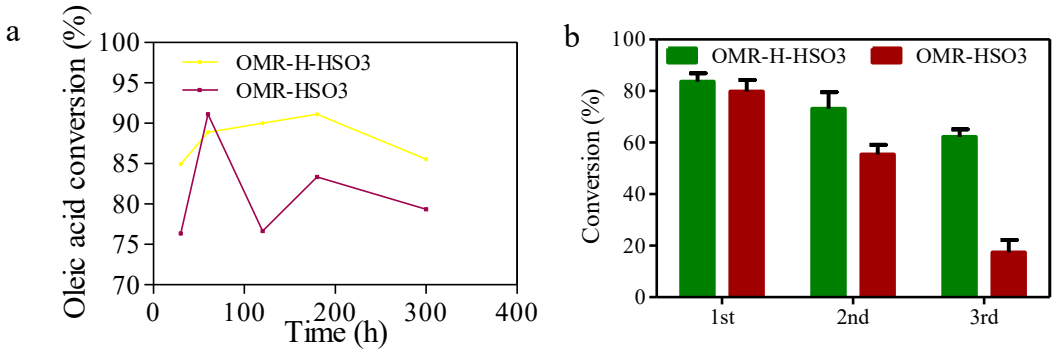

Figure A4. (a). Conversion rate of esterification of oleic acid during time (b) Reusability of the acid functionalized catalyst

3.4.2 Suzuki- Miyaura Reaction

In a typical run for the Suzuki–Miyaura reaction, 0.25 mmol of 4-iodotoluene, 0.375 mmol of aryl boronic acids, and 0.5 mmol of potassium carbonate were mixed well in a flask, followed by the addition of 10 mg of OMR-Pd 1% or 2%, 3.0 mL of ethanol and

1.0 mL of deionized water were used as the solvents. The reaction was performed at 80 °C for 30 min. Figure A5-a and b showed the conversion rate of this reaction based on GC analysis. As shown, both of the catalysts have the highest conversion rate after 45 min. Also, the catalyst conversion rate is almost constant during cycles. Then these catalysts were evaluated to couple bromotoluen and aryl boronic acid. The same container which was contained 1.0 mmol of 4-bromotoluene, 3.0 mmol of aryl boronic acids, and 2.0 mmol of potassium carbonate were mixed with 40 mg of the catalyst. Dimethylformamide (DMF) was mixed with water by the ratio of 3 to 1used as a solvent. The reaction temperature was kept at 110 °C for 5 hr. The maximum conversion rate was after 3 hours, and this time was used for the reusability of catalysts.

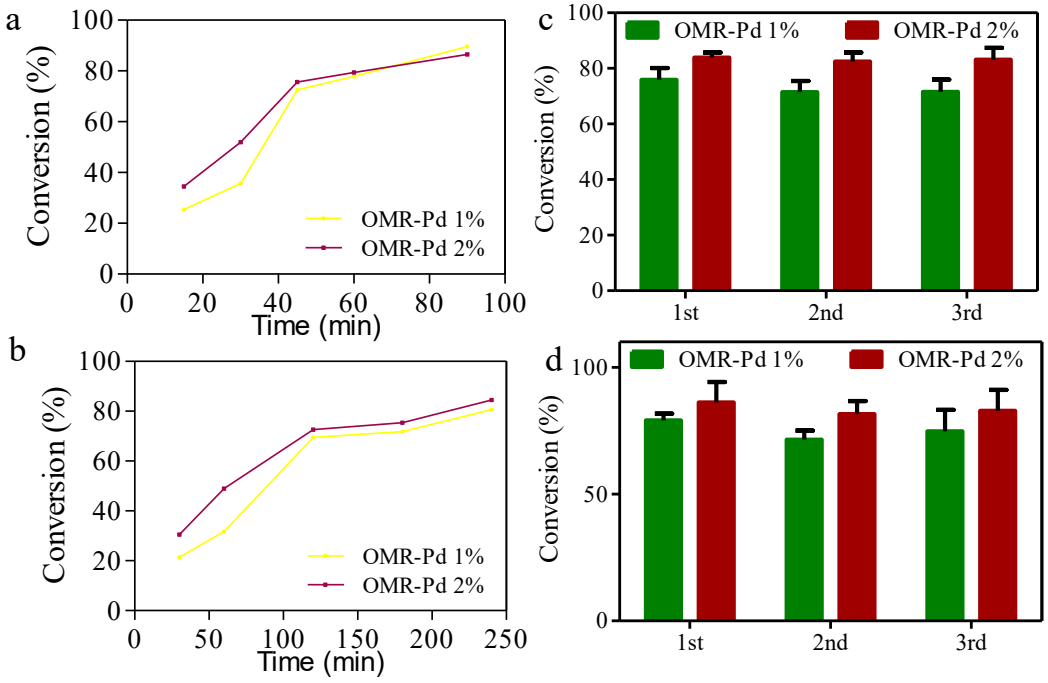

Figure A5. Conversion rate of (a) Suzuki cross coupling reaction 4-Iodotoluen (b) Suzuki cross coupling reaction 4-Bromotoluen

4 Discussion

Fig. A1-a show N_2 adsorption/desorption isotherms based on Brunauer– Emmett–Teller (BET) surface areas for the various concentration of template (F127) calcined at 360 ºC for two hours. Consequently, Pore size distribution (based on BJH model) of these samples illustrated in Fig. A4-b. These samples exhibit type-IV curves with a sharp capillary condensation step at P/P0 0.5–0.75 (Fig. 27-a, H2-type hysteresis loop), which is characteristic of a 3D caged mesostructured. Interestingly, template concentration does not have linear effects on surface area and pore size distributions based on BJH model. BET surface area of OMR-F0.5, OMR-F1, OMR-F1.5, and OMR-F2 are 219.754, 786.264, 566.192, and 590.807 m^2/gr, respectively. The change in BET surface area for these samples is mainly attributed to the difference in microporosity. For example, the microporous surface area of OMR-F0.5, OMR-F1, and OMR-1.5 is 360 and 112 m^2/g, respectively.

Generally, due to the strong hydrogen bond between F-127 and preformed resol, the F-127 groups will be embedded into the resin during the polymerization. The microporosity in the samples has resulted from the removal of F-127 block in the resin walls [185-190]. The more significant microporosity might suggest the stronger interaction between F-127 block with performed resol in the sample.

5 Conclusion

OMR catalyst successfully synthesized in a solid phase with two stages, and ease of functionalization emanates broad application. Therefore, OMR was functionalized with Cchlorosulfuric acid and used as a biomass conversion heterogeneous catalyst. The results showed in Figure A2, which confirmed the high efficiency of the OMR-HSO_3 catalyst for

esterification. Also, palladium acetate was grounded with solid raw precursors and used for cross-coupling reaction after calcination. High BET surface area (662.66 m^2/g for using 1 gr of template/0.46 g resorcinol and 1% palladium acetate (w/w)) and proper thermal stability (TG more than 450 ºC) made it a great heterogeneous catalyst for 98% conversion up to 5 cycles. This method offers a benchmark to fabricate a well-defined ordered mesoporous structure with the potential for catalyst applications.

Appendix B

Additional Data

EDS elemental analysis of RFs was illustrated in Figure S1 and S2.

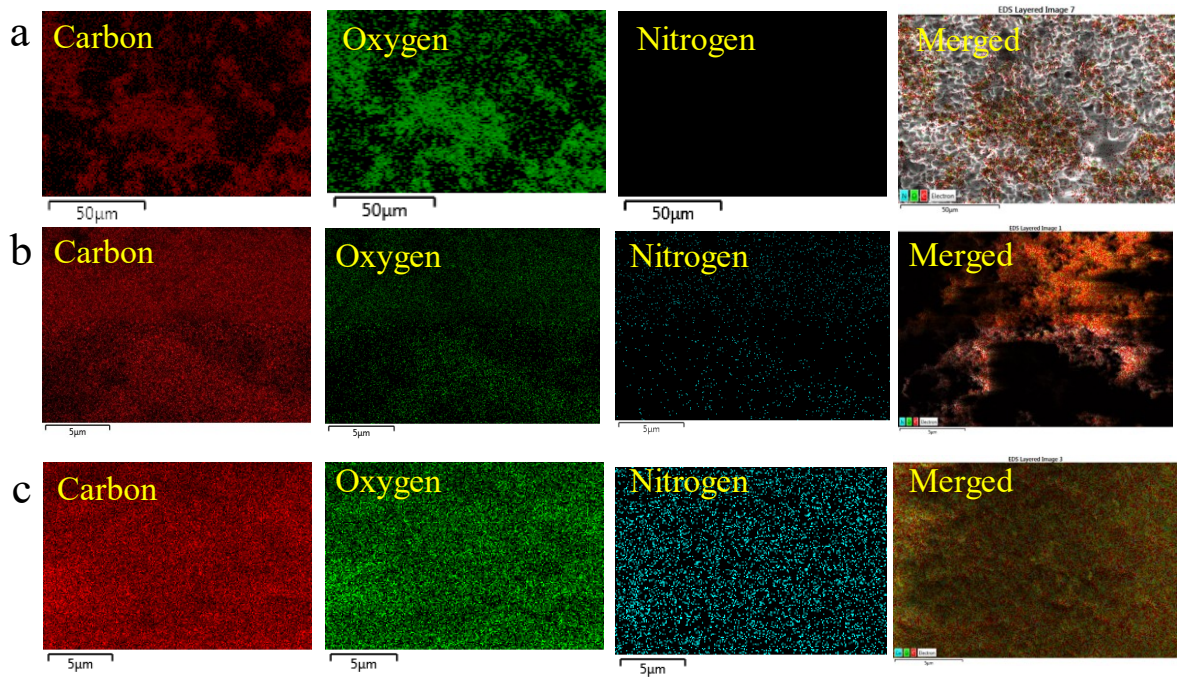

Figure S.1. EDS elemental mapping analysis of various metal doped RF catalyst: (a) RF (b) M-RF (c) H-RF.

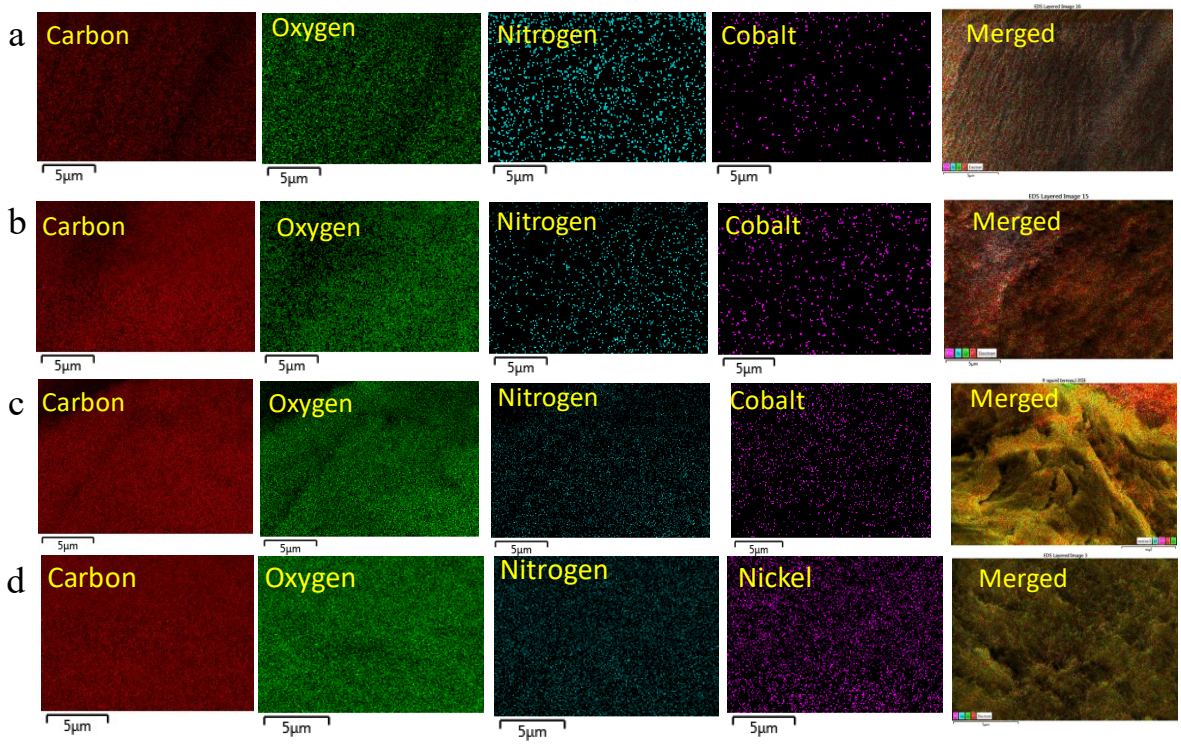

Figure S.2. EDS elemental mapping analysis of various metal doped RF catalyst: (a) Co1-M-RF (b) Co3-M-RF (c) Co5-M-RF (d) Ni3-M-RF.

Primary data for 3D printed structure

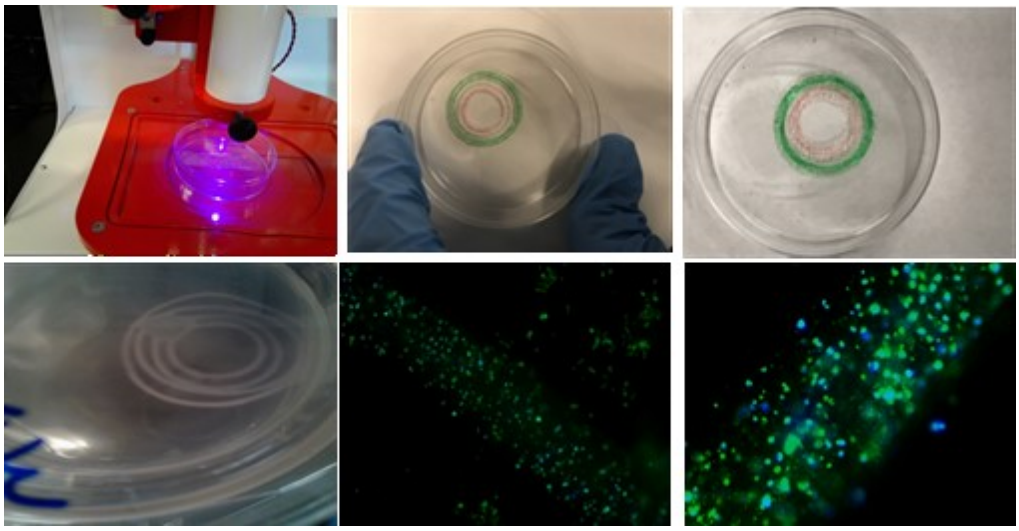

Figure S3. a. printing GelMa7% and alginate with various thickness by Bio Both 3D printer, b. Printing encapsulated cells and Actin & DAPI staining of cells after 1 week.

Synthesis Aqueous Template-Free Resin for catalytic application

Resorcinol and formaldehyde were used as the resource. Two strategies were used for this purpose, first using sodium oleate micelles based on using a carbon dioxide switchable solvent (hexane tertiary amine and dodecane tertiary amine), second using sodium oleate as a surfactant which is created a mesoporous network of resin. In fact, in the first method, the switchable solvent created micelles at 40 ºC. Then the resin network grew on these micelles when formaldehyde 37% was injected. In addition, palladium acetate salt was added before injecting formaldehyde to produce a heterogenous palladium

catalyst. Figure S4 and S5 showed thermal stability, SEM image, and nitrogen adsorption-desorption isotherms of these resins.

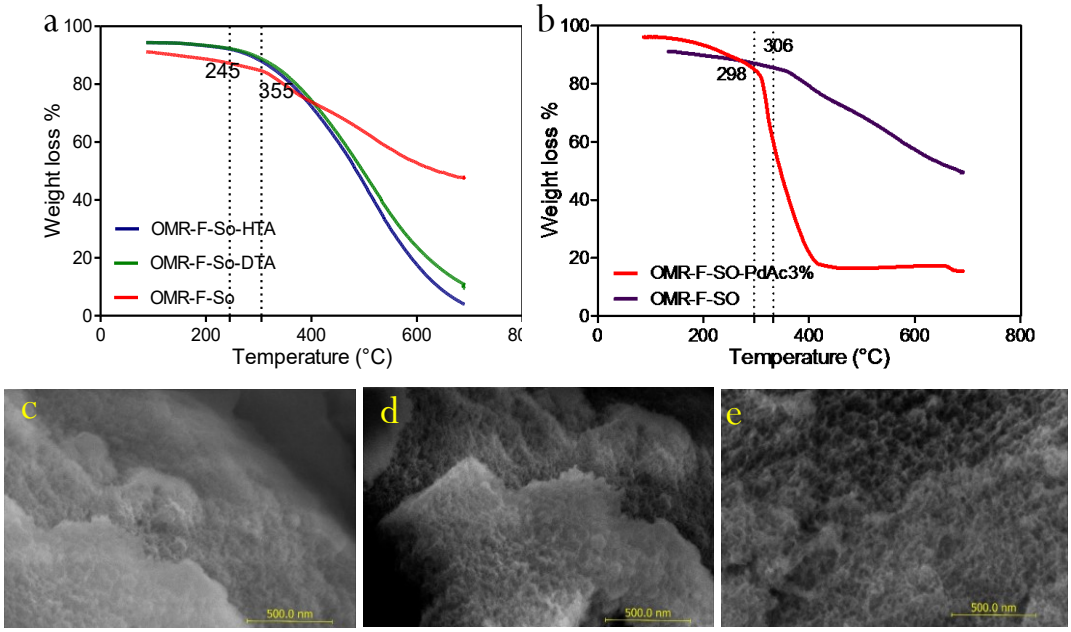

Figure S4 Thermal stability of MR Solvent- template free method with different method and palladium-doped MR solvent-template free method (c-e) SEM images 1. OMR-SO-HTA 2. OMR-SO-DTA 3. OMR-SO

Two main advantages of this method are; removing the need for calcination and reducing the cost by using water as a solvent. This MR has a low price, proper surface area, large pore size and volume, simple preparation, and scalability for the development of eco-friendly commercial resins.

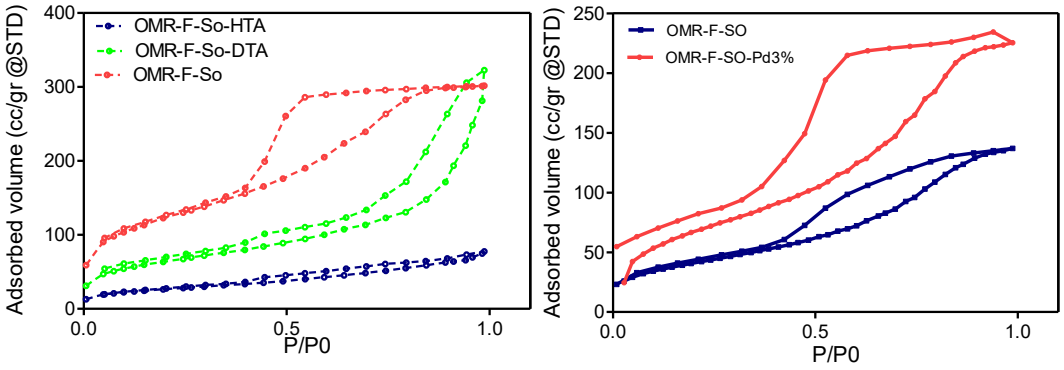

Figure S5. N_2 adsorption-desorption isotherms, (a). MR Solvent- template free method with different method (b) palladium-doped MR solvent-template free method

MR-F-So-Pd3%figure was used for Suzuki- Miyauru cross-coupling reaction. Figure S6 showed that this MR catalyst has a high conversion rate and can be used up to 5 batch cycles showed an efficiency of 92%.

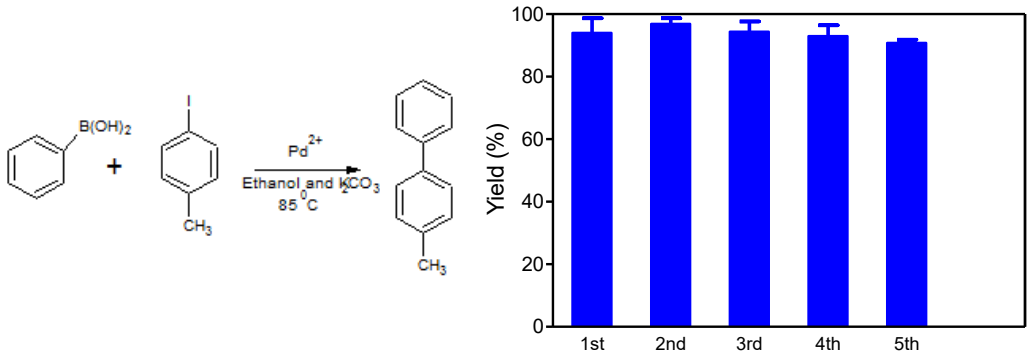

Figure S6. Suzuki- Miyaura reaction conversion rate in batch system for Iodotoluene with ethanol as solvent for 5 reaction cycles (n=3)